INSTITUTO SUPERIOR TÉCNICO
Universidade Técnica de Lisboa

Low-Cost INS/GPS Data Fusion with Extended Kalman Filter for Airborne Applications

by

Adriano Solimeno

A thesis submitted in fulfillment of the requirements for the
Degree of Master of Science in
Aerospace Engineering

Jury

Chair:	Prof. Fernando José Parracho Lau
Supervisor:	Prof. Fernando Duarte Nunes
Examiners:	Prof. Carlos Jorge Ferreira Silvestre
	Prof. Maria Alexandra Aguiar Gomes

July 2007

Acknowledgements

I would like to express my gratitude to my supervisor Prof. Fernando Duarte Nunes for his continuous support, advice, proposed ideas and constructive suggestions during the development of this thesis.

Many thanks go to all my friends and colleagues at the Instituto Superior Técnico de Lisboa. I am very pleased for having met such special people who helped me to carry out successfully my two years of abroad studies. My work and discussions with them were always a pleasure that created an ideal working environment for my research.

Thanks are also given to all my friends in Italy. I deeply appreciated their friendship, frank support, and significant assistance that they constantly and continuously gave me during this long period abroad. In particular, I am very thankful to all that were able to come visit me in Lisbon and enjoy the beauties of this splendid city.

Special thanks go to Justyna, for her everlasting patience, understanding, encouragement, and sacrifice, which have contributed a lot to the successful achievement of this thesis. You kept me going through it all.

Finally, the deepest gratitude of all goes to my family members. I owe all kinds of obligation to my parents and my sister Veronica for their unlimited and unconditional love, inspiration, guidance, care, and financial support. This research, and in fact, my entire education, is the result of a desire for knowledge that was inspired and encouraged by them.

Abstract

INS/GPS integrated systems, based on MEMS technology, are likely to become widely available as a result of the recent advent of low-cost sensors. The current performance achieved by low-cost IMUs is still relatively poor due to the large inertial sensor errors. This can significantly affect the performance of the integrated system in situations of low satellite visibility. Usually, GPS and INS are integrated with a loosely coupled scheme, which is suitable for those applications where satellite availability is always good. However, significant performance improvements can be made by using a tightly coupled integration in applications where GPS outages are frequent and when a reliable, accurate solution is needed during the entire mission. Therefore, the challenge is to develop a robust navigation system that can deal with the large sensor errors experienced with low-grade IMUs.

This thesis investigates the performance of a low-cost INS/GPS system in which the data fusion process is done with an extended Kalman filter. In order to perform numerical simulations, a MATLAB software has been developed. Both the loosely coupled and tightly coupled configurations are analyzed for several types of situations and operational conditions. The results obtained in this work demonstrate that a low-cost INS/GPS navigation system is partially capable of meeting the performance requirements for airborne navigation.

Table of contents

List of tables

List of figures

List of symbols

$\dot{\cdot}$	time derivative
$\hat{\cdot}$	estimated or computed value
$\tilde{\cdot}$	measured value
δ	error of
Δ	increment (difference) of
$E[\cdot]$	expectation of
$\|\cdot\|$	Euclidean/Frobenius norm
$\times$	cross product
$(\cdot\times)$	skew-symmetric form of a vector
$\cdot^{-1}$	matrix inverse
$\cdot^{T}$	matrix transpose
γ	normal gravity
$\Delta\underline{\theta}^{r}_{pq}$	vector of angular increments of *q*-frame relative to *p*-frame, expressed in *r*-frame
Δt	time increment (t_{k+1}-t_k)
$\Delta\underline{v}^{r}_{f}$	specific force measurement expressed in the *r*-frame
$\underline{\varepsilon}$	attitude error vector
ε_{ρ}	measurement noise and multipath on pseudorange
ϕ	roll
Φ	state transition matrix
φ	geodetic latitude
η	stochastic process
λ	geodetic longitude
ν	true anomaly
θ	pitch; orbit latitude
ρ	pseudorange

σ^2	mean squared value
ω	argument of perigee
$\underline{\omega}$	angular rate vector
Ω	skew symmetric matrix form of $\underline{\omega}$; right ascension of ascending node
ψ	yaw
a	semi-major axis
$\underline{a}$	acceleration vector
Az	azimuth angle
b	bias; semi-minor axis
c	speed of light
dP	orbital error of the GPS satellite
d_{ion}	delay due to the ionosphere
dt	GPS satellite clock error
dT	GPS receiver clock error
d_{trop}	delay due to the troposphere
e	eccentricity
i	orbit inclination
E	skew symmetric matrix for the attitude errors
El	elevation angle
f	flattening
$\underline{f}$	specific force vector
F	dynamics matrix
$\underline{g}$	gravity vector
G	noise-input mapping matrix
h	geodetic height
H	design matrix for measurements
I	identity matrix
K	Kalman gain matrix
m	observation vector dimension
n	state vector dimension; number of visible satellites
P	true range between GPS satellite and receiver; error covariance matrix
q	noise spectral density

$\underline{q}$	quaternion vector
Q	covariance matrix of system noise vector
$\underline{r}$	position vector
R	direction cosine matrix; covariance matrix of measurement vector noise
R_M	radius of curvature in meridian
R_N	radius of curvature in prime vertical
R_p^q	rotation matrix from the *p*-frame to the *q*-frame
S	scale factor
T	correlation time
$\underline{v}$	velocity vector; measurement vector noise
V	variance matrix
$\underline{w}$	system noise vector
$\underline{x}$	system state vector
$\underline{z}$	observation vector

List of abbreviations

AHRS	Attitude Heading Reference System
C/A	Coarse-Acquisition
CDMA	Code Division Multiple Access
DCM	Direction Cosine Matrix
DOP	Dilution Of Precision
ECEF	Earth-Centered Earth-Fixed
ECI	Earth-Centered Inertial
EKF	Extended Kalman Filter
FOG	Fiber Optic Gyro
GDOP	Geometrical Dilution Of Precision
GPS	Global Positioning System
HD	High Dynamics
HDOP	Horizontal Dilution Of Precision
IMU	Inertial Measurement Unit
INS	Inertial Navigation System
LC	Loosely Coupled
LD	Low Dynamics
LTP	Local Tangent Plane
MEMS	Micro-Electro-Mechanical System
NED	North-East-Down
P-code	Precise code
PDOP	Position Dilution Of Precision
PPS	Pulse Per Second
PV	Position-Velocity
PVA	Position-Velocity-Acceleration
RMS	Root Mean Square
TBC	To Be Confirmed
TC	Tightly Coupled
TDOP	Time Dilution Of Precision

TEC	Total Electron Content
UAV	Unmanned Air Vehicle
UERE	User Equivalent Range Error
VDOP	Vertical Dilution Of Precision

Chapter 1

Introduction

The last decade has shown an increasing demand for small-sized and low-cost inertial navigation systems (INSs) for use in many airborne applications, such as unmanned air vehicles (UAVs) and general aviation. Advances in microelectronics, computers, and sensor technologies permitted the development of commercial low-cost inertial measurement units (IMUs) and GPS receivers. The integration of these two navigation technologies is a practical positioning option for airborne applications.

The purpose of this chapter is to present some background information on the characteristics of low-cost sensors, specifically, of those adopted in the inertial navigation field, which are usually based on MEMS (Micro-Electro-Mechanical System) technologies. The main advantages, as well as the basic limitations that significantly degrade their performance, are presented. A similar analysis is also done for the Global Positioning System (GPS); the comparison of the benefits and drawbacks of each of these two navigation systems naturally leads to their combination in a process called, in general, data fusion. Finally, research objectives, methodologies, and the thesis outline are given.

1.1 Background

Before the deployment of GPS, dead-reckoning computations were the heart of every automatic navigation system [20]. Dead-reckoning consists of calculating the position from measurements of velocity relative to three orthogonal axes. In practice, the changes of direction and velocity can be measured with a set of three gyroscopes and three accelerometers, which form an IMU. Since the quantities measured by the inertial sensors have to be integrated in order to obtain the vehicle position, the errors tend to aggravate with time elapsing. In

addition, it is required that the initial position is known with good accuracy. As an advantage, the IMU measurements do not require any man-made external source, such as a radio transmitter, and are not affected by intentional (jamming) or non-intentional electromagnetic interference.

Therefore, it is advantageous to merge the INS with GPS since the two systems complement each other. In fact, the shortcomings of each system can be alleviated by the inclusion of the other one.

Fig. 1.1 illustrates the differences between the concepts of IMU and INS.

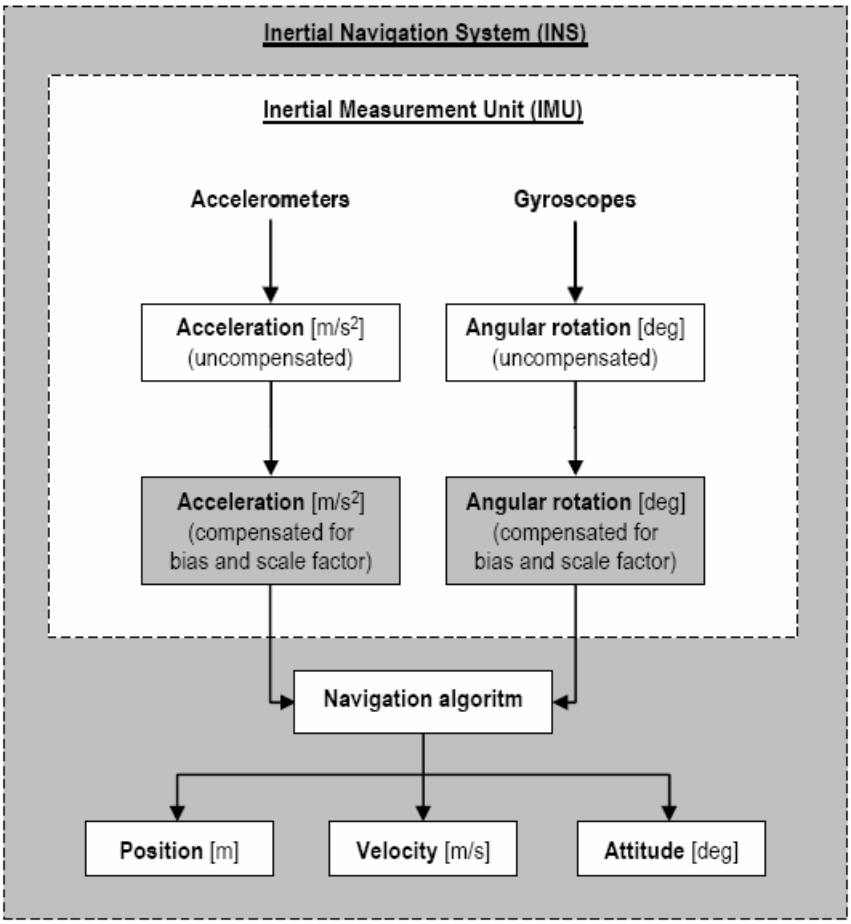

Fig. 1.1 Differences between IMU and INS (adopted from [31])

1.1.1 Low-cost MEMS-based IMUs

Micromachined inertial sensors are a very versatile type of sensors with applications in many areas. Until recently, medium to high performance inertial

sensors were restricted to applications in which the cost of these sensors was not a key factor, such as military systems. The arise of micromachining has generated the possibility of producing precision inertial sensors at a price that allows their usage in cost-sensitive consumer applications [4]. The fabrication processes of MEMS sensors make them very sensitive to the changes in the surrounding environment, such as temperature, pressure, magnetic field, etc. These changes cause the output of MEMS sensors to vary quickly, extensively, and sometimes randomly. This high sensitivity to environmental conditions adds more error types, and often of higher intensity, than those of traditional inertial sensors. All these error sources must be necessarily identified, modeled and determined in order to avoid an excessive degradation in the performance of MEMS sensors. The categorization and the impact of these errors in specific navigation applications will be presented throughout the chapters of this thesis, after having given some information on the well-known basic principles of the inertial navigation systems. In this introductive section, the attention is given to the description of the main advantages of inertial systems in general, as well as their problems and shortcomings.

An inertial navigation system provides position, velocity and attitude information on the basis of specific force and angular rate measurements. Theoretically, it is a self-contained system, meaning that it is autonomous regardless of the operational environment. However, as mentioned before, the accuracy can be seriously diminished because of several types of errors, especially for low-cost sensors. These errors are low frequency in nature, grow over time, and are affected by local gravity. The measurement output rate for these sensors is generally high (100-200 *Hz*). It will be shown that these characteristics are complementary to those of the GPS, which demonstrates the prospective benefits of their integration.

1.1.2 Global Positioning System

The GPS is able to provide accurate and continuous three-dimensional position and velocity information via its satellite constellation. Initially designed for military purposes, it is today available for civilian users as well. With GPS,

accurate positioning has become available for a variety of applications. Besides, the falling cost of GPS receivers over the past few years has rendered this system increasingly more attractive in all the applications where cost is a major factor. GPS accuracy is affected by several types of deterministic and random errors. Some of these errors are independent from the surroundings of the GPS receiver (i.e. the local environmental conditions) such as atmospheric errors, orbit errors, and clock drifts. Additionally, there are also several errors which strongly depend on the local environment, like multipath, jamming, and signal masking. Much research is being done in order to mitigate the effects of these errors which can degrade considerably the accuracy of the navigation solution. Nowadays, modern GPS receivers are only partially capable of tracking and acquiring signals in challenging environments, such as (urban) canyons or heavily dense foliage areas. Recent new technologies have made GPS receivers a very powerful tool in terms of range and quality of the solution; however, its stand-alone operation still remains very limited because of the effects caused by all the errors previously mentioned. For many applications, GPS receivers in stand-alone mode cannot provide a reliable and robust navigation solution. Thus, in canyons or in dense vegetation areas, it is desirable and practical to use an alternative aiding tool for position and velocity information, such as an INS, to improve GPS reliability and integrity (GPS integrity is defined as the ability to protect the user from inaccurate information during GPS outages). Furthermore, a GPS receiver can usually provide measurements at a rate which is much slower than the one of the INS; typical values range between 1 and 10 Hz [19], [27].

1.1.3 INS/GPS integration

The complementary nature of GPS and INS, in the sense that each system can compensate for the other's limitations, leads to their integration with the intent to obtain a navigation system characterized by higher levels of accuracy, reliability, and integrity. Tab. 1.1 illustrates the main differences between the two navigation systems, which have been outlined in the previous sections.

Tab. 1.1 INS-GPS comparison

	INS	GPS
Position and velocity accuracy	accurate over the short term* degrades with time	accurate over the long term does not degrade with time
Initial position calibration	required	not required
Attitude information	available	not available**
Local gravity	sensitive	non-sensitive
Measurement output rate	high	low
Autonomous	yes*	no
Jamming resistant	yes	no

*depending on IMU's quality, **available with multiple GPS antennas

It follows that these two units combined in a common system will provide a superior performance than each single system in stand-alone mode. The main objective of INS/GPS integration is to obtain a navigation system capable to provide:

- high position and velocity accuracy;
- precise attitude determination;
- high output data rate;
- navigational output available during GPS signal outages.

The differences in nature of the errors associated with the two systems benefit their integration through the use of a Kalman filter, which is a linear estimator that uses knowledge of the system dynamics and external measurements to obtain an optimal estimate of the state variables at the current time instant.
The problem of achieving a better performance can be divided into two parts: modeling and estimation. Modeling refers to the development of error models that describe more accurately the INS/GPS system. Estimation is concerned with the intent of achieving more accurate error estimates to be used for error compensation. A compromise must be found between these two issues because an excessive complication of the system model degrades the estimation accuracy of the state vector components. In this thesis, the main

focus is given on the estimation problem. Concerning the modeling part, the results obtained in [13], [14], and [26] will be mostly utilized.
Although in recent time a wide variety of different estimation algorithms have been investigated for INS/GPS integration, Kalman filter techniques are still commonly used for many applications because of the implementation simplicity and the optimal results that can be obtained.
Several different integration strategies have been developed in recent years. They can be divided into two categories: loosely-coupled (or decentralized) and tightly coupled (centralized) schemes. The benefits and drawbacks of each solution will be extensively discussed throughout this work.

1.2 Research objectives

Given the recent great interest towards the integration of low-cost MEMS-IMUs with GPS, this thesis investigates the performance of an integrated low-cost INS/GPS system for airborne applications. Specifically, the main objectives are:

- *To investigate the performance of MEMS-based inertial sensors*: the performance of the sensors will be evaluated for different situations, and will be compared to that obtained with a higher-grade sensor based on the same technology, and with a tactical grade IMU.
- *To investigate the performance of a low-cost INS/GPS system using closed-loop loosely and tightly coupled integration strategies*: the comparison between the two strategies will be done in terms of several aspects (level of accuracy, computational load, observability, error estimation, etc.).
- *To investigate the performance of a low-cost INS/GPS system during GPS outages*: both cases of partial and complete GPS outages will be considered; a simulation of an helicopter canyon flight will show how GPS outages can easily occur in practical situations.

- *To evaluate the performance of the system under different vehicle's dynamics*: this analysis will be done comparing the results obtained with situations of low and high vehicle's dynamics.
- *To investigate the performance of a low-cost INS/GPS system augmented with Galileo*: the purpose of this analysis is to evaluate the advantages offered by an additional satellite constellation in terms of increased accuracy and availability of the navigation solution, as well as improved system observability.

1.3 Research methodologies

In order to meet the objectives outlined in the previous section, the following methodologies have been carried out:

- *Implementation of a mechanization algorithm for strapdown INS*: this is an essential step for INS processing, which is necessary to convert the raw measurements of specific force and angular rates into position, velocity, and attitude information.
- *GPS processing*: this step involves the implementation of a GPS filter to compute the navigation solution from pseudorange and Doppler measurements. Two different filters have been implemented, specifically, for low and high dynamics.
- *Implementation of the integration strategies using the EKF*: this is the step where the navigation solutions from INS and GPS are fused together to obtain a combined solution. Both loosely coupled and tightly coupled approaches have been implemented in a closed-loop configuration (i.e. with error feedback). An augmented Kalman filter has been developed to integrate a MEMS-based IMU with GPS for effective sensor error compensation. The main advantage of such filter is a more efficient correction of the inertial sensor errors, as compared to a traditional filter with a lower number of states.

- *Software development*: the INS mechanization algorithm, the integration strategies, and their corresponding filters are implemented in a software developed with MATLAB. The software works in a post-processing mode but can be easily adapted to real-time applications.
- *Tests and data analysis*: the final step of this research is the presentation of several types of tests and data processing that have been performed. The analysis involves the interpretation of the results in terms of comparison of integration algorithms, types of filters, quality of IMUs, etc.

1.4 Thesis outline

This thesis contains eight chapters and four appendices which are organized as follows.

Chapter 1 presents the background, objectives and motivation for this dissertation.

Chapter 2 gives an overview of the Global Positioning System. GPS measurements and error sources are discussed. A solution of the pseudorange equation is also presented. The final part deals with the concept of dilution of precision.

In Chapter 3, INS fundamentals are reviewed. The basic principles of inertial navigation systems are discussed, including the equations of motion, the mechanization equations, and the error equations. Descriptions of the typical error sources of low-cost inertial sensors and of some common alignment techniques used for airborne applications are given. This chapter ends with an illustration of the principal technologies and implementations adopted for inertial systems.

Chapter 4 covers the Kalman filter theory and its practical implementation. After a brief review of the characteristics of discrete-time systems, the traditional

linear Kalman filter will be discussed in detail. Special attention will be also given to its modified, nonlinear version, known as extended Kalman filter. Finally, the stochastic processes most commonly used for modeling the non-deterministic error sources of INS and GPS are described.

The problem of the integrated INS/GPS system is discussed in Chapter 5. The basic schemes commonly used for performing the integration are given together with the details of the INS/GPS data fusion using the EKF. Advantages and limitations of each solution are discussed.

Chapter 6 provides a description of the software developed to run the simulations of the INS/GPS integrated system. The main modules that constitute the software, their characteristics and functions are briefly described.

In Chapter 7, the tests and performance analysis results are presented. Various tests have been carried out, and the data analysis is done in terms of accuracy of the navigation solution, system behavior during partial and complete GPS outages, system observability and filter capability in estimating the sensor errors. The final part of this chapter presents the simulation results of an innovative INS/GPS system augmented with Galileo, the European Global Navigation Satellite System currently under development.

Finally, Chapter 8 draws the major conclusions from this research work, and provides some topics that need further investigation and development.

Chapter 2

Overview of the Global Positioning System

This chapter reviews the basic concepts of the GPS, firstly focusing on its components and signal characteristics. A description of the GPS observables and the different error sources will be given, followed by an analytical solution for the pseudorange equation. Finally, the selection of satellites to obtain better user position accuracy and the concept of dilution of precision will be discussed.

2.1 Basic concepts

The Global Positioning System is a satellite-based navigation system that was developed by the U.S. Department of Defense in the early 1970s. Initially developed as a military system, it was later made available to civilians, and is now a dual-use system that can be accessed by both military and civilian users [9]. It is well described in standard textbooks such as [2], [9], [19], and [27], and will be not discussed with much detail here.

The GPS consists basically of three segments: the space segment, the control segment, and the user segment. The space segment consists of 24 satellites arranged in 6 orbital planes with an inclination angle of 55º relative to the Earth equator, as shown in Fig. 2.1. The satellites have approximately an average orbit radius of 20200 *km* and complete one orbit in 11 hours and 58 minutes. The control segment monitors the health of the orbiting satellites and uploads navigation data. It consists of a system of tracking stations located around the world, including six monitor stations, four ground antennas, and a master control station [11]. The user segment consists of receivers specifically designed to receive, decode, and process the GPS satellite signals.

Fig. 2.1 GPS satellite constellation

GPS satellites transmit two carrier frequencies: the primary L1 (1575.42 *MHz*) and the secondary L2 (1227.60 *MHz*). These frequencies are modulated by the navigation message and by spread spectrum codes with a unique pseudo-random noise sequence for each satellite [2]. Therefore, a signal coming from each satellite of the GPS constellation can be distinguished and separated from others by the Code Division Multiple Access (CDMA) technique. Currently, GPS signals are modulated by two codes, namely, the Coarse-Acquisition (C/A) code on L1 and the Precise (P) code on L1 and L2. The P-code is restricted to military use via its encryption by the Y-code, a practice known as anti-spoofing. This thesis deals only with L1 C/A-code measurements, of which a more detailed description follows.

The C/A-code is generated by two 10-bit shift registers, where the outputs of the two registers are again added to produce the new code. The C/A-code is a relatively short code with a period of 1 *ms* (1023 bits) for fast acquisition at a rate of 1023 *Mbps*. To provide good multiple access properties, the C/A-codes are designed from a family of codes referred as Gold codes, which are obtained from the product of two equal period 1023 bit codes to form a code with the same period [27].

In general, the GPS signal contains pseudorange, carrier phase and Doppler measurements. The L1 C/A-code pseudorange and Doppler measurements can be used for position and velocity calculation.

A more detailed description of the GPS navigation message is given in Appendix A, together with the illustration of the classical orbital parameters.

2.2 GPS observables

Pseudorange observations are obtained by measuring how long it takes for the signal to propagate from the satellite to the receiver and multiplying the propagation time by the speed of light. Due to non-synchronized receiver and satellite clocks, the measured range (pseudorange) is always biased. If pseudorange measurements can be made from at least four satellites, enough information exists to solve for the unknown position of the GPS user (3D coordinates) and for the receiver clock error (Fig. 2.2).

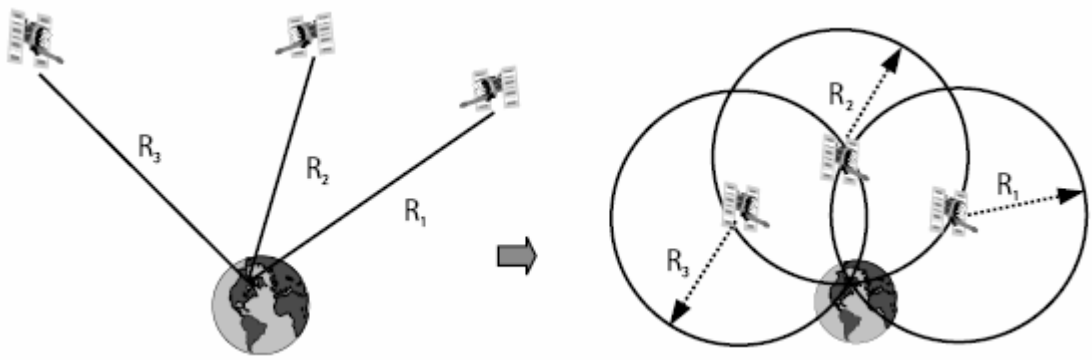

Fig. 2.2 Basic idea of GPS positioning

The pseudorange measurement for a single satellite can be expressed as [19], [27]:

$$\rho = P + dP + c\left(dt - dT\right) + d_{ion} + d_{trop} + \varepsilon_{\rho} \tag{2-1}$$

where

- ρ is the pseudorange observation (*m*);
- P is the true range between GPS satellite and receiver (*m*);
- dP is the orbital error of the satellite (*m*);
- c is the speed of light (*m/s*);
- dt is the satellite clock error (*s*);
- dT is the receiver clock error (*s*);
- d_{ion} is the delay due to the ionosphere (*m*);
- d_{trop} is the delay due to the troposphere (*m*);
- ε_{ρ} is the measurement noise and multipath effect (*m*).

A brief overview of these errors is given in section 2.3.

Doppler measurements (also known as delta-ranges) are obtained by determining the change in phase (i.e. range) over a given time interval divided by the interval length [11]. A change in phase corresponds to a frequency shift that is proportional to the relative velocity between the emitter (the satellite) and the receiver; this is commonly known as Doppler effect. Therefore, by measuring the frequency shift and knowing the emitter's velocity, the receiver's velocity can be determined. Doppler measurements are also corrupted by several types of error [11]:

$$\dot{\rho} = \dot{P} + d\dot{P} + c\left(d\dot{t} - d\dot{T}\right) + \dot{d}_{ion} + \dot{d}_{trop} + \dot{\varepsilon}_{\dot{\rho}} \tag{2-2}$$

where

- $\dot{\rho}$ is the Doppler observation (*m/s*);
- $\dot{P}$ is the true range rate between GPS satellite and receiver (*m/s*);
- $d\dot{P}$ is the orbital error drift of the satellite (*m/s*);
- $d\dot{t}$ is the satellite clock drift;
- $d\dot{T}$ is the receiver clock drift;
- $\dot{d}_{ion}$ is the delay drift due to the ionosphere (*m/s*);
- $\dot{d}_{trop}$ is the delay drift due to the troposphere (*m/s*);
- $\dot{\varepsilon}_{\dot{\rho}}$ is the measurement noise and the rate of change of multipath (*m/s*).

2.3 GPS errors

Eqs. (2-1) and (2-2) indicate that the GPS receiver's measurements are corrupted by several forms of error. Each one is briefly discussed in the following subsections.

2.3.1 Satellite clock errors

Timing of the signal transmission from each satellite is directly controlled by its own atomic clocks. Although such clocks are highly accurate, errors can be large enough to require correction (partly because it would be difficult to synchronize the clocks closely in all satellites). Instead, the clocks are allowed some degree of relative drift that is estimated by the ground stations and is used to generate clock correction data in the GPS navigation message. The result of such process is called GPS time. The time of transmission used in calculating pseudoranges must be in GPS time because is common to all satellites. Typically the onboard satellite clock error is less than 1 *ms* and varies slowly; after the correction has been applied, the residual error in GPS time is less than a few nanoseconds [9].

2.3.2 Receiver clock errors

Usually, receiver clocks are inexpensive quartz crystal oscillators, which are much less accurate than the satellite clocks [9]. Thus, the receiver clock errors have to be continuously estimated. The navigation equation includes a solution for the receiver clock error. Receivers that incorporate the clock error in the Kalman filter state vector need a suitable mathematical model. A typical two-state model will be described in section 5.2.1.1.

2.3.3 Ionospheric delay

The ionospheric delay (or advance) is due to the presence of free electrons in the upper atmosphere, typically between 50 and 1000 *km* above the Earth's surface [9]. These free electrons influence the electromagnetic wave propagation, and their presence is closely related to the amount of solar radiation; for such reason, ionospheric effects show diurnal and seasonal variations. The ionosphere affects the phase and group velocity. Approximated values are, respectively [19]:

$$v_p = \frac{c}{1 - \frac{40.3 n_e}{f^2}} \tag{2-3}$$

$$v_g = \frac{c}{1 + \frac{40.3 n_e}{f^2}} \tag{2-4}$$

where f is the signal frequency and n_e is the electron density. Note that the phase velocity exceeds the group velocity (ionospheric divergence). Since the group velocity depends on the signal frequency, the group delay can be estimated by observing the time of arrival of two signals with different frequencies (multi-frequency receivers). In receivers with a single frequency the ionospheric delay has to be estimated using the Klobuchar model and parameters that are transmitted in the navigation data [27]. This last approach yields less accurate corrections.

The speed of propagation of a radio signal in the ionosphere depends on the number of free electrons in its path, called the Total Electron Content (TEC): it is defined as the number of electrons in a tube of 1 m^2 cross section extending from the receiver to the satellite. The TEC can be measured in TCE Units (TECU), with 1 TECU $= 10^{16}\ electrons/m^2$. The group delay in seconds is given by

$$\Delta\tau_g = \frac{40.3 TEC}{c f^2} \tag{2-5}$$

whereas the phase delay is

$$\Delta\tau_p = -\Delta\tau_g \tag{2-6}$$

Fig. 2.3 shows a world map with the TEC along the GPS signal path coming from a satellite located at the zenith. Improving methods of mapping the ionosphere is a current topic of interest, since the error caused by this effect can be significant. Typically it varies between 1 and 15 *m* [17].

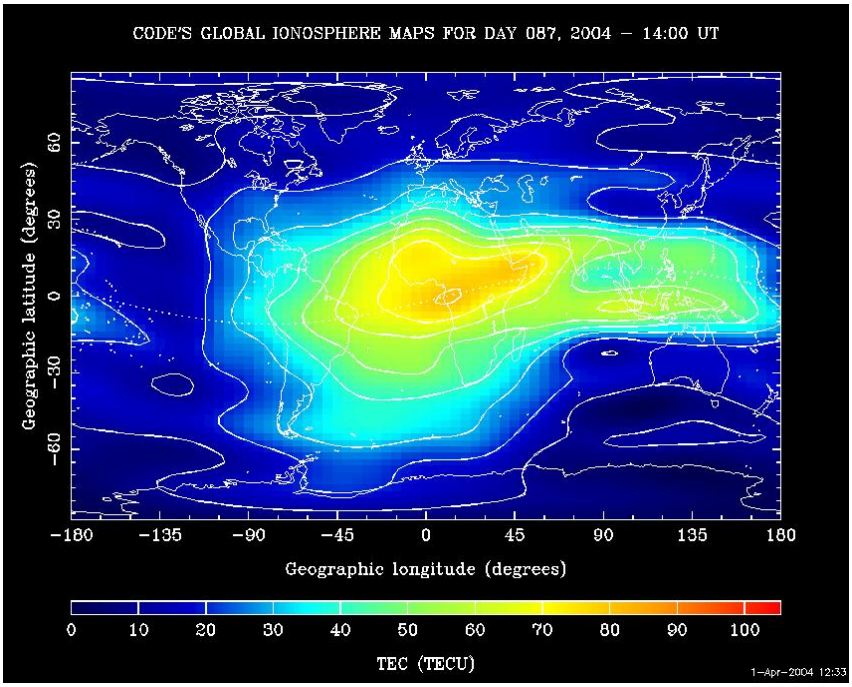

Fig. 2.3 Ionosphere map for TEC evaluation

2.3.4 Tropospheric delay

The troposphere is the layer of the atmosphere closest to the Earth which reaches a height of about 50 *km*. Because it is filled with water vapor, it refracts the GPS signal causing a reduction of its speed (phase delay). Several models exist for the tropospheric errors ([11], [19]) and they are usually based on differential techniques. In fact, weather parameters, which are continuously measured by the base stations, have considerable spatial and temporal variations. The ability of differential techniques to compensate for tropospheric effects will depend on the relative position between the user and the base station. The magnitude of the resulting signal delay typically varies from 2.5 to 15 *m* [17], and increases when the satellite elevation angle diminishes.

2.3.5 Multipath errors

Multipath is a major error source which occurs when the GPS signal arrives at the receiver antenna through different paths. These paths can be the direct line

of sight signal and reflected signals from objects surrounding the receiver antenna or from the ground (Fig. 2.4). Multipath distorts the original signal through interference with the reflected signals at the GPS antenna. Without multipath protection, C/A code errors of up to 10 *m* or more can be experienced [17]. However, with new advances in receiver technology, actual pseudorange multipath is dramatically reduced. A detailed description of multipath mitigation methods can be found in [17], [19], and [27].

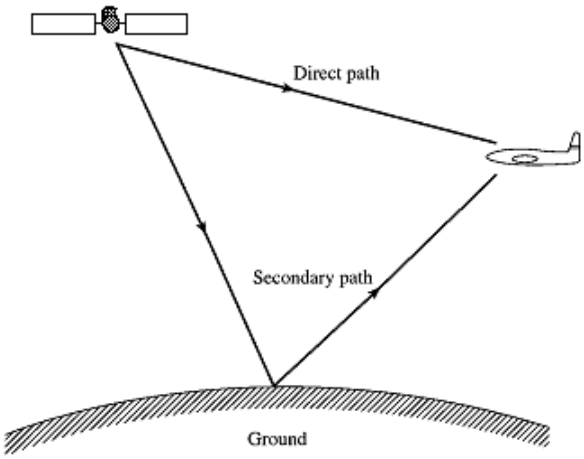

Fig. 2.4 The multipath problem

2.3.6 Satellite orbital errors

The satellite positions are predicted, on the basis of the previous motion of the satellites and through the knowledge of the Earth's gravity field, in order to be broadcast in real-time to the user through what is called the ephemeris data. Since the ephemeris model is a curve fit to the measured orbit, it will contain a time-varying residual error relative to the actual orbit [11]. An ephemeris error is usually in the order of 2 to 5 *m* [9].

2.3.7 Measurement noise

Different types of noise contribute to what is commonly called measurement noise:

- code and carrier random measurement noise (also known as receiver noise), which is a broad term covering the radio frequency radiation sensed by the antenna in the band of interest that is unrelated to the signal;
- noise introduced by the antenna, amplifiers, cables, and the receiver interferences;
- signal quantization noise.

Usually the measurement noise is modeled as white noise as it is uncorrelated over time, channels and receivers.

2.3.8 User Equivalent Range Error

In order to evaluate the combined effect of the errors described above, it is convenient to convert each one of them into an equivalent range error experienced by a user, which is called the User Equivalent Range Error (UERE). In general, errors from different sources have different statistical properties. However, if sufficiently long time periods are considered, all errors can be assumed as independent zero-mean random processes that can be combined to form a single UERE. This is accomplished by determining the root-mean-square (RMS) of the UERE errors from all sources:

$$UERE = \sqrt{\sum_{i=1}^{n} \left(UERE\right)_i^2} \tag{2-7}$$

Tab. 2.1 depicts typical values for GPS UERE errors and their combined effect for the C/A code at the 1-σ level assuming that the ionospheric delay and multipath are compensated in the receiver [19].

Tab. 2.1 GPS UERE budget for the C/A code (adopted from [19])

Segment	Error source	1-σ UERE (m)
Space	Stability of satellite clock	3.0
	Satellite perturbations	1.0
	Others	0.5
Control	Ephemeris errors	4.2
	Others	0.9
User	Ionospheric delay	5.0
	Tropospheric delay	1.5
	Multipath	2.5
	Measurement noise	1.5
	Others	0.5
UERE	Total	**8.0**

The UERE model corresponding to Tab. 2.1 does not take into account the elevation angle of each satellite, and thus is not very accurate. A better approximation, proposed in [27], consists of assuming that the measurement noise for satellite *i* is of the form

$$w_i\left(El_i\right) = w_{0,i} + w_1 f_i\left(El_i\right) \tag{2-8}$$

where $w_{0,i}$ are independent noise terms of variance $7\sigma^2/8$, w_1 has variance $\sigma^2/8$, and the obliquity factor f_i is approximated as

$$f_i\left(El_i\right) = \frac{1.1}{\sin\left(EL_i\right) + 0.1}, \qquad El_i > 0^{\circ} \tag{2-9}$$

where El_i is the elevation angle of satellite *i*.

2.4 Solution of the pseudorange equations

With the introduction of the UERE, Eq. (2-1) can be rewritten as follows:

$$\rho_i = \sqrt{\left(x_i - x_u\right)^2 + \left(y_i - y_u\right)^2 + \left(z_i - z_u\right)^2} - cdT + UERE_i \tag{2-10}$$

where all the error sources have been gathered into the UERE parameter and the geometric distance between the *i*-satellite and the user has been written in terms of Cartesian coordinates.

Measurements from at least four different satellites permit the determination of the unknown user coordinates (x_u, y_u, z_u) and the receiver clock error (dT). Although closed-form solutions are available [11], in this work the classical method based on linearization has been considered since it leads directly to the Kalman filter technique, as described later on.

Using an estimate of the user position ($\hat{x}_u$, $\hat{y}_u$, $\hat{z}_u$) and of the receiver clock error ($d\hat{T}$), an approximate pseudorange can be determined:

$$\hat{\rho}_i = \sqrt{\left(x_i - \hat{x}_u\right)^2 + \left(y_i - \hat{y}_u\right)^2 + \left(z_i - \hat{z}_u\right)^2} - cd\hat{T} \tag{2-11}$$

The user position and the receiver clock error are unknown but can be expressed through the sum of the estimate and an incremental component:

$$x_u = \hat{x}_u + \Delta x_u \tag{2-12}$$

$$y_u = \hat{y}_u + \Delta y_u \tag{2-13}$$

$$z_u = \hat{z}_u + \Delta z_u \tag{2-14}$$

$$dT = d\hat{T} + \Delta t_u \tag{2-15}$$

Applying a first-order Taylor series expansion to Eq. (2-10) gives

$$\rho_i = \hat{\rho}_i + \frac{\partial \hat{\rho}_i}{\partial \hat{x}_u}\Delta x_u + \frac{\partial \hat{\rho}_i}{\partial \hat{y}_u}\Delta y_u + \frac{\partial \hat{\rho}_i}{\partial \hat{z}_u}\Delta z_u + \frac{\partial \hat{\rho}_i}{\partial\left(d\hat{T}\right)}\Delta t_u + \ldots \tag{2-16}$$

where the partial derivatives are

$$\frac{\partial \hat{\rho}_i}{\partial \hat{x}_u} = -\frac{x_i - \hat{x}_u}{\sqrt{\left(x_i - \hat{x}_u\right)^2 + \left(y_i - \hat{y}_u\right)^2 + \left(z_i - \hat{z}_u\right)^2}} \tag{2-17}$$

$$\frac{\partial \hat{\rho}_i}{\partial \hat{y}_u} = -\frac{y_i - \hat{y}_u}{\sqrt{\left(x_i - \hat{x}_u\right)^2 + \left(y_i - \hat{y}_u\right)^2 + \left(z_i - \hat{z}_u\right)^2}} \tag{2-18}$$

$$\frac{\partial \hat{\rho}_i}{\partial \hat{z}_u} = -\frac{z_i - \hat{z}_u}{\sqrt{\left(x_i - \hat{x}_u\right)^2 + \left(y_i - \hat{y}_u\right)^2 + \left(z_i - \hat{z}_u\right)^2}} \tag{2-19}$$

$$\frac{\partial \hat{\rho}_i}{\partial \left(d\hat{T}\right)} = -c \tag{2-20}$$

By substituting Eqs. (2-17) through (2-20) into Eq. (2-16), and considering a system of equations for a number of satellites $n \geq 4$, we obtain

$$\Delta \underline{\rho} = H \Delta \underline{x} \tag{2-21}$$

where

$$\Delta \underline{\rho} = \begin{bmatrix} \rho_1 - \hat{\rho}_1 \\ \rho_2 - \hat{\rho}_2 \\ \vdots \\ \rho_n - \hat{\rho}_n \end{bmatrix}, \quad H = \begin{bmatrix} \frac{\partial \hat{\rho}_1}{\partial \hat{x}_u} & \frac{\partial \hat{\rho}_1}{\partial \hat{y}_u} & \frac{\partial \hat{\rho}_1}{\partial \hat{z}_u} & -1 \\ \frac{\partial \hat{\rho}_2}{\partial \hat{x}_u} & \frac{\partial \hat{\rho}_2}{\partial \hat{y}_u} & \frac{\partial \hat{\rho}_2}{\partial \hat{z}_u} & -1 \\ \vdots & \vdots & \vdots & \vdots \\ \frac{\partial \hat{\rho}_n}{\partial \hat{x}_u} & \frac{\partial \hat{\rho}_n}{\partial \hat{y}_u} & \frac{\partial \hat{\rho}_n}{\partial \hat{z}_u} & -1 \end{bmatrix}, \quad \Delta \underline{x} = \begin{bmatrix} \Delta x_u \\ \Delta y_u \\ \Delta z_u \\ c\Delta t_u \end{bmatrix} \tag{2-22}$$

The least-squares solution of Eq. (2-21) is

$$\Delta \underline{x} = \left(H^T H\right)^{-1} H^T \Delta \underline{\rho} \tag{2-23}$$

For $n=4$ the solution is simply

$$\Delta \underline{x} = H^{-1} \Delta \underline{\rho} \tag{2-24}$$

Although the least-squares method herein described permits to solve the pseudorange system of equations and determine the spatial coordinates

(x_u, y_u, z_u), it will be seen later on that the use of the extended Kalman filter yields solutions with better characteristics.

2.5 Dilution of precision

The positioning errors in the GPS receiver depend essentially on the errors that affect the estimated pseudoranges (through the UERE parameter) and on the geometry of the satellites in the sky. The dilution of precision (DOP) is often used to measure the part of the user position accuracy that depends on the satellite constellation geometry. There are several different definitions of DOP, and they are all function of the satellite geometry only. The pseudorange errors are considered zero-mean random Gaussian variables. Therefore, assuming a fixed geometry, $\Delta\underline{x}$ is a Gaussian vector with zero-mean and covariance matrix given by [19]

$$\begin{aligned}\mathrm{cov}\left(\Delta\underline{x}\right) &= E\left\{\Delta\underline{x}\Delta\underline{x}^T\right\} = \\ &= E\left\{\left(H^TH\right)^{-1}H^T\Delta\underline{\rho}\left(\Delta\underline{\rho}^T\right)H\left(H^TH\right)^{-1}\right\} = \\ &= \left(H^TH\right)^{-1}H^TE\left\{\Delta\underline{\rho}\left(\Delta\underline{\rho}^T\right)\right\}H\left(H^TH\right)^{-1}\end{aligned} \tag{2-25}$$

where matrix H is

$$H = -\begin{bmatrix} a_{x,1} & a_{y,1} & a_{z,1} & 1 \\ a_{x,2} & a_{y,2} & a_{z,2} & 1 \\ \vdots & \vdots & \vdots & \vdots \\ a_{x,n} & a_{y,n} & a_{z,n} & 1 \end{bmatrix} \tag{2-26}$$

with

$$a_{x,i} = \frac{x_i - x_u}{r_i} \tag{2-27}$$

$$a_{y,i} = \frac{y_i - y_u}{r_i} \tag{2-28}$$

$$a_{z,i} = \frac{z_i - z_u}{r_i} \tag{2-29}$$

and

$$r_i = \sqrt{\left(x_i - x_u\right)^2 + \left(y_i - y_u\right)^2 + \left(z_i - z_u\right)^2} \tag{2-30}$$

is the distance between satellite *i* and the receiver. Note that $(H^T H)^{-1}$ is a symmetric matrix. Assuming also that the terms in $\Delta\underline{\rho}$ are equally distributed and independent with a variance equal to the square of the UERE parameter (considered the same for all satellites to simplify the problem) we can write:

$$E\left\{\Delta\underline{\rho}\left(\Delta\underline{\rho}^T\right)\right\} = I_{nxn}\sigma^2_{UERE} \tag{2-31}$$

which substituted into Eq. (2-25) gives

$$\begin{aligned}\operatorname{cov}\left(\Delta\underline{x}\right) &= \left(H^T H\right)^{-1} H^T H \left(H^T H\right)^{-1} \sigma^2_{UERE} = \\ &= \left(H^T H\right)^{-1} \sigma^2_{UERE} = \\ &= V\sigma^2_{UERE}\end{aligned} \tag{2-32}$$

The DOP parameters are defined as the ratio of a combination of the elements of the GDOP matrix $V = \left(H^T H\right)^{-1}$ with the parameter σ^2_{UERE}. The geometrical dilution of precision (GDOP) is the most general parameter, defined as

$$GDOP = \sqrt{V_{11} + V_{22} + V_{33} + V_{44}} = \sqrt{trace\left(H^T H\right)^{-1}} \tag{2-33}$$

Other DOP parameters are used to characterize the precision of the different components of the spatial/temporal solution: the position dilution of precision (PDOP), the horizontal dilution of precision (HDOP), the vertical dilution of

precision (VDOP), and the time dilution of precision (TDOP) are the most typical. Their corresponding definitions are given below:

$$PDOP = \sqrt{V_{11} + V_{22} + V_{33}} \tag{2-34}$$

$$HDOP = \sqrt{V_{11} + V_{22}} \tag{2-35}$$

$$VDOP = \sqrt{V_{33}} \tag{2-36}$$

$$TDOP = \sqrt{V_{44}} \tag{2-37}$$

The smallest DOP value means the best satellite geometry for calculating user position. Efficient algorithms for computing DOP factors are necessary in applications that will select the satellites to be used based on the minimization of a desired DOP parameter.

2.6 Impact of the constellation geometry on the DOP parameters

In order to better understand the impact of the satellite constellation geometry on the DOP parameters a simple example can be considered.

The position of a satellite with respect to the user can be expressed in terms of the azimuth angle (Az, measured clockwise starting from the North) and the elevation angle (El, measured in the local horizontal plane, with $0^o \le El \le 90^o$). Matrix H, defined in Eq. (2-26), can be rewritten as [27]

$$H = -\begin{bmatrix} \cos(El_1)\sin(Az_1) & \cos(El_1)\cos(Az_1) & \sin(El_1) & 1 \\ \cos(El_2)\sin(Az_2) & \cos(El_2)\cos(Az_2) & \sin(El_2) & 1 \\ \cos(El_3)\sin(Az_3) & \cos(El_3)\cos(Az_3) & \sin(El_3) & 1 \\ \cos(El_4)\sin(Az_4) & \cos(El_4)\cos(Az_4) & \sin(El_4) & 1 \end{bmatrix} \tag{2-38}$$

It can be demonstrated [27] that the minimization of the GDOP parameter for *n*=4 corresponds to a situation of three satellites equally spaced above the horizon with the lowest possible elevation angle, and one satellite located vertically above the user.

The impact of the satellite constellation geometry on the DOP parameters is shown in Fig. 2.5. These results have been obtained with a satellite fixed in the zenith, while the other three, maintained all the time equally spaced, have an elevation angle varying between -10º and 60º. Note that negative elevation angles can be achieved with a receiver mounted on an aircraft and with low orbit satellites. High values of elevation angles are typical of situations like canyon flights in which only a reduced area of the sky is visible; the GPS signals that reach the user will be only those coming from the satellites with the highest elevation angles. This situation will be analyzed with more details in section 7.4.2.1.

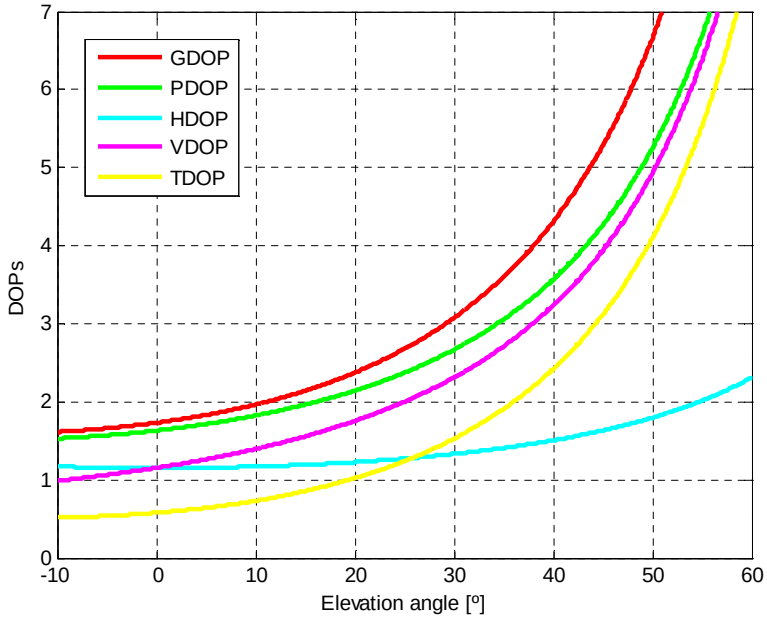

Fig. 2.5 DOPs as function of the elevation angle (using a constant UERE)

The nearly stable value of the HDOP along the entire interval proves that the assumed satellite configuration is good. Satellites concentrated in a smaller sky portion would cause a greater variability of the results. It is also interesting to observe that the lowest values of elevation angles lead to smallest errors in the vertical direction.

By observing Fig. 2.5, one might draw the conclusion that the optimal geometry is achieved with the three satellites having elevation angles almost equal to zero. However, in practical situations, the effects of multipath, of ionospheric

and tropospheric delays, and of GPS signal power loss must be taken into account, especially for low elevation angles.

Eq. (2-31) is valid under the assumption that the UERE parameter is the same for all satellites. We already saw that for practical situations this is not true, and a more realistic model is given by Eq. (2-8). By considering this model, Eq. (2-31) can be rewritten as follows:

$$E\left\{\Delta\underline{\rho}\left(\Delta\underline{\rho}^{T}\right)\right\} = E\left\{\underline{w}\underline{w}^{T}\right\} = R \tag{2-39}$$

where

$$R_{ij} = \begin{cases} \left(7 + f_i f_j\right)\sigma^2 / 8, & \text{for } i = j \\ f_i f_j \sigma^2 / 8, & \text{for } i \neq j \end{cases} \tag{2-40}$$

Note that it has been assumed that the error term $w_1 f_i$ of Eq. (2-8) is random and correlated for all satellites. This new result leads to a different expression of the covariance matrix defined in Eq. (2-25) [27]:

$$\operatorname{cov}\left(\Delta\underline{x}\right) = \left(H^T R^{-1} H\right)^{-1} \tag{2-41}$$

The effective DOP parameters can be obtained normalizing this covariance matrix to σ^2; their values are shown in Fig. 2.6. Except for the HDOP which still remains stable along the entire interval, the other parameters begin to increase significantly for elevation angles below 10º.

Although an approximated model has been adopted for this example, the results obtained are still indicative of the typical impacts of low elevation angle operations.

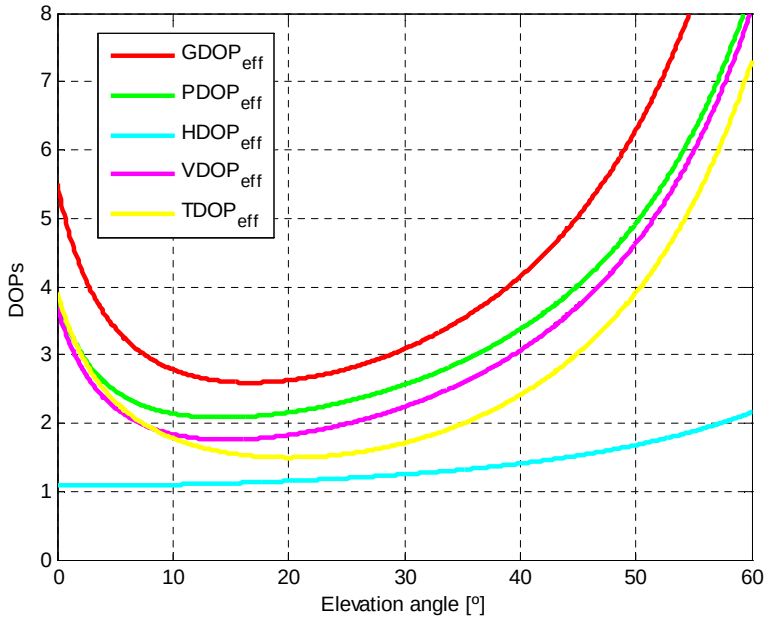

Fig. 2.6 Effective DOPs obtained with the approximated model of Eq. (2-8)

Chapter 3

Overview of the Inertial Navigation System

An inertial navigation system calculates the position, velocity, and attitude of a vehicle by measuring the accelerations and rotations applied to the system's inertial frame. An inertial measurement unit is constituted by orthogonally mounted accelerometers and angular rate sensors (gyros). The combination of the IMU with the mechanization equations (and possibly the system errors estimation) forms the INS.

This chapter begins with a description of the coordinate frames usually utilized in inertial data processing, and then briefly presents the INS kinematic and mechanization equations. These equations are then perturbed to define the INS error dynamics equations. A description of the typical INS error sources is given, followed by a list of the most common alignment methods used for airborne applications. The final part of this chapter deals with the main technologies and implementations used for IMUs.

3.1 Coordinate frames

Four coordinate frames are used in this dissertation. The discussion of each follows from [11] and [17]. The majority of notation used throughout the text can be summarized as follows:

- a vector denoted $\underline{x}^p$ represents a quantity $\underline{x}$ expressed in the *p*-frame;
- a rotation (transformation) matrix of the form R_p^q transforms a vector from the *p*-frame to the *q*-frame;
- the angular velocity between two frames expressed in a specific frame can be represented either by a vector $\underline{\omega}$ or by the corresponding skew-symmetric matrix Ω (with $\Omega^T = -\Omega$).

For example

$$\underline{\omega}_{pq}^{r} = \begin{bmatrix} \omega_x & \omega_y & \omega_z \end{bmatrix}^T \tag{3-1}$$

or

$$\Omega_{pq}^{r} = \begin{bmatrix} 0 & -\omega_z & \omega_y \\ \omega_z & 0 & -\omega_x \\ -\omega_y & \omega_x & 0 \end{bmatrix} \tag{3-2}$$

describe the angular velocity between the *p*-frame and the *q*-frame expressed in the *r*-frame.

3.1.1 Inertial frame (*i*-frame)

Earth-Centered Inertial (ECI) coordinates are the favored inertial coordinates in the near-Earth environment. The origin of ECI coordinates is at the center of gravity of the Earth, and the three axes are defined as follows (Fig. 3.1):

- X^i in the direction of the vernal equinox;
- Z^i parallel to the rotation axis (North polar axis) of the Earth;
- Y^i to make a right-handed orthogonal coordinate system.

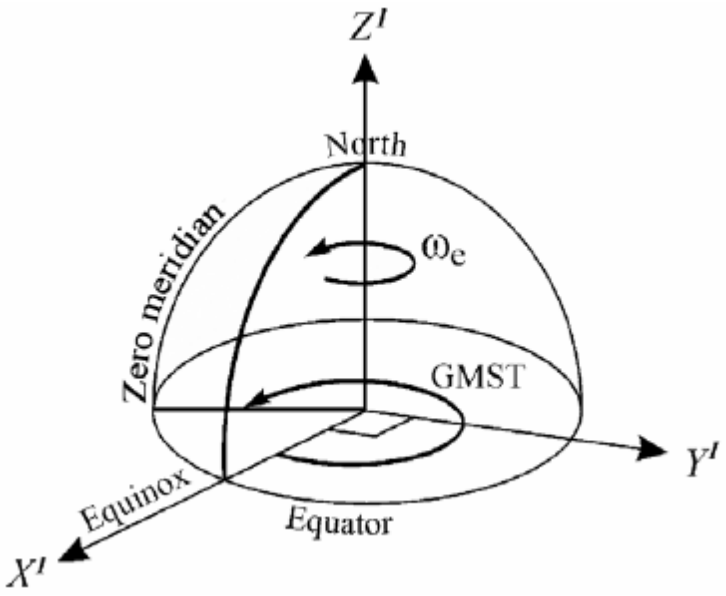

Fig. 3.1 The inertial frame

3.1.2 Earth frame (*e*-frame)

The Earth-Centered Earth-Fixed (ECEF) coordinates have the same origin and third (polar) axis as the ECI coordinates but rotate with the Earth. The three axes are defined as follows (Fig. 3.2):

- X^e toward the mean meridian of Greenwich;
- Z^e parallel to the Earth's rotation axis (as for the *i*-frame);
- Y^e to make a right-handed orthogonal coordinate system.

3.1.3 Local geodetic frame (*n*-frame)

Local Tangent Plane (LTP) coordinates serve as local reference directions for representing vehicle attitude and velocity for operation on or near the surface of the Earth; for this reason, it is often referred to as navigation frame (*n*-frame). A common orientation for LTP coordinates is the North-East-Down (NED) system defined as follows:

- X^n horizontal axis in the direction of increasing latitude;
- Y^n horizontal axis in the direction of increasing longitude;
- Z^n to make a right-handed orthogonal coordinate system.

Horizontal location components in this local frame are called "relative northing" and "relative easting".
The NED system, together with the ECEF system, is shown in Fig. 3.2, where φ denotes the geodetic latitude and λ the geodetic longitude.

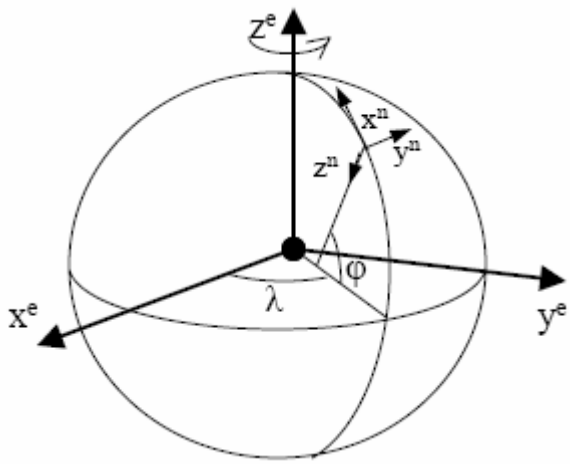

Fig. 3.2 The ECEF and NED coordinate systems

3.1.4 Body frame (*b*-frame)

The body frame represents the orientation of the strapdown IMU which is rigidly mounted to the vehicle. The origin of the system is the center of the IMU, and the orientation of the axes is defined as follows (Fig. 3.3):

- X^b in the nominal direction of motion of the vehicle;
- Y^b out the right-hand side;
- Z^b to make a right-handed orthogonal coordinate system.

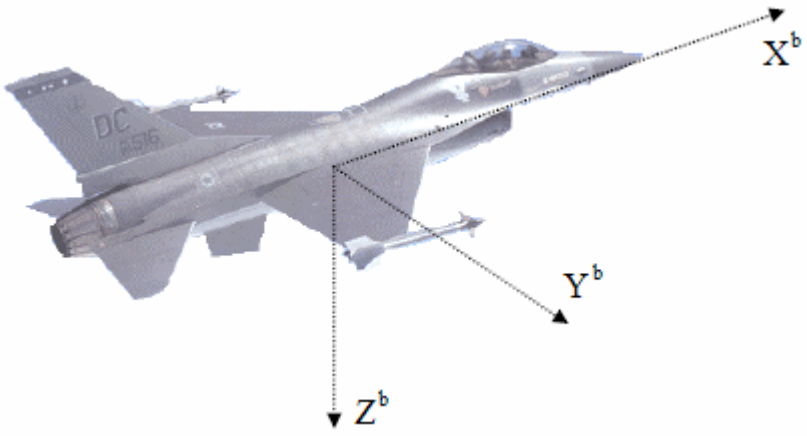

Fig. 3.3 The body frame

3.1.5 Coordinate transformations

Coordinate transformations permit to represent a vector into different coordinate systems. There are several techniques to perform the transformations; probably the simplest one is through the application of an appropriate Direction Cosine Matrix (DCM). The process for the determination of these matrices can be found in several textbooks, such as [15] and [23]; here, only the final expressions will be given.

The DCM from the *e*-frame to the *n*-frame is [24]:

$$R_e^n = \begin{bmatrix} -\sin\varphi\cos\lambda & -\sin\varphi\sin\lambda & \cos\varphi \\ -\sin\lambda & \cos\lambda & 0 \\ -\cos\varphi\cos\lambda & -\cos\varphi\sin\lambda & -\sin\varphi \end{bmatrix} \tag{3-3}$$

The definition of the DCM from the *b*-frame to the *n*-frame requires the introduction of the Euler angles roll, pitch, and yaw. When using Euler angles it is always necessary to specify the order of rotations. A common convention for vehicle attitude Euler angles is shown in Fig. 3.4 where, starting with the vehicle level and having the roll axis pointed North [17]:

1. *Yaw*: rotation through the yaw angle ψ about the vehicle yaw axis to the intended azimuth (heading) of the vehicle roll axis. Azimuth is measured clockwise from North.
2. *Pitch*: rotation through the pitch angle θ about the vehicle pitch axis to bring the vehicle roll axis to its intended elevation. Elevation is measured positive upward from the local horizontal plane.
3. *Roll*: rotation through the roll angle ϕ about the vehicle roll axis to bring the vehicle attitude to the specified orientation.

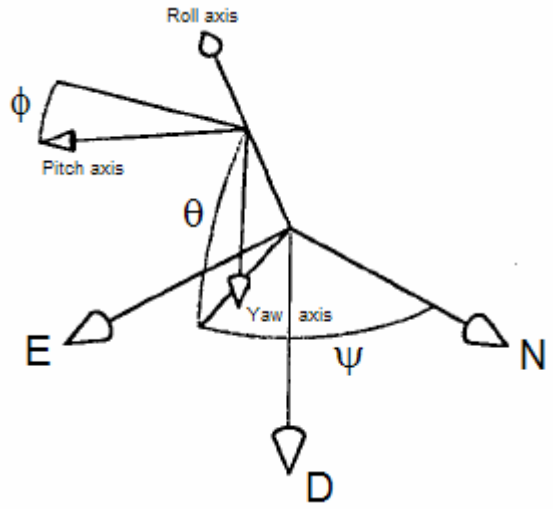

Fig. 3.4 Convention for the vehicle's Euler angles

With the above definition, the DCM from the *b*-frame to the *n*-frame is [5], [17]:

$$R_b^n = \begin{bmatrix} c\theta c\psi & -c\phi s\psi + s\phi s\theta c\psi & s\phi s\psi + c\phi s\theta c\psi \\ c\theta s\psi & c\phi c\psi + s\phi s\theta s\psi & -s\phi c\psi + c\phi s\theta s\psi \\ -s\theta & s\phi c\theta & c\phi c\theta \end{bmatrix} \tag{3-4}$$

where "*sin*" and "*cos*" are shortly denoted as "*s*" and "*c*", respectively.

The Euler angles can be determined from the DCM R_b^n with the following equations [24]:

$$\phi = \arctan 2\left(R_b^n[3,2], R_b^n[3,3]\right) \tag{3-5}$$

$$\theta = -\arcsin\left(R_b^n[3,1]\right) \tag{3-6}$$

$$\psi = \arctan 2\left(R_b^n[2,1], R_b^n[1,1]\right) \tag{3-7}$$

where *arctan2(y, x)* is a four quadrant inverse tangent function.

It is now convenient to use the previously defined DCM R_e^n to transform the rotation vector of the *e*-frame with respect to the *i*-frame projected on the *e*-frame:

$$\underline{\omega}_{ie}^e = \begin{bmatrix} 0 & 0 & \omega_e \end{bmatrix}^T \tag{3-8}$$

where ω_e is the magnitude of the Earth rotation rate (≈ 7.2921155 x 10^{-5} *rad/s*). By projecting this vector to the *n*-frame we obtain

$$\underline{\omega}_{ie}^{n} = R_e^n \underline{\omega}_{ie}^{e} = \begin{bmatrix} \omega_e \cos\varphi & 0 & -\omega_e \sin\varphi \end{bmatrix}^T \tag{3-9}$$

The turn rate of the *n*-frame with respect to the *e*-frame is called transport rate, and is expressed in terms of the rate of change of latitude and longitude [32]:

$$\underline{\omega}_{en}^{n} = \begin{bmatrix} \dot{\lambda}\cos\varphi & -\dot{\varphi} & -\dot{\lambda}\sin\varphi \end{bmatrix}^T \tag{3-10}$$

In order to have Eq. (3-10) as a function of position and velocity, it is necessary to introduce two more parameters, namely, the radii of curvature in the meridian and prime vertical at a given latitude:

$$R_M = \frac{a\left(1-e^2\right)}{\left(1-e^2\sin^2\varphi\right)^{3/2}} \tag{3-11}$$

$$R_N = \frac{a}{\left(1-e^2\sin^2\varphi\right)^{1/2}} \tag{3-12}$$

In the expressions above, *a* = 6378137.0 *m* and *e* = 0.0818 are the semi-major axis length and the eccentricity of the WGS-84 ellipsoid [36], respectively.
We can now express the geodetic latitude and longitude rates as follows [11]:

$$\dot{\phi} = \frac{1}{R_M + h} v_N \tag{3-13}$$

$$\dot{\lambda} = \frac{1}{\left(R_N + h\right)\cos\varphi} v_E \tag{3-14}$$

where h is the geodetic height, and v_N, v_E are velocities in the North and East direction, respectively. By substituting Eqs. (3-13) and (3-14) into Eq. (3-10) we obtain an expression that is function of the position and velocity:

$$\underline{\omega}_{en}^{n} = \begin{bmatrix} v_E / \left(R_N + h\right) \\ -v_N / \left(R_M + h\right) \\ -v_E \tan\varphi / \left(R_N + h\right) \end{bmatrix} \tag{3-15}$$

Finally, the two rotation vectors $\underline{\omega}_{ie}^{n}$ and $\underline{\omega}_{en}^{n}$ can be summed to obtain the rotation vector of the *n*-frame with respect to the *i*-frame (which will be extensively utilized in the following sections):

$$\underline{\omega}_{in}^{n} = \underline{\omega}_{ie}^{n} + \underline{\omega}_{en}^{n} = \begin{bmatrix} \omega_e \cos\varphi + v_E / \left(R_N + h\right) \\ -v_N / \left(R_M + h\right) \\ -\omega_e \sin\varphi - v_E \tan\varphi / \left(R_N + h\right) \end{bmatrix} \tag{3-16}$$

Another coordinate transformation, which also gives results to be used later on (see section 6.6), is the one that converts the ECEF coordinates into geodetic longitude, latitude, and height. The Earth ellipsoidal model defined in the WGS-84 gives different parameters that are required to perform the transformation, namely, the semi-major axis (a), the semi-minor axis (b), the eccentricity (e), and the flattening (f). For a user located in ECEF coordinates (x_u, y_u, z_u), the geodetic latitude, longitude, and height can be determined through the algorithm shown in Tab. 3.1 [25].

Tab. 3.1 Transformation from ECEF to geodetic coordinates

(1)	$r = \sqrt{x_u^2 + y_u^2}$	(9)	$r_0 = -\frac{Pe^2 r}{1+Q} + \sqrt{\frac{1}{2}a^2\left(1+\frac{1}{Q}\right) - \frac{P(1-e^2)z_u^2}{Q(1+Q)} - \frac{1}{2}Pr^2}$
(2)	$E^2 = a^2 - b^2$	(10)	$U = \sqrt{(r - e^2 r_0)^2 + z_u^2}$
(3)	$F = 54 b^2 z_u^2$	(11)	$V = \sqrt{(r - e^2 r_0)^2 + (1-e^2) z_u^2}$
(4)	$G = r^2 + (1-e^2) z_u^2 - e^2 E^2$	(12)	$z_0 = \frac{b^2 z_u}{aV}$
(5)	$c = \frac{e^4 F r^2}{G^3}$	(13)	$h = U\left(1 - \frac{b^2}{aV}\right)$
(6)	$s = \sqrt[3]{1 + c + \sqrt{c^2 + 2c}}$	(14)	$\phi = \arctan\left(\frac{z_u + e'^2 z_0}{r}\right)$
(7)	$P = \frac{F}{3\left(s + \frac{1}{s} + 1\right)^2 G^2}$	(15)	$\lambda = \arctan\frac{y_u}{x_u}$
(8)	$Q = \sqrt{1 + 2e^4 P}$		

In the table, the parameter e' is defined as

$$e' = \sqrt{\left(\frac{a}{b}\right)^2 - 1} = \frac{ae}{b} \tag{3-17}$$

It is possible to observe that while the calculation of the geodetic longitude from ECEF coordinates is immediate, the determination of latitude and height requires more operations. Approximated formulas for the calculation of these two parameters are given by [2] and [17]:

$$\varphi \approx \arctan 2\left[\left(z_u + \frac{e^2 a^2 \sin^3\gamma}{b}\right) \Big/ \left(\xi - e^2 a \cos^3\gamma\right)\right] \tag{3-18}$$

$$h \approx \xi\cos\varphi + \left(z_u + e^2 N \sin\varphi\right)\sin\varphi - N \tag{3-19}$$

where

$$\gamma = \tan^{-1}\left(\frac{a z_u}{b\xi}\right) \tag{3-20}$$

$$\xi = \sqrt{x_u^2 + y_u^2} \tag{3-21}$$

$$N = \frac{a}{\sqrt{1 - e^2 \sin^2\varphi}} \tag{3-22}$$

3.2 INS kinematic equations

The position in the *n*-frame is expressed in geodetic (curvilinear) coordinates:

$$\underline{r}^n = \begin{bmatrix}\varphi & \lambda & h\end{bmatrix}^T \tag{3-23}$$

while the velocities in the *n*-frame are

$$\underline{v}^n = \begin{bmatrix} v_N & v_E & v_D \end{bmatrix}^T \tag{3-24}$$

The INS kinematic equations (or inertial navigation equations) mathematically describe the motion of the vehicle. Their derivation can be broken up into three parts: position, velocity, and attitude equations. The full demonstration can be found in [11] and [32]. The results are reported here:

$$\begin{bmatrix} \dot{\underline{r}}^n \\ \dot{\underline{v}}^n \\ \dot{R}_b^n \end{bmatrix} = \begin{bmatrix} D^{-1}\underline{v}^n \\ R_b^n \underline{f}^b - \left(2\underline{\omega}_{ie}^n + \underline{\omega}_{en}^n\right) \times \underline{v}^n + \underline{g}^n \\ R_b^n \left(\Omega_{ib}^b - \Omega_{in}^b\right) \end{bmatrix} \tag{3-25}$$

where the IMU's measurement inputs are $\underline{f}^b$ and Ω_{ib}^b. The notation used in Eq. (3-25) is described below.

Matrix D^{-1} is a diagonal matrix defined as follows:

$$D^{-1} = \begin{bmatrix} \dfrac{1}{R_M + h} & 0 & 0 \\ 0 & \dfrac{1}{\left(R_N + h\right)\cos\varphi} & 0 \\ 0 & 0 & -1 \end{bmatrix} \tag{3-26}$$

The specific force vector $\underline{f}$ is defined as the difference between the true acceleration in space and the acceleration due to gravity, and it represents the outputs of the accelerometers; the gravity vector is denoted $\underline{g}$.

Finally, matrix Ω represents the skew symmetric matrix form of the vector $\underline{\omega}$; specifically, Ω_{ib}^b represents the outputs of the gyroscopes.

3.3 INS mechanization equations

The mechanization equations convert the output of the IMU, which includes rotation rates and specific force measurements, into position, velocity, and attitude information. The mechanization equations consist of four basic steps [28]:

1. correction of raw data through known or estimated errors;
2. attitude update;
3. transformation of specific force to the navigation frame;
4. calculation of velocity and position.

Note that instead of the measured rates, most IMUs will actually output velocity and angular increments in the body frame ($\Delta\tilde{v}_f^b$ and $\Delta\tilde{\theta}_{ib}^b$, respectively) over the interval t_{k+1}-t_k. Since this does not affect the validity of Eq. (3-25), it will be assumed in the following part, which is mostly taken from [11] and [20].

3.3.1 Correction of raw data

The raw measurements are typically corrupted by errors such as turn-on bias, in-run bias, scale factor errors and other misalignment errors [26]. The values of these errors can be obtained from laboratory or field calibration, or can be estimated during the mission, as will be shown in Chapter 5.
Once the sensor errors are obtained, the measurements can be corrected using Eqs. (3-27) and (3-28) for gyros and accelerometers, respectively:

$$\Delta\underline{\theta}_{ib}^b = \begin{bmatrix} 1/\left(1+S_{gx}\right) & 0 & 0 \\ 0 & 1/\left(1+S_{gy}\right) & 0 \\ 0 & 0 & 1/\left(1+S_{gz}\right) \end{bmatrix} \left(\Delta\underline{\tilde{\theta}}_{ib}^b - \underline{b}_g \Delta t\right) \tag{3-27}$$

$$\Delta\underline{v}_f^b = \begin{bmatrix} 1/\left(1+S_{ax}\right) & 0 & 0 \\ 0 & 1/\left(1+S_{ay}\right) & 0 \\ 0 & 0 & 1/\left(1+S_{az}\right) \end{bmatrix} \left(\Delta\underline{\tilde{v}}_f^b - \underline{b}_a \Delta t\right) \tag{3-28}$$

where

$\underline{b}_a$, $\underline{b}_g$	are the bias instabilities and turn-on-bias for each sensor;
$\underline{S}_a$, $\underline{S}_g$	are the scale factor errors for each sensor;
Δt	is the time increment (t_{k+1}-t_k);
$\Delta\underline{\theta}_{ib}^{b}$	is the measured (raw) angular increment;
$\Delta\underline{v}_{f}^{b}$	is the measured (raw) velocity increment.

3.3.2 Attitude update

The body angular increments with respect to the navigation frame are obtained by

$$\begin{aligned}\Delta\underline{\theta}_{nb}^{b} &= \begin{bmatrix}\Delta\theta_x & \Delta\theta_y & \Delta\theta_z\end{bmatrix}^T = \\ &= \Delta\underline{\theta}_{ib}^{b} - R_n^b\left(\underline{\omega}_{ie}^{n} + \underline{\omega}_{en}^{n}\right)\Delta t\end{aligned} \tag{3-29}$$

where, using the orthogonality of the DCM

$$R_n^b = \left(R_b^n\right)^T \tag{3-30}$$

The computation of the rotation matrix R_b^n from the angular increments is usually done using a quaternion approach, whereby the rotation matrix is expressed by a single rotation angle, $\Delta\theta$, about a fixed spatial axis (see Appendix B for a brief description of the quaternion algebra). The angular increments obtained in Eq. (3-29) are used to update the quaternion vector [14]:

$$\underline{q}_{k+1} = \underline{q}_k + 0.5\begin{bmatrix} c & s\Delta\theta_z & -s\Delta\theta_y & s\Delta\theta_x \\ -s\Delta\theta_z & c & s\Delta\theta_x & s\Delta\theta_y \\ s\Delta\theta_y & -s\Delta\theta_x & c & s\Delta\theta_z \\ -s\Delta\theta_x & -s\Delta\theta_y & -s\Delta\theta_z & c \end{bmatrix}\underline{q}_k \tag{3-31}$$

where

$$s = \frac{2}{\Delta\theta}\sin\frac{\Delta\theta}{2} = 1 - \frac{\Delta\theta^2}{24} + \frac{\Delta\theta^4}{1920} + \cdots \tag{3-32}$$

$$c = 2\left(\cos\frac{\Delta\theta}{2} - 1\right) = -\frac{\Delta\theta^2}{4} + \frac{\Delta\theta^4}{192} + \cdots \tag{3-33}$$

and

$$\Delta\theta = \sqrt{\Delta\theta_x^2 + \Delta\theta_y^2 + \Delta\theta_z^2} \tag{3-34}$$

The DCM R_b^n is then updated as [14]

$$R_b^n = \begin{bmatrix} \left(q_1^2 - q_2^2 - q_3^2 + q_4^2\right) & 2\left(q_1q_2 - q_3q_4\right) & 2\left(q_1q_3 + q_2q_4\right) \\ 2\left(q_1q_2 + q_3q_4\right) & \left(q_2^2 - q_1^2 - q_3^2 + q_4^2\right) & 2\left(q_2q_3 - q_1q_4\right) \\ 2\left(q_1q_3 - q_2q_4\right) & 2\left(q_2q_3 + q_1q_4\right) & \left(q_3^2 - q_1^2 - q_2^2 + q_4^2\right) \end{bmatrix} \tag{3-35}$$

Finally, the vehicle's attitude Euler angles can be determined with Eqs. (3-5) through (3-7).

3.3.3 Transformation of specific force to the n-frame

Before correcting and integrating, the specific force measurements must be rotated from the body frame to the navigation frame:

$$\Delta\underline{v}_f^n = R_b^n \begin{bmatrix} 1 & 0.5\Delta\theta_z & -0.5\Delta\theta_y \\ -0.5\Delta\theta_z & 1 & 0.5\Delta\theta_x \\ 0.5\Delta\theta_y & -0.5\Delta\theta_x & 1 \end{bmatrix} \Delta\underline{v}_f^b \tag{3-36}$$

where the first-order sculling correction is also applied [20].

3.3.4 Calculation of velocity and position

The final velocity increment in the *n*-frame is obtained by applying the Coriolis and gravity corrections:

$$\Delta \underline{v}^n = \Delta \underline{v}_f^n - \left(2\underline{\omega}_{ie}^n + \underline{\omega}_{en}^n\right) \times \underline{v}^n \Delta t + \underline{\gamma}^n \Delta t \tag{3-37}$$

where

$$\underline{\gamma}^n = \begin{bmatrix} 0 & 0 & \gamma \end{bmatrix}^T \tag{3-38}$$

and γ is the normal gravity at the geodetic latitude φ and height h, which can be approximated by the following expression:

$$\gamma = a_1\left(1 + a_2 \sin^2\varphi + a_3 \sin^4\varphi\right) + \left(a_4 + a_5 \sin^2\varphi\right)h + a_6 h^2 \tag{3-39}$$

The values of the coefficients for the gravity model of Eq. (3-39) are listed in Tab. 3.2.

Tab. 3.2 Coefficients for the gravity model (adopted from [32])

Coefficient	Value
a_1	*9.7803267715 (m/s^2)*
a_2	*0.0052790414 (m/s^2)*
a_3	*0.0000232718 (m/s^2)*
a_4	*-0.0000030876910891 (s^{-2})*
a_5	*0.0000000043977311 (s^{-2})*
a_6	*0.0000000000007211 (m^{-1}s^{-2})*

Once the velocity increment is computed, the updated velocity is given by

$$\underline{v}_{k+1}^n = \underline{v}_k^n + \Delta \underline{v}_{k+1}^n \tag{3-40}$$

Finally, using trapezoidal integration, the position can be incremented as

$$\underline{r}_{k+1}^{n} = \underline{r}_{k}^{n} + \frac{1}{2} D^{-1}\left(\underline{v}_{k}^{n} + \underline{v}_{k+1}^{n}\right)\Delta t \tag{3-41}$$

where the expression of D^{-1} is given by Eq. (3-26).

Fig. 3.5 summarizes the overall *n*-frame INS mechanization described in this section.

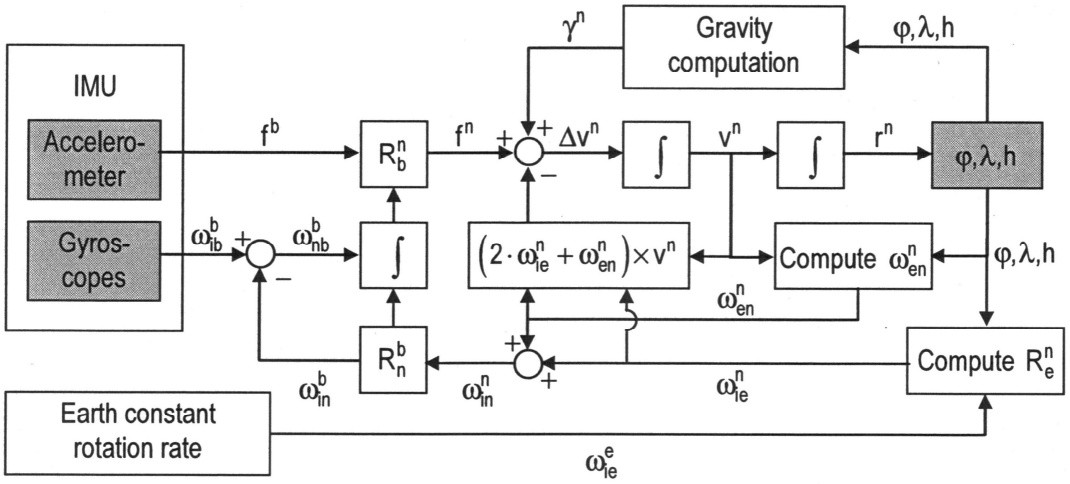

Fig. 3.5 INS mechanization in the *n*-frame (adopted from [31])

3.4 INS error dynamics equations

The error dynamics equations are obtained by perturbing the kinematic equations. These error equations will be necessary to build the INS and INS/GPS Kalman filters (see Chapter 5).

The perturbation of position, velocity, attitude DCM, and gravity can be expressed as

$$\hat{\underline{r}}^{n} = \underline{r}^{n} + \delta\underline{r}^{n} \tag{3-42}$$

$$\hat{\underline{v}}^{n} = \underline{v}^{n} + \delta\underline{v}^{n} \tag{3-43}$$

$$\hat{R}_{b}^{n} = \left(I - E^{n}\right) R_{b}^{n} \tag{3-44}$$

$$\underline{\gamma}^{n} = \underline{g}^{n} + \delta\underline{g}^{n} \tag{3-45}$$

where $\delta \underline{r}^n = \begin{bmatrix} \delta\varphi & \delta\lambda & \delta h \end{bmatrix}^T$ are the position errors described in curvilinear coordinates, $\delta \underline{v}^n = \begin{bmatrix} \delta v_N & \delta v_E & \delta v_D \end{bmatrix}^T$ are Earth referenced velocity errors given in the navigation frame, $\delta \underline{g}$ is the gravity error, and

$$E^n = \left(\underline{\varepsilon}^n \times \right) = \begin{bmatrix} 0 & -\varepsilon_D & \varepsilon_E \\ \varepsilon_D & 0 & -\varepsilon_N \\ -\varepsilon_E & \varepsilon_N & 0 \end{bmatrix} \tag{3-46}$$

is a skew symmetric matrix for the attitude errors.

3.4.1 Position errors

The linearized position error dynamics equation can be obtained by perturbing the first line of Eq. (3-25):

$$\delta \dot{\underline{r}}^n = F_{rr} \delta \underline{r}^n + F_{rv} \delta \underline{v}^n \tag{3-47}$$

where

$$F_{rr} = \begin{bmatrix} \frac{\partial \dot{\varphi}}{\partial \varphi} & \frac{\partial \dot{\varphi}}{\partial \lambda} & \frac{\partial \dot{\varphi}}{\partial h} \\ \frac{\partial \dot{\lambda}}{\partial \varphi} & \frac{\partial \dot{\lambda}}{\partial \lambda} & \frac{\partial \dot{\lambda}}{\partial h} \\ \frac{\partial \dot{h}}{\partial \varphi} & \frac{\partial \dot{h}}{\partial \lambda} & \frac{\partial \dot{h}}{\partial h} \end{bmatrix} = \begin{bmatrix} 0 & 0 & \frac{-v_N}{\left(R_M + h\right)^2} \\ \frac{v_E \sin\varphi}{\left(R_N + h\right)\cos^2\varphi} & 0 & \frac{-v_E}{\left(R_N + h\right)^2 \cos\varphi} \\ 0 & 0 & 0 \end{bmatrix} \tag{3-48}$$

$$F_{rv} = \begin{bmatrix} \frac{\partial \dot{\varphi}}{\partial v_N} & \frac{\partial \dot{\varphi}}{\partial v_E} & \frac{\partial \dot{\varphi}}{\partial v_D} \\ \frac{\partial \dot{\lambda}}{\partial v_N} & \frac{\partial \dot{\lambda}}{\partial v_E} & \frac{\partial \dot{\lambda}}{\partial v_D} \\ \frac{\partial \dot{h}}{\partial v_N} & \frac{\partial \dot{h}}{\partial v_E} & \frac{\partial \dot{h}}{\partial v_D} \end{bmatrix} = \begin{bmatrix} \frac{1}{R_M + h} & 0 & 0 \\ 0 & \frac{1}{\left(R_N + h\right)\cos\varphi} & 0 \\ 0 & 0 & -1 \end{bmatrix} = D^{-1} \tag{3-49}$$

3.4.2 Velocity errors

In order to perturb the velocity equation it is convenient to introduce a simplified model for the gravity vector in which the Earth is assumed spherical and γ varies only with altitude [32]:

$$\gamma = \gamma_0 \left(\frac{R}{R+h} \right)^2 \tag{3-50}$$

where γ_0 is the normal gravity at $h = 0$, and $R = \sqrt{R_M R_N}$.

By perturbing the second line of Eq. (3-25) we obtain the linearized velocity error dynamics equation [11], [32]:

$$\delta \dot{\underline{v}}^n = F_{vr} \delta \underline{r}^n + F_{vv} \delta \underline{v}^n + \left(\underline{f}^n \times \right) \underline{\varepsilon}^n + R_b^n \delta \underline{f}^b \tag{3-51}$$

where

$$F_{vr} = \begin{bmatrix} -2v_E\omega_e \cos\varphi - \dfrac{v_E^2}{(R_N+h)\cos^2\varphi} & 0 & \dfrac{-v_N v_D}{(R_M+h)^2} + \dfrac{v_E^2 \tan\varphi}{(R_N+h)^2} \\ 2\omega_e (v_N \cos\varphi - v_D \sin\varphi) + \dfrac{v_E v_N}{(R_N+h)\cos^2\varphi} & 0 & \dfrac{-v_E (v_D + v_N \tan\varphi)}{(R_N+h)^2} \\ 2v_E\omega_e \sin\varphi & 0 & \dfrac{v_E^2}{(R_N+h)^2} + \dfrac{v_N^2}{(R_M+h)^2} - 2\gamma/(R+h) \end{bmatrix} \tag{3-52}$$

$$F_{vv} = \begin{bmatrix} \dfrac{v_D}{R_M+h} & -2\omega_e \sin\varphi - 2\dfrac{v_E \tan\varphi}{R_N+h} & \dfrac{v_N}{R_M+h} \\ 2\omega_e \sin\varphi + \dfrac{v_E \tan\varphi}{R_N+h} & \dfrac{v_D + v_N \tan\varphi}{R_N+h} & 2\omega_e \cos\varphi + \dfrac{v_E}{R_N+h} \\ -2\dfrac{v_N}{R_M+h} & -2\omega_e \cos\varphi - 2\dfrac{v_E}{R_N+h} & 0 \end{bmatrix} \tag{3-53}$$

In Eq. (3-51) $\delta \underline{f}^b$ is the perturbation of the specific force vector in the body frame.

3.4.3 Attitude errors

Finally, the linearized attitude error dynamics equation can be written as [11], [32]:

$$\dot{\underline{\varepsilon}}^n = F_{er}\delta \underline{r}^n + F_{ev}\delta \underline{v}^n - \left(\underline{\omega}_{in}^n \times\right)\underline{\varepsilon}^n - R_b^n \delta \underline{\omega}_{ib}^b \tag{3-54}$$

where

$$F_{er} = \begin{bmatrix} -\omega_e \sin\varphi & 0 & \dfrac{-v_E}{\left(R_N + h\right)^2} \\ 0 & 0 & \dfrac{v_N}{\left(R_M + h\right)^2} \\ -\omega_e \cos\varphi - \dfrac{v_E}{\left(R_N + h\right)\cos^2\varphi} & 0 & \dfrac{v_E \tan\varphi}{\left(R_N + h\right)^2} \end{bmatrix} \tag{3-55}$$

$$F_{ev} = \begin{bmatrix} 0 & \dfrac{1}{R_N + h} & 0 \\ \dfrac{-1}{R_M + h} & 0 & 0 \\ 0 & \dfrac{-\tan\varphi}{R_N + h} & 0 \end{bmatrix} \tag{3-56}$$

In Eq. (3-54) $\delta\underline{\omega}_{ib}^b$ is the perturbation of the angular rate vector of the *b*-frame relative to the *i*-frame expressed in the *b*-frame.

3.5 Inertial sensor errors

Despite remarkable advances of MEMS technology in cost and size constraints, MEMS-based inertial sensors have inherited the error behavior of conventional inertial sensors [26]. Gyroscope errors will result in errors in the transformation matrix between body and navigation frames, whereas accelerometer errors will lead to errors in the integrated velocity and position. The integration yields errors proportional to the integration time, t, and to its square, t^2, respectively for velocity and position.

Since calibration significantly increases the manufacturing cost, low-cost inertial sensors are rarely calibrated by the manufacturer [33]. Therefore sensor errors need to be modeled in the state vector of the navigation filter in addition to position, velocity, and attitude errors.

The primary sources of error for both gyros and accelerometers include:

1. *Bias*, which is a non-zero sensor output when the input is zero; bias drift after turn-on needs to be conveniently modeled (usually as a random walk or first-order Gauss-Markov process).
2. *Scale factor error*, which represents a non-constant sensor gain (or sensitivity) often resulting from aging or manufacturing tolerances; it can vary during the sensor operation, especially for low-cost IMUs, therefore it also has to be modeled with an appropriate stochastic process.
3. *Non-orthogonality errors*, which are the results of a misalignment of the sensor axes caused by imperfections in the construction of the sensor assembly. Most stand-alone INS implementations include an initial period for alignment of the attitude direction cosines [17]; however, a GPS-aided alignment is also possible, where the axes misalignments are modeled as part of the INS error dynamics equations (it is the vector $\underline{\varepsilon}^n$ previously introduced).
4. *Random noise*, which is an additional signal resulting from the sensor itself or other electronic equipment that interfere with the output signal being measured. It is usually modeled as a zero-mean white Gaussian noise.

The measurement equations for accelerometers and gyros, with the addition of the error sources described above, are given by

$$\tilde{\underline{f}}^b = \underline{f}^b + \underline{b}_a + diag\left(\underline{f}^b\right)\underline{S}_a + \underline{w}_a \tag{3-57}$$

$$\tilde{\underline{\omega}}_{ib}^b = \underline{\omega}_{ib}^b + \underline{b}_g + diag\left(\underline{\omega}_{ib}^b\right)\underline{S}_g + \underline{w}_g \tag{3-58}$$

where $\underline{w}$ is the sensor random noise. The description of the stochastic processes commonly used to model these errors is given in section 4.4.

3.6 INS alignment

INS alignment is the process of aligning the stable platform axes parallel to navigation coordinates (for gimbaled systems) or that of determining the initial values of the coordinate transformations from sensor coordinates to navigation coordinates (for strapdown systems) [17]. Several methods of alignment are used for aircraft:

- *Gyrocompass alignment*: it is performed on stationary vehicles; it uses the sensed direction of acceleration to determine the local vertical and the sensed direction of rotation to determine the North. In such way, latitude can be determined by the angle between the Earth rotation vector and the horizontal; longitude must be determined by other means and entered manually. This method is inexpensive, but the most time consuming (requires several minutes, typically).
- *Transfer alignment*: some vehicles contain a high quality inertial navigation system and one or more lower-cost units [20]; transfer alignment is the process of matching the slave platforms to the master using natural or deliberately-induced maneuvers of the vehicle. This method is typically several times faster than gyrocompass alignment, but it requires another INS on the vehicle and it might also need special

maneuvering to achieve complete observability of the alignment variables.

- *Optical alignment*: an inertial system can be aligned relative to an external optical line of sight, for example using a ground-based theodolite and a mirror on the platform. It is usually impractical on aircraft because of the necessity for optical access and the inconvenience of establishing theodolite sites. However, optical alignment can be used in conjunction with platforms that have star-trackers mounted on the stable element (typical for space applications).
- *GPS-aided alignment*: it uses position matching with GPS to estimate alignment variables. It does not require the vehicle to remain stationary during alignment, but there will be some period of time after turn-on (a few minutes, typically) before the system navigation errors can settle to acceptable values [17].

3.7 Description of IMUs

After having illustrated and discussed the equations, algorithms, and operations involved in the determination of position, velocity, and attitude through an INS, the final section of this chapter briefly describes the implementations and technologies that are currently adopted for IMUs, with particular focus on MEMS-based inertial sensors.

3.7.1 Inertial sensors

As previously mentioned, an IMU is a self-contained unit constituted by a set of inertial sensors, namely, gyroscopes and accelerometers, which give the outputs required for the computation of the navigation solution. In this subsection, the main features of these types of sensors are described.

A gyroscope is a device for measuring or maintaining orientation, traditionally based on the principle of conservation of angular momentum. Although a great

variety of technologies and implementations exist (see sections 3.7.2 and 3.7.3), a conventional mechanical gyroscope is a rigid body similar to a wheel with one principal moment of inertia larger than the other two (Fig. 3.6). The wheel spins about the axis of maximum inertia, and it responds to a force applied about the input axis by a reaction force about the output axis. The three axes are orthogonal, and this cross-axis response is the essence of the well-known gyroscopic effect. More recent gyroscopes are based on physical principles that are not of mechanical nature, as will be seen later on.

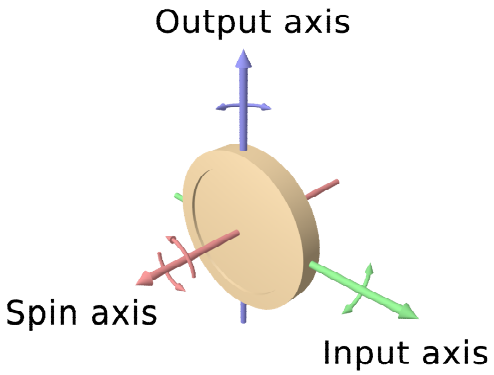

Fig. 3.6 Simple representation of the conventional mechanical gyroscope

The other type of inertial sensors that form an IMU are the accelerometers, which are devices based on Newton's second law and capable to determine the three-dimensional acceleration vector. The great majority of accelerometers has in common that their mechanical sensing element consists of a proof mass attached by a suspension system to a reference frame, as shown in Fig. 3.7.

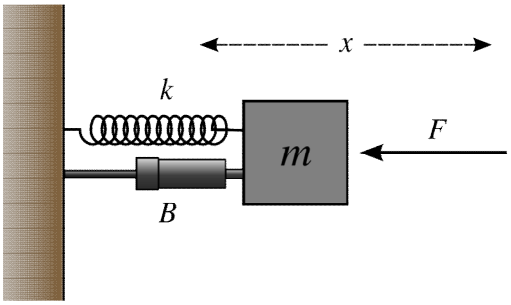

Fig. 3.7 Simple representation of the conventional mechanical accelerometer

An inertial force will deflect the proof mass; by measuring the magnitude of the force (directly or indirectly, such as through the mass displacement) it is

possible to calculate the acceleration. This common principle, although being very simple, allows a wide range of sensor designs, as described in section 3.7.3.

3.7.2 Implementations

Two different implementation approaches are possible: gimbaled systems and strapdown systems.

In a gimbaled system, a stable platform is mechanically isolated from the rotations of the host vehicle by a set of three or (preferably) four gimbals, as shown in Fig. 3.8-a. Each gimbal is a ring with orthogonal inside and outside pivot axes. These are connected inside one another, with the innermost gimbal attached to the stable platform, and the outermost gimbal attached to the vehicle. A sensor cluster of three accelerometers and three gyroscopes is rigidly mounted to the stable platform. The input axes of the inertial sensors are parallel to the pivot axes. The gyroscopes are used to sense any rotation of the platform, and their outputs are used in servo feedback loops to command gimbal pivot torque actuators in order to maintain the platform stable (i.e. aligned with a specific navigation coordinate system). If this is achieved, then the platform does not experience any rotation relative to the navigation frame, in spite of vehicle motion. The accelerometers, aligned with the platform, measure the specific force in the navigation frame; scaling and integrating this measurement yields the desired navigation frame position and velocity vectors. Vehicle attitude is determined by measuring the relative angles between the vehicle and the platform axes. A fourth gimbal is desirable for vehicles such as missiles or high-performance aircraft with full freedom of rotation about all three axes. The reason is to avoid the alignment of two gimbal axes, in a condition called “gimbal lock”. In fact, in such situation, the third gimbal alone is not able to isolate the platform from rotations; thus, an additional gimbal is required.

Strapdown systems attach the inertial sensors directly to the vehicle frame, possibly with shock isolators in order to limit rotational vibrations [17]. In this approach, the sensors experience the full dynamic motion of the vehicle. Therefore, higher bandwidth (possibly noisier) rate gyros with a higher dynamic

range are required [11]. Because of the increased dynamic range, gyro scale factor errors and nonlinearity become increasingly important. In addition, the relationship among the vehicle frame, the navigation frame, and the inertial frame must be maintained computationally, thus increasing the on-board computational load (relative to that of a gimbaled system).

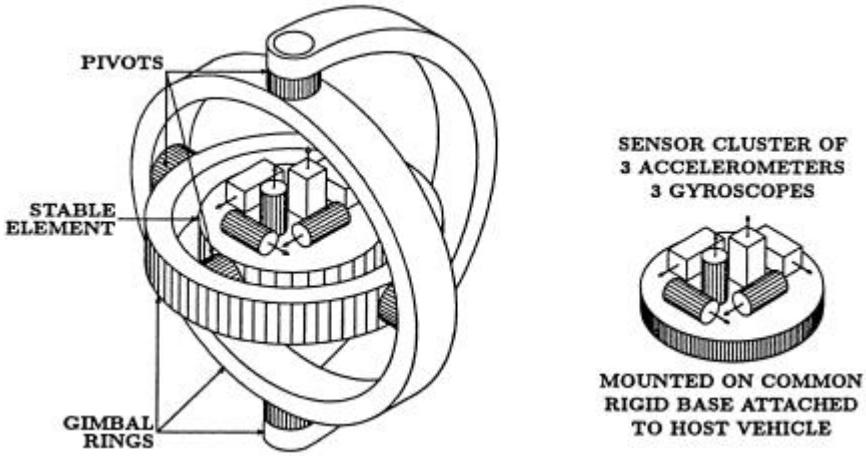

(a) Gimbaled **(b) Strapdown**

Fig. 3.8 Possible implementations of an IMU

Upon their first introduction, the feasibility of strapdown systems was debated because of the restrictive gyro dynamic response specifications and the computational requirements, especially in applications in which inertial-only (i.e. unaided) position accuracy was required for long durations [11]. Gimbaled systems have smaller computational loads and expose the inertial sensors to a more benign environment, but are typically larger, heavier, and more expensive than strapdown systems because of the actuation mechanism. Advances in sensor and computer technologies over the past decades have resulted in a general shift toward strapdown systems even for stand-alone INSs requiring high accuracy for long periods of time, since this implementation is inexpensive, small in size, and is also characterized by low power requirements.

3.7.3 Sensor technologies

Some of the sensor technologies used for inertial navigation are presented in Tab. 3.3. Many more exist, but these can serve at least to illustrate the great diversity of technologies applied in this field.

Tab. 3.3 Some basic inertial sensor technologies (adopted from [17])

Sensor	Gyroscope			Accelerometer		
Physical principle used	Conservation of angular momentum	Coriolis effect	Sagnac effect	Gyroscopic precession	Electro-magnetic force	Strain under load
Sensor implementation methods	Angular displacement	Vibration	Ring laser	Angular displacement	Drag cup	Piezo-electric
	Torque rebalance	Rotation	Fiber optic	Torque rebalance	Electro-magnetic	Piezo-resistive

Whereas a description of all these type of sensors cannot be presented here, some details about MEMS-based inertial sensors will be given.

Micromachined inertial sensors have been the subject of intensive research for over two decades. Many authors have published works about MEMS-based sensors and a huge amount of developed solutions are reported in literature.

Concerning the micromachined accelerometers, a common factor is that the displacement of the proof mass has to be sensed by a position-measuring interface circuit, and it is then converted into an electrical signal [4]. Many types of sensing mechanism have been reported, such as capacitive, piezoresistive, piezoelectric, optical, resonant, and tunneling current, each one having distinct advantages and drawbacks; the first three are the most commonly used [4]. The characteristics and performance of any MEMS-accelerometer are greatly influenced by the position measurement interface, and, in general, the main requirements are low noise, high linearity, good dynamic response, and low power consumption. Ideally, the interface circuit should be represented by a simple gain block, relating the displacement of the proof mass to an electrical signal.

The IMU analyzed in this work (which will be described in detail in section 5.2.2.1) contains three micromachined accelerometers (called ADXL) based on a capacitive principle; therefore, a more specific description of this type of

sensors is given here. Fig. 3.9 illustrates the working principle of these accelerometers. The sensor's fixed electrodes are differentially excited by square waves equal in amplitude but 180º out of phase. If the proof mass is not deflected, the two capacitors are matched and the resulting output voltage of the buffer is zero. If the proof mass is displaced from the center, the amplitude of the buffer voltage is proportional to the mismatch in capacitance. The buffer voltage is demodulated and amplified by an instrumentation amplifier referenced to a constant voltage (with a typical value of 1.8 *V*); this signal is fed back to the proof mass through an isolation resistor (of typically 3 *MΩ*). This results in an electrostatic force that maintains the proof mass virtually motionless over the dynamic range.

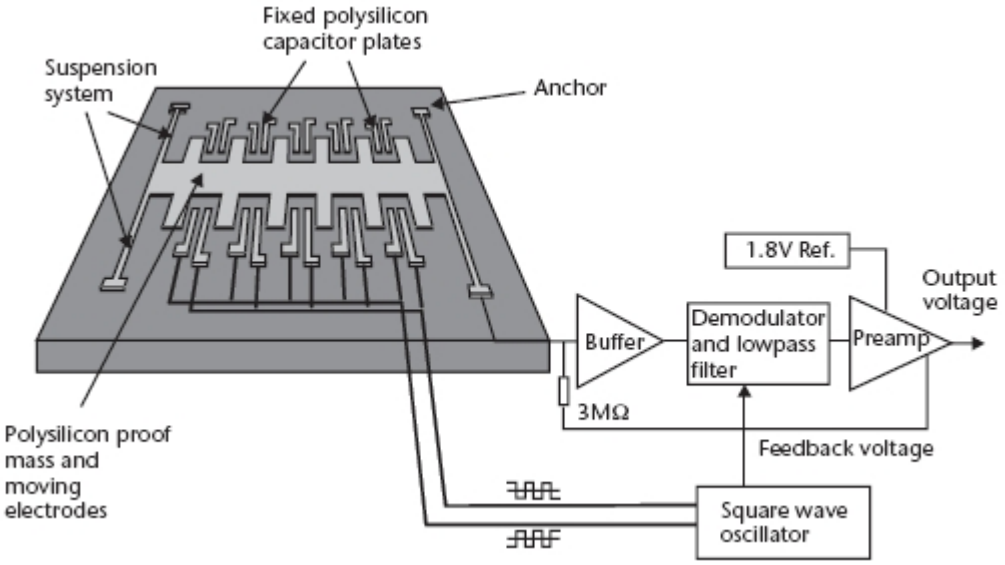

Fig. 3.9 Working principle of an ADXL MEMS-capacitive accelerometer

Micromachined gyroscopes typically rely on a mechanical structure that is driven into resonance exciting a secondary oscillation in either the same structure or in a second one, due to the Coriolis force [4]. The amplitude of this secondary oscillation is directly proportional to the angular rate signal to be measured. A great variety of implementations exist for MEMS-gyroscopes as well.

The gyroscopes inside the IMU studied in this thesis belong to a particular family called ADXRS. In these gyroscopes, a sensing structure contains a so called "dither frame" that is driven electrostatically to resonance. In reality, each

gyroscope contains two identical structures in order to reject environmental shock and vibration [4]. Fig. 3.10 shows one structure schematically. A rotation about the axis orthogonal to the plane of the structure produces a Coriolis force that displaces an inner frame perpendicular to the vibratory motion. This Coriolis motion is detected by a series of capacitive “fingers” positioned on the edges of the inner and outer frames. The resulting signal is amplified and demodulated to produce the rate signal output.

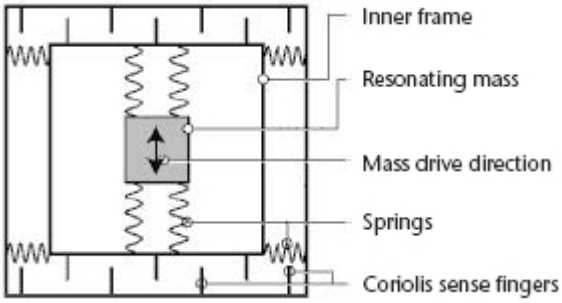

Fig. 3.10 Scheme of one of the two structures of an ADXRS MEMS-gyro

3.7.4 Classification of IMUs

It is common to categorize the IMUs based on their accuracy (or grade). Tab. 3.4 illustrates the characteristics of different grade IMUs, giving the order of magnitude of the sensor biases and some typical applications in which they are involved.

Tab. 3.4 The categories of IMUs

Grade	**Strategic**	**Navigation**	**Tactical**	**Automotive**
Positional error	*< 30 m/hr*	*1-4 km/hr*	*20-40 km/hr*	*2 km/min*
Accelerometer bias (μg)	*1*	*50-500*	*500-1000*	*>1200*
Gyro bias (deg/hr)	*0.0001*	*0.005-0.01*	*0.1-10*	*>100*
Price	*>200k US $*	*50k~200k US $*	*10k~50k US $*	*<10k US $*
Applications	*Military platforms, submarines, Intercontinental Ballistic Missiles (ICBM)*	*General navigation applications, high accuracy georeferencing*	*Short time applications*	*Short time applications*

Low-cost MEMS-IMUs can be included in the automotive grade category, since their specifications hardly meet the requirements of a tactical grade unit. However, their considerably lower price, together with the physical characteristics of size and weight, justify the great interest and the huge amount of study and research that is being done on these sensors in the last few years. In terms of cost, MEMS-IMUs are surely a favorable option for the use in future commercial applications.

Some examples of commercial IMUs available on the international market are shown in Tab. 3.5. Since the quality of an IMU is often evaluated by the quality of the gyros contained in the sensor system, the following table gives an overview of some commercial IMUs categorized as function of the gyro bias and the corresponding price. For each IMU is given the company name, the model, the typical gyro bias and the price. The background colors correspond to the different IMU's categories shown in Tab. 3.4. Most of the information below has been collected through an internet research.

Tab. 3.5 Some examples of commercial IMUs

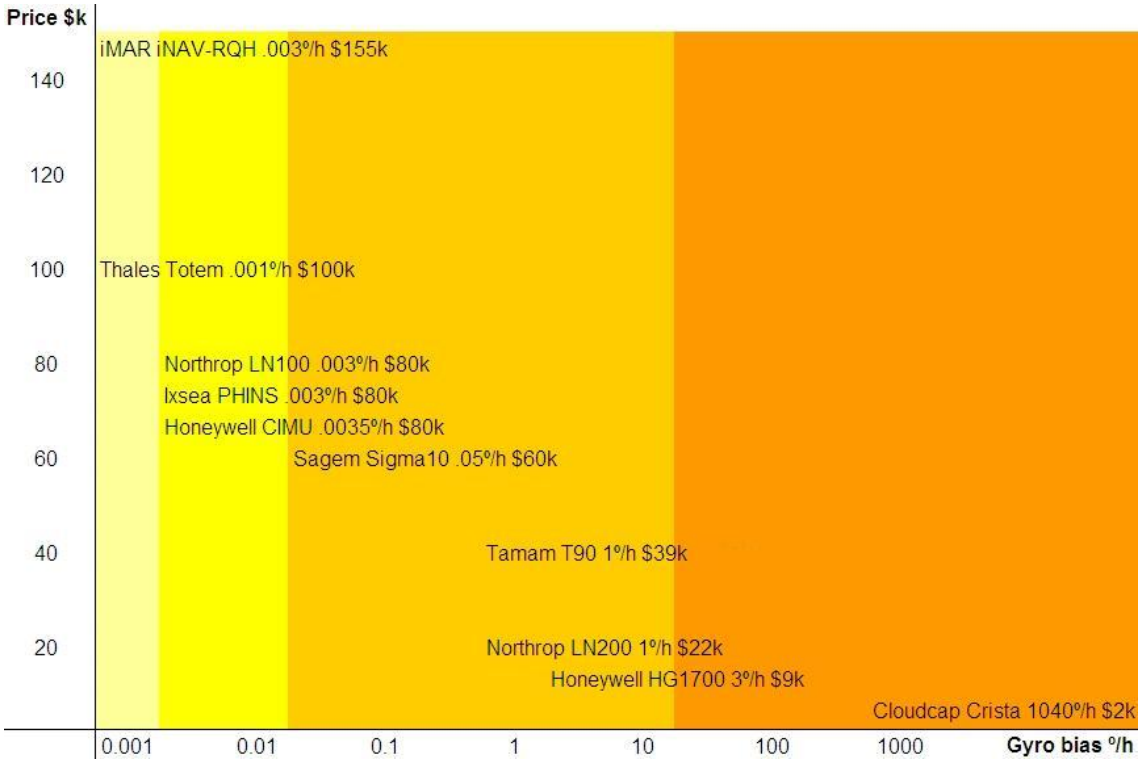

Chapter 4

Linear and Extended Kalman Filter

Since its introduction in 1960, the Kalman filter has become an integral component in thousands of military and civilian navigation systems [16], [21]. It is an extremely effective and versatile procedure for combining noisy sensor outputs to estimate the state of a system with uncertain dynamics. The filter uses statistical models to properly weight each new measurement relative to the past information.

This chapter describes the Kalman filter algorithm and its nonlinear version, known as extended Kalman filter. An overview of the characteristics of discrete-time systems is given, followed by the description of the filter equations. The last part provides some information on the stochastic processes that are commonly used to model the non-deterministic behavior of inertial sensors.

4.1 Discrete-time linear systems

According to the linear system theory, the dynamics of a linear system can be represented by a vector differential equation:

$$\dot{\underline{x}}(t) = F(t)\,\underline{x}(t) + G(t)\,\underline{w}(t) \tag{4-1}$$

where

- $\underline{x}(t)$ is an *n x 1* state vector;
- $F(t)$ is an *n x n* system dynamic matrix;
- $G(t)$ is an *n x p* noise-input mapping matrix;
- $\underline{w}(t)$ is a *p x 1* system noise vector.

The observation of the linear system is performed according to the linear measurement equation:

$$\underline{z}(t) = H(t)\,\underline{x}(t) + \underline{v}(t) \tag{4-2}$$

where

$\underline{z}(t)$ is an *m x 1* observation vector;

$H(t)$ is an *m x n* design matrix;

$\underline{v}(t)$ is an *m x 1* measurement noise vector.

The covariances of the noise vectors are given by

$$E\left[\underline{w}(t)\,\underline{w}(\tau)^T\right] = Q(t)\,\delta(t-\tau) \tag{4-3}$$

$$E\left[\underline{v}(t)\,\underline{v}(\tau)^T\right] = R(t)\,\delta(t-\tau) \tag{4-4}$$

where $Q(t)$ and $R(t)$ are respectively the system noise and the measurement noise covariance matrices, and the operator $\delta(\cdot)$ denotes the Dirac delta function.

Since the IMU's measurements consist of sampled data, the continuous-time system is to be transformed to its corresponding discrete-time form:

$$\underline{x}_{k+1} = \Phi_k\,\underline{x}_k + \underline{w}_k \tag{4-5}$$

$$\underline{z}_k = H_k\,\underline{x}_k + \underline{v}_k \tag{4-6}$$

where *k* denotes an epoch t_k, and Φ_k is the state transition matrix. The relationship between the state transition matrix and the dynamic matrix is [16]:

$$\Phi_k = e^{F(t_k)\Delta t} = I + F(t_k)\,\Delta t + \frac{\left(F(t_k)\,\Delta t\right)^2}{2} + \cdots \tag{4-7}$$

where I is the identity matrix and Δt is the length of the sampling interval.

The covariance matrix Q_k associated to the discrete-time noise vector $\underline{w}_k$ can be determined by the following approximated expression [33]:

$$Q_k \approx \frac{1}{2}\left[\Phi_k G(t_k) Q(t_k) G^T(t_k) + G(t_k) Q(t_k) G^T(t_k) \Phi_k^T\right] \Delta t \tag{4-8}$$

4.2 Kalman filter

The Kalman filter is a recursive algorithm that uses a series of predictions and measurement update steps to obtain an optimal estimate of the state vector in the sense of minimizing the mean square errors. This algorithm assumes that the process $\underline{x}(t)$ to be estimated, defined by Eq. (4-1), can be modeled in discrete time by Eq. (4-5), and the measurement of the process occurs at discrete points in time in accordance with the relationship given in Eq. (4-6). It further assumes that the dynamics noise $\underline{w}_k$, and the measurement noise $\underline{v}_k$ have white noise characteristics (i.e. zero-mean and zero-correlation).

The equations in the Kalman filter algorithm fall under two groups. The first group of equations predict the state (and the associated covariance) of the system, based on the current state and the assumed system model, in order to obtain an *a priori* estimate for the next time step, as indicated by

$$\underline{\hat{x}}(k+1|k) = \Phi_k \underline{\hat{x}}(k|k) \tag{4-9}$$

$$P(k+1|k) = \Phi_k P(k|k) \Phi_k^T + Q_k \tag{4-10}$$

where $P(k+1|k)$ and $P(k|k)$ are the error covariance matrices associated with the estimated state vector at the prediction and time update steps, respectively.

The second group of equations updates the predicted states and covariance estimates with the currently available measurements in accordance to the measurement model:

$$\underline{\hat{x}}(k|k) = \underline{\hat{x}}(k|k-1) + K_k\left[\underline{z}_k - H_k \underline{\hat{x}}(k|k-1)\right] \tag{4-11}$$

$$P(k|k) = [I - K_k H_k] P(k|k-1) \tag{4-12}$$

The term $\left[\underline{z}_k - H_k \underline{\hat{x}}(k|k-1)\right]$ in Eq. (4-11) is called the innovation sequence; it is the difference between the actual observation and the predicted observation, thus it represents the amount of new information introduced into the system by the actual measurement.

The Kalman gain matrix, K_k, is a weighting factor indicating how much of the new information contained in the innovation sequence should be accepted by the system. As such, the gain matrix is optimized to produce a minimum error variance, and its expression is given by

$$K_k = P(k|k-1) H_k^T \left[H_k P(k|k-1) H_k^T + R_k \right]^{-1} \tag{4-13}$$

To start the Kalman filter suitable values are assigned to the state vector estimate $\underline{\hat{x}}(1|0)$ and to the error covariance matrix $P(1|0)$.

A complete demonstration of the above equations can be found in several textbooks, such as [6], [16], and [17].

Fig. 4.1 illustrates the block diagram of the Kalman filter, including the system model and the measurement model.

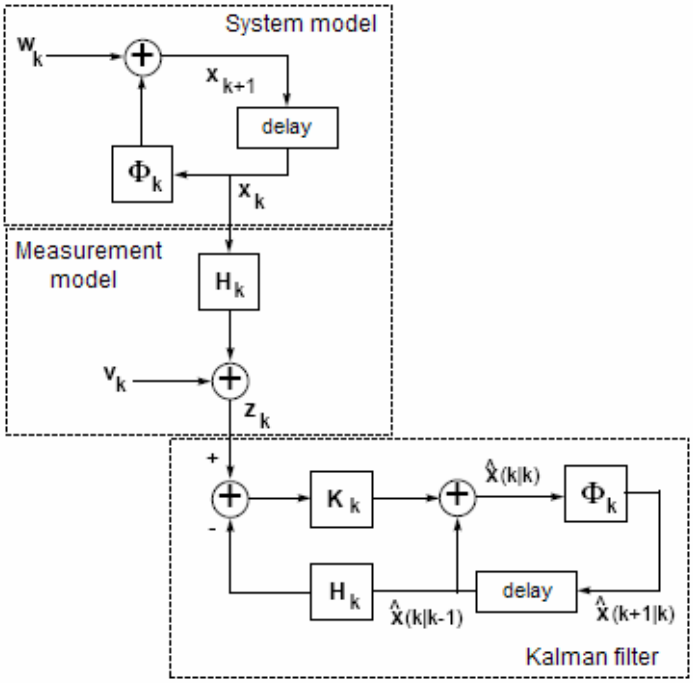

Fig. 4.1 Block diagram of the Kalman filter algorithm

4.3 Extended Kalman filter

Although the Kalman filter is defined for linear dynamic systems with linear measurements, it has been often used in applications without truly linear dynamics or measurements, and usually with remarkable success [17].
The nonlinear (continuous) system equations and the nonlinear (discrete) measurement equations can be written as

$$\dot{\underline{x}}(t) = \underline{f}\left[\underline{x}(t)\right] + G(t)\,\underline{w}(t) \tag{4-14}$$

$$\underline{z}_k = \underline{h}\left[\underline{x}(t_k)\right] + \underline{v}_k \tag{4-15}$$

The Kalman filter corresponding to Eqs. (4-14) and (4-15) is constituted by the following set of equations:

- Prediction step

$$\hat{\underline{x}}(k+1\,|\,k) = \hat{\underline{x}}(k\,|\,k) + \int_{t_k}^{t_{k+1}} \underline{f}\left[\hat{\underline{x}}(t\,|\,t_k)\right] dt \tag{4-16}$$

$$F_k = \left.\frac{\partial \underline{f}}{\partial \underline{x}}\right|_{\underline{x}=\hat{\underline{x}}} \tag{4-17}$$

$$P(k+1\,|\,k) = \Phi_k P(k\,|\,k)\Phi_k^T + Q_k \qquad (\Phi_k \approx I + F_k \Delta t) \tag{4-18}$$

- Update step

$$\hat{\underline{x}}(k\,|\,k) = \hat{\underline{x}}(k\,|\,k-1) + K_k\left(\underline{z}_k - \underline{h}\left[\hat{\underline{x}}(k\,|\,k-1)\right]\right) \tag{4-19}$$

$$H_k = \left.\frac{\partial \underline{h}}{\partial \underline{x}}\right|_{\underline{x}=\hat{\underline{x}}} \tag{4-20}$$

$$P(k\,|\,k) = \left[I - K_k H_k\right] P(k\,|\,k-1) \tag{4-21}$$

$$K_k = P(k\,|\,k-1)\,H_k^T\left[H_k P(k\,|\,k-1)\,H_k^T + R_k\right]^{-1} \tag{4-22}$$

The major differences from the conventional Kalman filter equations are:

1. integration of the nonlinear integrand $\underline{f}\left[\underline{\hat{x}}(t \mid t_k)\right]$, $t > t_k$, to predict $\underline{\hat{x}}(k+1 \mid k)$;
2. use of the nonlinear function $\underline{h}\left[\underline{\hat{x}}(k \mid k-1)\right]$ in the measurement updates;
3. use of the Jacobian matrix of the dynamic model function $\underline{f}$ as the dynamic coefficient matrix F_k in the propagation of the covariance matrix;
4. use of the Jacobian matrix of the measurement function $\underline{h}$ as the measurement sensitivity matrix H_k in the covariance correction and Kalman gain equations;
5. contrarily to the linear Kalman filter, the covariance matrices $P(k \mid k)$ and $P(k \mid k-1)$ of the EKF do not give the error covariances of the estimated state vectors $\underline{\hat{x}}(k \mid k)$ and $\underline{\hat{x}}(k \mid k-1)$. In fact, the EKF is not optimal and it may even diverge.

4.4 Stochastic processes

The fundamental noise processes in the basic Kalman filter model are zero-mean white Gaussian noise processes. However, the physical noise processes of the real world applications (either the dynamic disturbance or the sensor noise) do not need to be necessarily uncorrelated in order to apply Kalman filtering [17].
The most typical stochastic processes used to model the dynamics of the inertial sensor errors are briefly described in the following subsections.

4.4.1 White noise

White noise is defined as a stationary random process having a constant spectral density function, which implies the power is uniformly distributed over all frequency components in the full infinite range; thus, this process is not

physically realizable. However, white noise is a very useful approximation to situations in which a disturbing noise is wideband compared with the bandwidth of the system. A number of random processes can be generated by passing white noise through a suitable filter.

4.4.2 Random Walk

Random walk, also called Wiener process, is defined as the integral of the white noise, with initial zero conditions:

$$\dot{\eta}(t) = w(t), \qquad \eta(0) = 0 \tag{4-23}$$

where $w(t)$ is white noise with power spectral density q. The uncertainty of the random walk increases with time [32]:

$$E\left[\eta(t)^2\right] = qt \tag{4-24}$$

therefore it is a non-stationary process. The corresponding discrete-time form is a cumulative sum of white noise:

$$\eta_{k+1} = \eta_k + w_k, \qquad w_k = \int_{t_k}^{t_k+\Delta t} w(t)\,dt \tag{4-25}$$

where the covariance of η_k is

$$q_k = q\Delta t \tag{4-26}$$

4.4.3 Random constant

The random constant is a non-dynamic quantity with a fixed random amplitude; its continuous and discrete expressions are given respectively by

$$\dot{\eta}(t) = 0, \quad \eta(0) = \eta_0 \tag{4-27}$$

$$\eta_{k+1} = \eta_k \tag{4-28}$$

Non-orthogonalities of sensor triads can be considered as random constants during calibration, and also biases if the operation time is short [32].

4.4.4 First-order Gauss-Markov process

Gauss-Markov process is a general designation for all those random processes obtained through any linear operation performed on a Gaussian random variable. In this work the main interest is focused on a specific class of stationary processes, known as first-order Gauss-Markov processes, which have an exponentially decaying correlation. For a process with correlation time T, mean squared value σ^2, and zero-mean, the model is described by

$$\dot{\eta}(t) = -\frac{1}{T}\eta(t) + w(t) \tag{4-29}$$

The autocorrelation function is

$$R_\eta(t) = \sigma^2 e^{-\frac{|\tau|}{T}} \tag{4-30}$$

with $\sigma^2 = qT/2$, where q is the power spectral density of $w(t)$.

The power spectral density of this process is

$$G_\eta(t) = \frac{qT^2}{1+4\pi^2 f^2 T^2} = \frac{2\sigma^2/T}{1+4\pi^2 f^2 T^2} \tag{4-31}$$

The corresponding discrete-time form of this process and of its spectral density are given respectively by

$$\eta_{k+1} = e^{-\Delta t/T}\eta_k + w_k \tag{4-32}$$

$$q_k = \sigma^2\left(1 - e^{-2\Delta t/T}\right) \tag{4-33}$$

The first-order Gauss-Markov process is important because it fits a large number of physical processes with reasonable accuracy, and it has a relatively simple mathematical description [32].

4.4.5 Summary of stochastic processes

In summary, all of the random processes described in the previous sections can be generally written as:

$$\eta_{k+1} = a\eta_k + w_k \tag{4-34}$$

where a is an appropriate model parameter. The following table summarizes the main characteristics of each process that has been presented.

Tab. 4.1 Summary of stochastic processes

	a	q_k
Random walk	*1*	$q\Delta t$
Random constant	*1*	*0*
First-order Gauss-Markov	$e^{-\Delta t/T}$	$\sigma^2(1-e^{-2\Delta t/T})$

Chapter 5

INS/GPS Integration

While the main features of GPS and INS have been reviewed in Chapters 2 and 3, respectively, this chapter deals with the theoretical and practical aspects of integrating the two systems. First, the most common INS/GPS strategies are presented, with detailed descriptions of specific Kalman filter designs. In the last section, the integration methods previously described are compared in terms of several aspects, with particular focus on the computational loads.

5.1 Integration strategies

Numerous approaches are possible for the integration of GPS and INS information to provide a combined navigation solution. Differences between the various approaches are based on the type of information that is shared between the individual systems. In practice, two main integration approaches are implemented in the navigation field: the loosely coupled (LC) and tightly coupled (TC) schemes. Both the strategies can be open-loop, where the estimation of the INS errors does not interfere with the operation of the INS, or closed loop, where the sensor errors are compensated within the calculation procedure of the INS mechanization algorithm (see section 3.3.1).
The main characteristics of each of these approaches are discussed in the following sections.

5.2 Loosely coupled integration

The loosely coupled integration scheme is illustrated in Fig. 5.1.

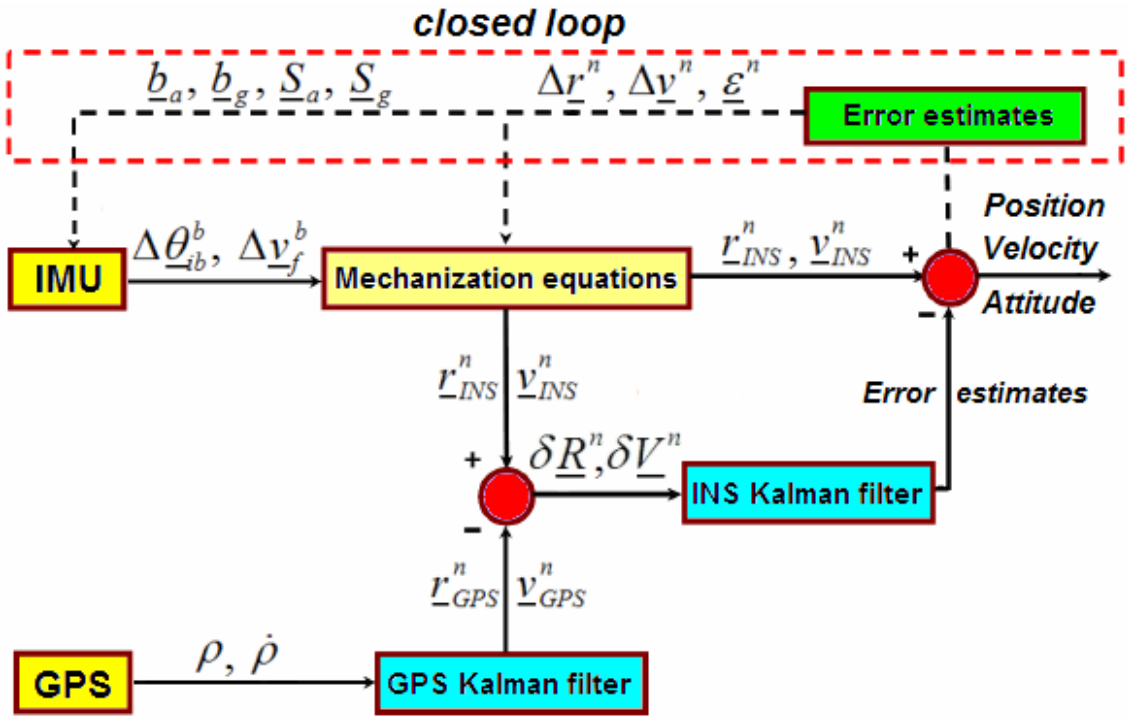

Fig. 5.1 Loosely coupled integration scheme (adopted from [14])

In a loosely coupled integrated system, the GPS receiver has its own Kalman filter (GPS filter) to process pseudorange and Doppler measurements which are used to calculate the user position and velocity. The differences between the INS and GPS calculated positions and velocities are utilized as measurements for a second Kalman filter (INS filter) in which the INS error dynamics equations are used as system model. In this way, the INS filter provides estimates of all the observable INS errors, which are consequently used to correct the INS raw measurements and to compensate the system output.

Next we describe the GPS filter and the INS filter of the scheme of Fig. 5.1. Note that the GPS filter is an extended Kalman filter and the INS filter is a (linear) Kalman filter.

5.2.1 GPS filter

A PV (Position-Velocity) model is typically used for low dynamics applications; in case of high dynamics, it can be replaced by a PVA (Position-Velocity-Acceleration) model. Previous investigations have shown that, in general, there

is no significant difference in the performance of these two models when considering land or maritime applications; in such situations, either one can be used for GPS-based positioning [28]. However, for airborne applications, where considerable accelerations may be experienced, this could not be necessarily true. Therefore, in this work both the two models have been implemented and their performance has been compared (see section 7.3).

5.2.1.1 Receiver clock model

Regardless of the chosen filter (PV or PVA), it is always necessary to model the GPS receiver clock bias. Physically, the clock bias develops as the integral of the frequency error of the receiver clock oscillator [11]. This physical process suggests a two-state clock model, as shown in Fig. 5.2.

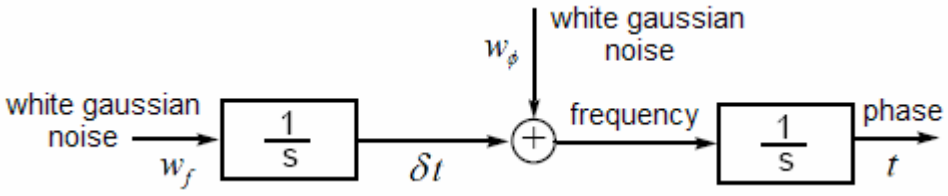

Fig. 5.2 Model for the receiver clock bias

The corresponding state-space form can be written as

$$\begin{bmatrix} \dot{t} \\ \dot{\delta t} \end{bmatrix} = \begin{bmatrix} 0 & 1 \\ 0 & 0 \end{bmatrix} \begin{bmatrix} t \\ \delta t \end{bmatrix} + \begin{bmatrix} w_\phi \\ w_f \end{bmatrix} \tag{5-1}$$

where

t is the clock offset error (*s*);

δt is the clock drift error;

w_ϕ is the clock error driving noise with spectral density q_ϕ;

w_f is the clock drift error driving noise with spectral density q_f.

To complete the clock error model, the spectral densities of the driving noise processes must be specified. This can be accomplished by using the Allan variance parameters which define the physical characteristics of the clock [6]. Two simplified expressions are given by

$$q_\phi \approx \frac{h_0}{2} \tag{5-2}$$

$$q_f \approx 2\pi^2 h_{-2} \tag{5-3}$$

Tab. 5.1 shows some typical values of the Allan variance parameters for different types of clock used in GPS receivers. These values are given in units of seconds; when used for range errors they must be multiplied by the square of the speed of light [6].

Tab. 5.1 Typical Allan variance parameters for various GPS receiver clocks

Clock	h_0	h_{-2}
Compensated* crystal	2×10^{-19}	2×10^{-20}
Ovenized crystal	8×10^{-20}	4×10^{-23}
Rubidium	2×10^{-20}	4×10^{-29}

*Compensation is for temperature variations

5.2.1.2 System model

It is now possible to define the two models for the GPS filter. The block diagram of the PV model for each spatial coordinate (r_x, r_y or r_z) is shown in Fig. 5.3. The state vector includes position, velocity, and the clock errors. Velocity is modeled as a random walk process, while positions are simply the integral of velocity.

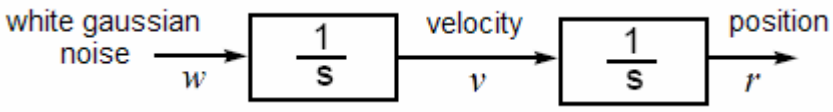

Fig. 5.3 PV model for GPS-only filter

The state vector is

$$\underline{x} = \begin{bmatrix} \underline{r}^n & \underline{v}^n & t & \delta t \end{bmatrix}^T \tag{5-4}$$

and has 8 components (state variables). The corresponding state-space form is given by

$$\underbrace{\begin{bmatrix} \dot{\underline{r}}^n \\ \dot{\underline{v}}^n \\ \dot{t} \\ \dot{\delta t} \end{bmatrix}}_{\dot{\underline{x}}} = \underbrace{\begin{bmatrix} 0_{3x3} & I_{3x3} & 0_{3x1} & 0_{3x1} \\ 0_{3x3} & 0_{3x3} & 0_{3x1} & 0_{3x1} \\ 0_{1x3} & 0_{1x3} & 0 & 1 \\ 0_{1x3} & 0_{1x3} & 0 & 0 \end{bmatrix}}_{F} \underbrace{\begin{bmatrix} \underline{r}^n \\ \underline{v}^n \\ t \\ \delta t \end{bmatrix}}_{\underline{x}} + \underbrace{\begin{bmatrix} 0_{3x3} & 0_{3x1} & 0_{3x1} \\ I_{3x3} & 0_{3x1} & 0_{3x1} \\ 0_{1x3} & 1 & 0 \\ 0_{1x3} & 0 & 1 \end{bmatrix}}_{G} \underbrace{\begin{bmatrix} \underline{w}_v \\ w_\phi \\ w_f \end{bmatrix}}_{\underline{w}} \tag{5-5}$$

where $\underline{w}_v$ is the process driving noise with spectral density $\underline{q}_v$. The noise covariance matrix associated to this model is

$$Q = \begin{bmatrix} diag\left(\underline{q}_v\right) & 0_{3x1} & 0_{3x1} \\ 0_{1x3} & q_\phi & 0 \\ 0_{1x3} & 0 & q_f \end{bmatrix} \tag{5-6}$$

In the PVA model, displayed in Fig. 5.4 for a single spatial coordinate, instead of a pure random walk process, the acceleration is usually modeled as a first-order Gauss-Markov process, since accelerations are usually correlated over short time intervals [11].

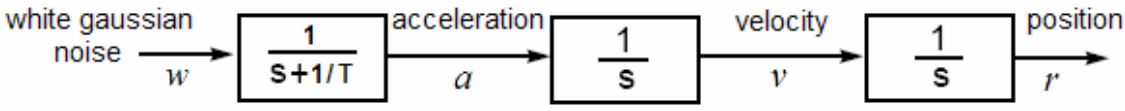

Fig. 5.4 PVA model for GPS-only filter

The state vector is

$$\underline{x} = \begin{bmatrix} \underline{r}^n & \underline{v}^n & \underline{a}^n & t & \delta t \end{bmatrix}^T \tag{5-7}$$

and has 11 components. The corresponding state-space form is

$$\underbrace{\begin{bmatrix} \dot{\underline{r}}^n \\ \dot{\underline{v}}^n \\ \dot{\underline{a}}^n \\ \dot{t} \\ \delta\dot{t} \end{bmatrix}}_{\dot{\underline{x}}} = \underbrace{\begin{bmatrix} 0_{3x3} & I_{3x3} & 0_{3x3} & 0_{3x1} & 0_{3x1} \\ 0_{3x3} & 0_{3x3} & I_{3x3} & 0_{3x1} & 0_{3x1} \\ 0_{3x3} & 0_{3x3} & -diag(T) & 0_{3x1} & 0_{3x1} \\ 0_{1x3} & 0_{1x3} & 0_{1x3} & 0 & 1 \\ 0_{1x3} & 0_{1x3} & 0_{1x3} & 0 & 0 \end{bmatrix}}_{F} \underbrace{\begin{bmatrix} \underline{r}^n \\ \underline{v}^n \\ \underline{a}^n \\ t \\ \delta t \end{bmatrix}}_{\underline{x}} + \underbrace{\begin{bmatrix} 0_{3x3} & 0_{3x1} & 0_{3x1} \\ 0_{3x3} & 0_{3x1} & 0_{3x1} \\ I_{3x3} & 0_{3x1} & 0_{3x1} \\ 0_{1x3} & 1 & 0 \\ 0_{1x3} & 0 & 1 \end{bmatrix}}_{G} \underbrace{\begin{bmatrix} \underline{w}_a \\ w_\phi \\ w_f \end{bmatrix}}_{\underline{w}} \quad (5\text{-}8)$$

and the noise covariance matrix associated to this model is expressed as

$$Q = \begin{bmatrix} diag\left(\underline{q}_a\right) & 0_{3x1} & 0_{3x1} \\ 0_{1x3} & q_\phi & 0 \\ 0_{1x3} & 0 & q_f \end{bmatrix} \quad (5\text{-}9)$$

The discrete-time form for both models, necessary for software implementation, can be easily obtained by using Eqs. (4-7) and (4-8).

5.2.1.3 Measurement model

The pseudorange and Doppler measurements for the *i*-satellite can be related to the receiver position and velocity through the following expressions [22]:

$$\rho^i = \left\| \underline{r}^n_{sat,i} - \underline{r}^n \right\| + ct + w^i \quad (5\text{-}10)$$

$$\dot{\rho}^i = \frac{\left(\underline{r}^n_{sat,i} - \underline{r}^n\right)\left(\underline{v}^n_{sat,i} - \underline{v}^n\right)}{\left\| \underline{r}^n_{sat,i} - \underline{r}^n \right\|} + c\delta t + \dot{w}^i \quad (5\text{-}11)$$

These equations are nonlinear, thus need to be linearized in order to be used in the Kalman filter algorithm. Assuming that *n* satellites are visible, the following linearized matrices can be defined:

$$H_{rr} = \begin{bmatrix} \frac{\partial \rho^1}{\partial r_x} & \frac{\partial \rho^1}{\partial r_y} & \frac{\partial \rho^1}{\partial r_z} \\ \vdots & \vdots & \vdots \\ \frac{\partial \rho^n}{\partial r_x} & \frac{\partial \rho^n}{\partial r_y} & \frac{\partial \rho^n}{\partial r_z} \end{bmatrix} \tag{5-12}$$

$$H_{vr} = \begin{bmatrix} \frac{\partial \dot{\rho}^1}{\partial r_x} & \frac{\partial \dot{\rho}^1}{\partial r_y} & \frac{\partial \dot{\rho}^1}{\partial r_z} \\ \vdots & \vdots & \vdots \\ \frac{\partial \dot{\rho}^n}{\partial r_x} & \frac{\partial \dot{\rho}^n}{\partial r_y} & \frac{\partial \dot{\rho}^n}{\partial r_z} \end{bmatrix} \tag{5-13}$$

$$H_{vv} = \begin{bmatrix} \frac{\partial \dot{\rho}^1}{\partial v_x} & \frac{\partial \dot{\rho}^1}{\partial v_y} & \frac{\partial \dot{\rho}^1}{\partial v_z} \\ \vdots & \vdots & \vdots \\ \frac{\partial \dot{\rho}^n}{\partial v_x} & \frac{\partial \dot{\rho}^n}{\partial v_y} & \frac{\partial \dot{\rho}^n}{\partial v_z} \end{bmatrix} \tag{5-14}$$

where the linearization point is the predicted state estimate at a particular epoch.

For the PV model, the measurement equation can be written as

$$\underbrace{\begin{bmatrix} \underline{\rho} \\ \underline{\dot{\rho}} \end{bmatrix}}_{\underline{z}} = \underbrace{\begin{bmatrix} H_{rr} & 0_{nx3} & c_{nx1} & 0_{nx1} \\ H_{vr} & H_{vv} & 0_{nx1} & c_{nx1} \end{bmatrix}}_{H} \underbrace{\begin{bmatrix} \underline{r}^n \\ \underline{v}^n \\ t \\ \delta t \end{bmatrix}}_{\underline{x}} + \underbrace{\begin{bmatrix} \underline{w} \\ \underline{\dot{w}} \end{bmatrix}}_{\underline{v}} \tag{5-15}$$

Similarly, for the PVA model, we can write

$$\underbrace{\begin{bmatrix} \underline{\rho} \\ \underline{\dot{\rho}} \end{bmatrix}}_{\underline{z}} = \underbrace{\begin{bmatrix} H_{rr} & 0_{nx3} & 0_{nx3} & c_{nx1} & 0_{nx1} \\ H_{vr} & H_{vv} & 0_{nx3} & 0_{nx1} & c_{nx1} \end{bmatrix}}_{H} \underbrace{\begin{bmatrix} \underline{r}^n \\ \underline{v}^n \\ \underline{a}^n \\ t \\ \delta t \end{bmatrix}}_{\underline{x}} + \underbrace{\begin{bmatrix} \underline{w} \\ \underline{\dot{w}} \end{bmatrix}}_{\underline{v}} \tag{5-16}$$

The measurement noise covariance matrix is the same for both models:

$$R = \begin{bmatrix} diag\left(\sigma_{\rho}^{2}\right) & 0_{nxn} \\ 0_{nxn} & diag\left(\sigma_{\dot{\rho}}^{2}\right) \end{bmatrix} \tag{5-17}$$

where σ_{ρ}^{2} and $\sigma_{\dot{\rho}}^{2}$ are weights assigned to pseudorange and Doppler measurements. The simplest choice is to assign equal weights to all measurements (for example, using the UERE parameter). However, as it was shown in section 2.6, this is not a realistic option because for a user near or on the Earth's surface, operation at low elevation angles can lead to increased random errors caused by multipath and ionospheric/tropospheric delay effects. Therefore, it is desirable to adopt a model that takes into consideration these effects, such as the one given by Eq. (2-8).

5.2.2 INS filter

The model for the INS filter is based on the INS error dynamics equations presented in section 3.4. Before giving the details of the filter design, it is necessary to outline the characteristics of the specific stochastic processes used to model the INS errors.

5.2.2.1 Inertial sensor error models

The basic inertial sensor errors have been presented in section 3.5, where the measurement equations for accelerometers and gyros were also shown. These are rewritten here for convenience:

$$\underline{\tilde{f}}^{b} = \underline{f}^{b} + \underline{b}_{a} + diag\left(\underline{f}^{b}\right)\underline{S}_{a} + \underline{w}_{a} \tag{5-18}$$

$$\underline{\tilde{\omega}}_{ib}^{b} = \underline{\omega}_{ib}^{b} + \underline{b}_{g} + diag\left(\underline{\omega}_{ib}^{b}\right)\underline{S}_{g} + \underline{w}_{g} \tag{5-19}$$

The bias error for low-cost sensors is typically the sum of a constant offset (turn-on bias) and a non-constant variation (bias drift or in-run bias), as indicated by the following expression:

$$\underline{b}_x(t) = \underline{b}_{tob,x} + \delta\underline{b}_x(t) \tag{5-20}$$

where

$\underline{b}_{tob,x}$ is the turn-on bias for sensor *x*;

$\delta\underline{b}_x(t)$ is the bias drift for sensor *x*.

The turn-on bias, although being constant during a single operation, varies from turn-on to turn-on; in order to avoid a field calibration process for determining its value before each utilization, an adequate model for this error can be included into the INS filter as well, so that the Kalman filter algorithm will provide an estimate of its value. According to the nature of this type of error, the most suitable stochastic process to represent it mathematically is a random constant:

$$\dot{\underline{b}}_{tob,x}(t) = 0 \tag{5-21}$$

The in-run bias variation can be modeled with several types of processes; in this work, a first-order Gauss-Markov process has been used:

$$\delta\dot{\underline{b}}_x(t) = -\frac{1}{T_{b,x}}\delta\underline{b}_x(t) + \underline{w}_{b,x}(t) \tag{5-22}$$

The scale factor error is generally constant during the operation. However, for low-cost MEMS-based IMUs it can present some slow variations with time. Thus, it can be modeled as a first-order Gauss-Markov process as well, with a large correlation time [13]:

$$\dot{\underline{S}}_x(t) = -\frac{1}{T_{s,x}}\underline{S}_x(t) + \underline{w}_{s,x}(t) \tag{5-23}$$

Finally, the random noise is simply modeled as a zero-mean white Gaussian noise.

The characteristics of the error models described above are listed in Tab. 5.2 and are taken from [14]. They have been obtained through an auto-correlation analysis conducted with static data of a Crista IMU from Cloud Cap Technology, shown in Fig. 5.5. Since this low-cost MEMS-based IMU is the one considered for the simulations presented in Chapter 7, a brief description of the main features of this specific sensor are given below.

The Crista IMU consists of a three axes inertial sensor which uses MEMS ADXRS gyroscopes and ADXL accelerometers (see section 3.7.3) mounted on orthogonal axes to provide 300*º/s* rate and 10*g* acceleration data. All measurements are temperature-compensated and are provided at a rate greater than 200 *Hz*. An in-built GPS PPS (Pulse Per Second) signal interface allows synchronization of IMU and GPS data. The IMU is small in size (2.05''x1.55''x1.00'') and weighs only 36.8 grams. According to the source, this sensor is available in single quantities for under $2000 US. Factory specifications for this IMU are included in Appendix C.

Fig. 5.5 Crista IMU from Cloud Cap Technology

Tab. 5.2 Crista IMU characteristics assumed for numerical simulations

Crista IMU			
	x	**y**	**z**
Accelerometers			
Turn-on bias	*0.480 m/s²*	*0.260 m/s²*	*0.480 m/s²*
Bias drift*	*0.007 m/s²*	*0.007 m/s²*	*0.009 m/s²*
	227 s	*211 s*	*365 s*
Scale factor error*	*10000 ppm*	*10000 ppm*	*10000 ppm*
	18000 s	*18000 s*	*18000 s*
Random noise	*0.28 mg/√Hz*	*0.40 mg/√Hz*	*0.28 mg/√Hz*
Gyros			
Turn-on bias	*4230 º/h*	*1800 º/h*	*1800 º/h*
Bias drift*	*211 º/h*	*205 º/h*	*161 º/h*
	382 s	*375 s*	*297 s*
Scale factor error*	*10000 ppm*	*10000 ppm*	*10000 ppm*
	18000 s	*18000 s*	*18000 s*
Random noise	*226 º/h/√Hz*	*177 º/h/√Hz*	*165 º/h/√Hz*

* Parameters of first-order Gauss-Markov processes

5.2.2.2 System model

The INS error dynamics equations together with the INS error models form the system model for a 27-state Kalman filter. The state vector is

$$\underline{x} = \left[\delta \underline{r}^n \quad \delta \underline{v}^n \quad \underline{\varepsilon}^n \quad \delta \underline{b}_a \quad \delta \underline{b}_g \quad \underline{b}_{tob,a} \quad \underline{b}_{tob,g} \quad \underline{S}_a \quad \underline{S}_g \right]^T \tag{5-24}$$

and has 27 components which are:

$\delta \underline{r}^n$ position error vector;

$\delta \underline{v}^n$ velocity error vector;

$\underline{\varepsilon}^n$ attitude error vector;

$\delta \underline{b}_a$ accelerometers bias drift vector;

$\delta \underline{b}_g$ gyros bias drift vector;

$\underline{b}_{tob,a}$ accelerometers turn-on bias vector;

$\underline{b}_{tob,g}$ gyros turn-on bias vector;

$\underline{S}_a$ accelerometers scale factor error vector;

$\underline{S}_g$ gyros scale factor error vector.

The system model for the INS filter is characterized by the following vectors and matrices.

$$F = \begin{bmatrix} F_{rr} & F_{rv} & 0_{3x3} & 0_{3x3} & 0_{3x3} & 0_{3x3} & 0_{3x3} & 0_{3x3} & 0_{3x3} \\ F_{vr} & F_{vv} & \left(\underline{f}^{n}\times\right) & R_b^n & 0_{3x3} & R_b^n & 0_{3x3} & R_b^n diag\left(\underline{f}^{b}\right) & 0_{3x3} \\ F_{er} & F_{ev} & -\left(\underline{\omega}_{in}^{n}\times\right) & 0_{3x3} & -R_b^n & 0_{3x3} & -R_b^n & 0_{3x3} & -R_b^n diag\left(\underline{\omega}_{ib}^{b}\right) \\ 0_{3x3} & 0_{3x3} & 0_{3x3} & -diag\left(1/T_{b,a}\right) & 0_{3x3} & 0_{3x3} & 0_{3x3} & 0_{3x3} & 0_{3x3} \\ 0_{3x3} & 0_{3x3} & 0_{3x3} & 0_{3x3} & -diag\left(1/T_{b,g}\right) & 0_{3x3} & 0_{3x3} & 0_{3x3} & 0_{3x3} \\ 0_{3x3} & 0_{3x3} & 0_{3x3} & 0_{3x3} & 0_{3x3} & 0_{3x3} & 0_{3x3} & 0_{3x3} & 0_{3x3} \\ 0_{3x3} & 0_{3x3} & 0_{3x3} & 0_{3x3} & 0_{3x3} & 0_{3x3} & 0_{3x3} & 0_{3x3} & 0_{3x3} \\ 0_{3x3} & 0_{3x3} & 0_{3x3} & 0_{3x3} & 0_{3x3} & 0_{3x3} & -diag\left(1/T_{s,a}\right) & 0_{3x3} & \\ 0_{3x3} & 0_{3x3} & 0_{3x3} & 0_{3x3} & 0_{3x3} & 0_{3x3} & 0_{3x3} & -diag\left(1/T_{s,g}\right) & \end{bmatrix} \quad (5\text{-}25)$$

$$\underline{w} = \begin{bmatrix} \underline{w}_a & \underline{w}_g & \underline{w}_{b,a} & \underline{w}_{b,g} & \underline{w}_{s,a} & \underline{w}_{s,g} \end{bmatrix}^T \quad (5\text{-}26)$$

$$G = \begin{bmatrix} 0_{3x3} & 0_{3x3} & 0_{3x3} & 0_{3x3} & 0_{3x3} & 0_{3x3} \\ R_b^n & 0_{3x3} & 0_{3x3} & 0_{3x3} & 0_{3x3} & 0_{3x3} \\ 0_{3x3} & -R_b^n & 0_{3x3} & 0_{3x3} & 0_{3x3} & 0_{3x3} \\ 0_{3x3} & 0_{3x3} & I_{3x3} & 0_{3x3} & 0_{3x3} & 0_{3x3} \\ 0_{3x3} & 0_{3x3} & 0_{3x3} & I_{3x3} & 0_{3x3} & 0_{3x3} \\ 0_{3x3} & 0_{3x3} & 0_{3x3} & 0_{3x3} & 0_{3x3} & 0_{3x3} \\ 0_{3x3} & 0_{3x3} & 0_{3x3} & 0_{3x3} & 0_{3x3} & 0_{3x3} \\ 0_{3x3} & 0_{3x3} & 0_{3x3} & 0_{3x3} & I_{3x3} & 0_{3x3} \\ 0_{3x3} & 0_{3x3} & 0_{3x3} & 0_{3x3} & 0_{3x3} & I_{3x3} \end{bmatrix} \quad (5\text{-}27)$$

$$Q = \begin{bmatrix} diag\left(\underline{q}_a\right) & 0_{3x3} & 0_{3x3} & 0_{3x3} & 0_{3x3} & 0_{3x3} \\ 0_{3x3} & diag\left(\underline{q}_g\right) & 0_{3x3} & 0_{3x3} & 0_{3x3} & 0_{3x3} \\ 0_{3x3} & 0_{3x3} & diag\left(\underline{q}_{b,a}\right) & 0_{3x3} & 0_{3x3} & 0_{3x3} \\ 0_{3x3} & 0_{3x3} & 0_{3x3} & diag\left(\underline{q}_{b,g}\right) & 0_{3x3} & 0_{3x3} \\ 0_{3x3} & 0_{3x3} & 0_{3x3} & 0_{3x3} & diag\left(\underline{q}_{s,a}\right) & 0_{3x3} \\ 0_{3x3} & 0_{3x3} & 0_{3x3} & 0_{3x3} & 0_{3x3} & diag\left(\underline{q}_{s,g}\right) \end{bmatrix} \quad (5\text{-}28)$$

The covariance matrix Q_k associated to the discrete-time model is calculated with the approximated formula of Eq. (4-8). However, this approximation does not account for any of the correlations between the components of the driving noise $\underline{w}_k$ that develop over the course of a sampling period because of the integration of the continuous-time driving noise $\underline{w}$ through the state dynamics [11]. Let $\|Q_k\|$ be the (Frobenius) norm of matrix Q_k, with

$$\|Q_k\| = \left(\sum_{i,j}^{n} q_{ij}^2 \right)^{1/2} \tag{5-29}$$

where q_{ij} are the entries of Q_k and n is its order. If $\|Q_k\|$ is larger than the real norm, the Kalman filter trusts the measurement more than the system, with the result of noisy estimates due to the free passage of the measurement noise; if the norm of Q_k is smaller than the real one, the solution will show a time lag, and might even diverge causing numerical instabilities [32]. Therefore, for low-cost systems, Q_k must be selected pessimistically so that the trajectory can follow that of GPS. In this work, the elements of Q_k have been manually increased until the filter stabilized and the trajectory could follow that of the GPS.

5.2.2.3 Measurement model

In the loosely coupled integration the measurement for the INS filter is the difference between the INS and the GPS navigation solutions (position and velocity) calculated separately and independently by the two systems. The measurement vector and the design matrix are given respectively by

$$\underline{z} = \begin{bmatrix} \delta \underline{R}^n \\ \delta \underline{V}^n \end{bmatrix} = \begin{bmatrix} \underline{r}^n_{INS} - \underline{r}^n_{GPS} \\ \underline{v}^n_{INS} - \underline{v}^n_{GPS} \end{bmatrix} = \begin{bmatrix} \varphi_{INS} - \varphi_{GPS} \\ \lambda_{INS} - \lambda_{GPS} \\ h_{INS} - h_{GPS} \\ \underline{v}^n_{INS} - \underline{v}^n_{GPS} \end{bmatrix} \tag{5-30}$$

$$H = \begin{bmatrix} I_{3x3} & 0_{3x3} & 0_{3x3} & 0_{3x3} & 0_{3x3} & 0_{3x3} & 0_{3x3} & 0_{3x3} & 0_{3x3} \\ 0_{3x3} & I_{3x3} & 0_{3x3} & 0_{3x3} & 0_{3x3} & 0_{3x3} & 0_{3x3} & 0_{3x3} & 0_{3x3} \end{bmatrix} \tag{5-31}$$

However, this approach causes numerical instabilities in calculating the term $\left(H_k P(k \mid k-1) H_k^T + R_k\right)^{-1}$ in the Kalman gain Eq. (4-13), because φ and λ are in radians and therefore they are very small values [32]. A simple solution is to multiply the first two rows by $\left(R_M + h\right)$ and $\left(R_N + h\right)\cos\varphi$, respectively:

$$\underline{z} = \begin{bmatrix} \left(R_M + h\right)\left(\varphi_{INS} - \varphi_{GPS}\right) \\ \left(R_N + h\right)\cos\varphi\left(\lambda_{INS} - \lambda_{GPS}\right) \\ h_{INS} - h_{GPS} \\ \underline{v}_{INS}^n - \underline{v}_{GPS}^n \end{bmatrix} \tag{5-32}$$

$$H = \left[\begin{array}{ccc|cccccccc} R_M + h & 0 & 0 & & & & & & & \\ 0 & \left(R_N + h\right)\cos\varphi & 0 & 0_{3x3} & 0_{3x3} & 0_{3x3} & 0_{3x3} & 0_{3x3} & 0_{3x3} & 0_{3x3} & 0_{3x3} \\ 0 & 0 & 1 & & & & & & & \\ \hline & 0_{3x3} & & I_{3x3} & 0_{3x3} & 0_{3x3} & 0_{3x3} & 0_{3x3} & 0_{3x3} & 0_{3x3} & 0_{3x3} \end{array}\right] \tag{5-33}$$

Finally, the measurement noise covariance matrix is given by

$$R = \begin{bmatrix} \sigma_\varphi^2 & 0 & 0 & 0 & 0 & 0 \\ 0 & \sigma_\lambda^2 & 0 & 0 & 0 & 0 \\ 0 & 0 & \sigma_h^2 & 0 & 0 & 0 \\ 0 & 0 & 0 & \sigma_{V_N}^2 & 0 & 0 \\ 0 & 0 & 0 & 0 & \sigma_{V_E}^2 & 0 \\ 0 & 0 & 0 & 0 & 0 & \sigma_{V_D}^2 \end{bmatrix} \tag{5-34}$$

where the values of the individual weights depend on the accuracy of the GPS solution.

5.3 Tightly coupled integration

A second strategy to perform the INS/GPS integration is the tightly coupled approach, whose implementation is illustrated in Fig. 5.6.

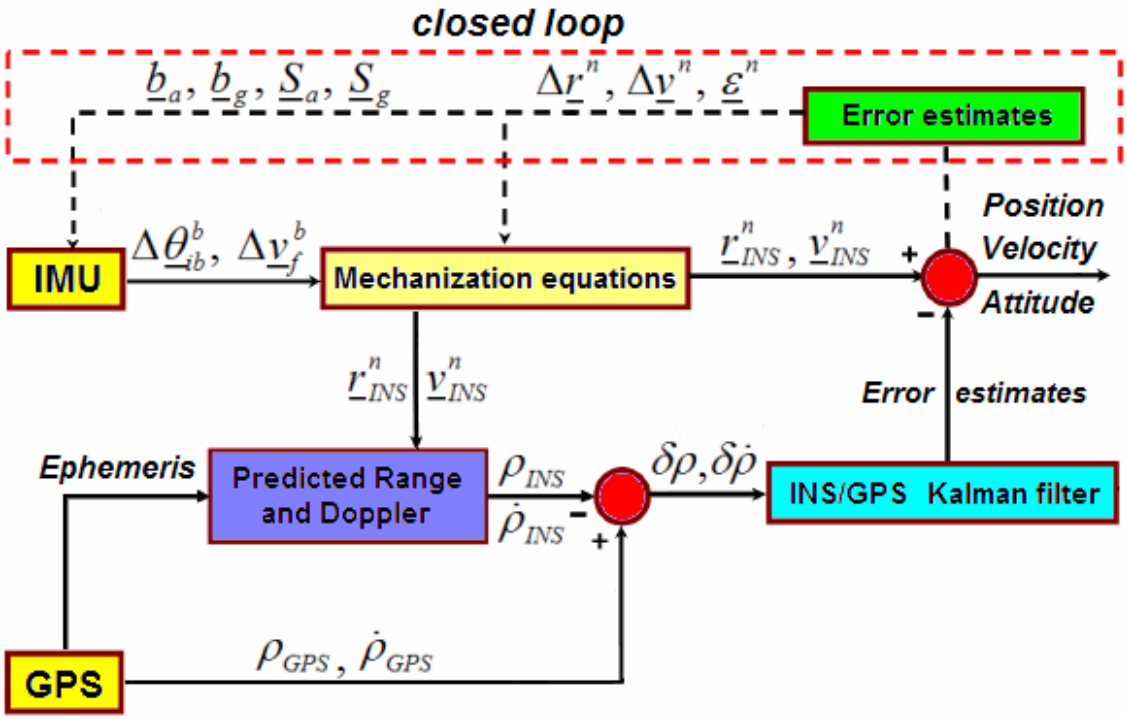

Fig. 5.6 Tightly coupled integration scheme (adopted from [14])

The tightly coupled integration uses raw measurements of GPS and INS-derived estimates of pseudorange and Doppler (determined using satellite ephemeris data), which are compared and used as inputs of an integrated single Kalman filter; in this scheme, the GPS filter is no longer necessary. The integrated Kalman filter (or INS/GPS filter) includes the equations for determining the navigation errors (position, velocity, and attitude), as well as those for the sensor errors, for both the INS and GPS systems.

The design of the INS/GPS Kalman filter is presented in the following subsections.

5.3.1 INS/GPS filter

The INS/GPS filter used in the tightly coupled integration is an extended Kalman filter which operates as a combination of the GPS and INS filter used in the loosely coupled approach.

5.3.1.1 System model

The system model must account for all of the GPS and INS states to be modeled. The two filters presented in the previous sections contain both positions and velocities in the state vector (more exactly, in the INS filter they are position and velocity errors). This permits to have an INS/GPS filter which corresponds to the 27-state INS filter augmented with the two state variables of the GPS receiver clock model. Thus, the state vector is

$$\underline{x} = \begin{bmatrix} \delta \underline{r}^n & \delta \underline{v}^n & \underline{\varepsilon}^n & \delta \underline{b}_a & \delta \underline{b}_g & \underline{b}_{tob,a} & \underline{b}_{tob,g} & \underline{S}_a & \underline{S}_g & t & \delta t \end{bmatrix}^T \qquad (5\text{-}35)$$

and has 29 components.

5.3.1.2 Measurement model

The tightly coupled approach is similar to the loosely coupled in terms of system model; they differ mostly in terms of measurement models. Instead of positions and velocities, pseudoranges and Doppler measurements (calculated by the INS and physically measured by the GPS receiver) are fed to the filter as observables. Therefore, the measurement model is similar to the one used in the GPS filter, with the main difference that now the measurements are differences of pseudoranges and Doppler:

$$\underline{z} = \begin{bmatrix} \underline{\rho}_{INS} - \underline{\rho}_{GPS} \\ \underline{\dot{\rho}}_{INS} - \underline{\dot{\rho}}_{GPS} \end{bmatrix} \qquad (5\text{-}36)$$

$$H = \begin{bmatrix} H_{rr} & 0_{nx3} & 0_{nx3} & 0_{nx3} & 0_{nx3} & 0_{nx3} & 0_{nx3} & 0_{nx3} & 0_{nx3} & c_{nx1} & 0_{nx1} \\ H_{vr} & H_{vv} & 0_{nx3} & 0_{nx3} & 0_{nx3} & 0_{nx3} & 0_{nx3} & 0_{nx3} & 0_{nx3} & 0_{nx1} & c_{nx1} \end{bmatrix} \quad (5\text{-}37)$$

where the matrices H_{rr}, H_{vr}, and H_{vv} have the same structure previously shown in section 5.2.1.3, with the only difference being the linearization point. In fact, the nominal trajectory for linearization is now obtained from the INS mechanization computed position and velocity solutions, rather than the predicted estimates.

5.4 Comparison of the two integration schemes

In this final section the main benefits and limitations of the two integration approaches previously described are discussed.

5.4.1 General aspects

The main advantages of the loosely coupled integration are:

- the dimensions of the state vectors (in both filters) are smaller than in the tightly coupled case, which translates into faster processing time (see section 5.4.2);
- the implementation of this scheme is very simple, that is, it doesn't require to change the existing hardware of the systems (INS and GPS) in order to be implemented.

On the other hand, there are also some significant limitations and shortcomings:

- the GPS receiver needs at least four satellite signals to compute the navigation solution. Under severe conditions, such as in (urban) canyons, GPS receivers can experience regular satellite outages; as a result, the integrated system might show poor accuracy, depending

mostly on the quality of the IMU (which assumes a major role in such specific situations).

- Process noise is added to two Kalman filters; this reduces the overall filtering capabilities of the system.

The tightly coupled integration is an alternative method that overcomes the main limitations of the loosely coupled approach. This second strategy offers several advantages:

- it gives an integrated navigation solution even if the number of GPS satellite signals drops below four;
- a single filter provides a statistically rigorous sharing of information among states (to the extent that the input statistics are correct);
- GPS data from individual satellites are used for the measurement update, so poor measurements can be detected and rejected, making the filter more robust;
- process noise is added to a single filter, thus improving the overall filtering capabilities of the system;
- having to program a single Kalman filter can simplify software development and debugging.

The tightly coupled integration is clearly more reliable in case of GPS data gaps, since it permits the use of as few as one GPS measurement in the estimation algorithm. Nevertheless, this strategy has some problems as well:

- it requires the access to the hardware, making this approach not available to the general user community [11];
- the larger size of the state vector requires more computational time, as illustrated in the following subsection.

5.4.2 Comparison of computational loads

In order to compare the computational loads of the various filters previously described, the matrix operations used in the Kalman filter algorithm (see section 4.2) have been evaluated. Tab. 5.3 gives a summary of this analysis for each iteration.

Tab. 5.3 Number of operations of the Kalman filter algorithm

Operation	#	Multiplications	Additions
nn x n1	*1*	n^2	$(n-1)n$
nn x nn	*3*	n^3	$(n-1)n^2$
nn + nn	*2*	*0*	n^2
n1 + n1	*1*	*0*	*n*
m1 + m1	*1*	*0*	*m*
mm + mm	*1*	*0*	m^2
nm x m1	*1*	*nm*	$(m-1)n$
nm x mm	*1*	nm^2	$(m-1)mn$
nm x mn	*1*	mn^2	$(m-1)n^2$
nn x nm	*1*	mn^2	$(n-1)nm$
mn x nm	*1*	nm^2	$(n-1)m^2$
mn x nn	*1*	mn^2	$(n-1)nm$
*inv(mm)**	*1*	$5/6m^3+m^2-5/6m$	$4/3m^3-3/2m^2+1/6m$

*using Gaussian elimination [34]

In the table, *nn* means a *n x n* matrix, and *n1* means a *n*-dimensional vector; *n* is the size of the state vector $\underline{x}$, while *m* is the size of the measurement vector $\underline{z}$. The second column represents the multiples of operations used in the Kalman filter algorithm. Note that these results can also be applied to the EKF algorithm as well, but, in this case, the computational load does not include the evaluation of the Jacobian matrices F_k and H_k (see section 4.3).

The results for the different filters are illustrated in Tab. 5.4, where the total number of operations is the sum of all multiplications and additions performed by a particular filter during a single step of the (extended) Kalman filter algorithm. The results are given for an increasing number of satellite signals processed by the GPS receiver.

Tab. 5.4 Total number of operations for different filters

Total number of operations				
# sat.	Loosely coupled			Tightly coupled
	GPS		INS	INS/GPS
	PV	PVA		
1	-	-	-	*151440*
2	-	-	-	*156819*
3	-	-	-	*162455*
4	*5212*	*11671*	*148493*	*168361*
5	*6004*	*12910*	*148493*	*174550*
6	*6924*	*14301*	*148493*	*181035*
7	*7985*	*15857*	*148493*	*187829*
8	*9200*	*17591*	*148493*	*194945*
9	*10582*	*19516*	*148493*	*202396*

For a better visualization, the same results have also been plotted in Fig. 5.7 and 5.8.

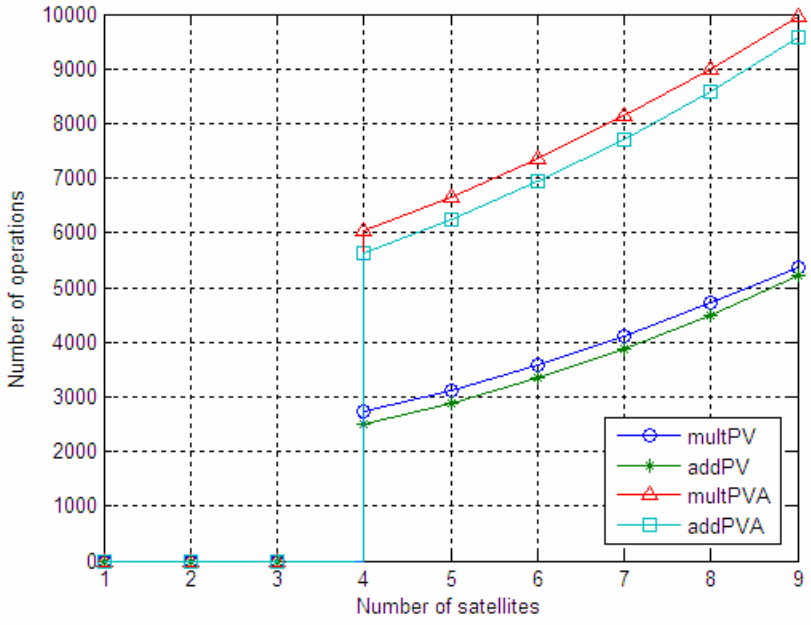

Fig. 5.7 Number of operations of PV and PVA filters

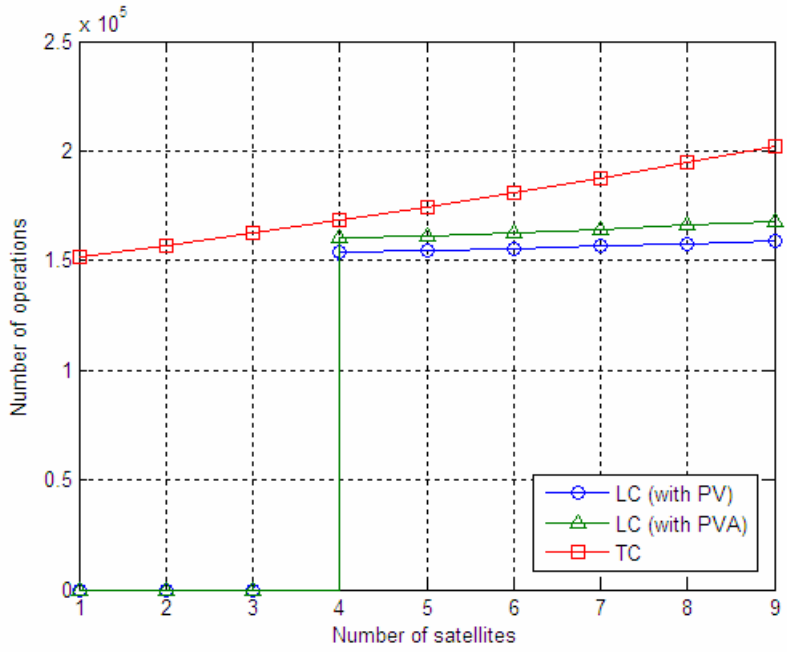

Fig. 5.8 Number of operations for LC and TC integrations

As normal, an increased number of GPS signals being processed corresponds to a higher computational load. With less than 4 satellites available, the LC approach cannot compute a solution; therefore the Kalman filter algorithm is not performed in those situations.

The computational load required for the PVA filter is approximately twice as the one required for the PV filter. However, when we consider the GPS filter as part of the LC scheme, such difference becomes less significant since the number of operations performed by the INS filter has a superior influence. The increment using the LC integration with a PVA filter instead of a PV ranges between 4.2-5.6%, depending on the number of satellites.

Concerning the comparison between the LC and TC integrations, in this case the differences in computational loads are more significant: the increment varies between 5.1-20.5% when considering the LC-PVA scheme, while for the LC-PV it is 9.5-27.5%.

The main conclusion that can be drawn from this analysis is that the difference in computational loads is mainly a function of the system dimensions, thus explaining why the TC approach requires a higher computational time. In addition, the more satellites are available, the greater will be the difference between the two approaches.

Chapter 6

Software and Implementation Considerations

This chapter gives some information about the software developed in order to run various tests and simulations of the integrated INS/GPS system. The program was created in MATLAB and consists of a number of modules (*m-files*) which will be briefly described in the following sections.

6.1 Main.m

The main file is simply a routine that calls, in the proper order, all those functions that have been created to perform the desired simulations. The basic steps are:

1. upload of constant variables (IMU and GPS characteristics, Earth's geometric parameters, time settings, etc.);
2. upload of trajectory data, i.e. the vehicle's reference position, velocity, and attitude during the entire simulation (the INS/GPS algorithm is executed in a post-mission mode);
3. upload of initial conditions (for the INS mechanization and for the various Kalman filters);
4. memory pre-allocation for vectors and matrices (this part is essential since it reduces considerably the computational time);
5. definition of GPS satellite visibility: here it is possible to manually set the number of visible satellites in any period of time according to the type of situation that the user wishes to reproduce;
6. *for* cycle consisting of several operations: INS measurements (corrupted by all the error sources described in section 3.5), INS mechanization,

GPS measurements (also affected by errors), GDOP evaluation, PV or PVA filter (only for the loosely coupled mode), EKF algorithm;

7. graphs plotting.

The time length of one step of the *for* cycle depends on the IMU's working frequency; however, GDOP evaluation is done only periodically (for example, every 30 *s*) while GPS measurements, as well as the EKF algorithm, depend on the measurement update frequency of the GPS receiver, which has been set equal to 10 *Hz* for all simulations, since this is a typical value encountered for low-cost GPS receivers.

6.2 Trajectory.m

In order to assess the performance of the integrated navigation system, a reference trajectory is needed. The goal of this function is to generate a reference trajectory to obtain the data about the vehicle's position. It performs the integration of the general motion equations using an explicit Runge-Kutta (4,5) formula. The vehicle's velocity and attitude must be assigned in advance. Besides position information, this function also returns the accelerations and the rates of turn in the *b*-frame, which are used to represent the uncorrupted IMU's output.

6.3 GPS.m

This module was created to make available the GPS satellite orbit coordinates during a desired period of time. An approximated satellite position in ECEF coordinates is given as [17]

$$r_x^e = R\left(\cos\theta\cos\Omega - \sin\theta\sin\Omega\cos i\right) \tag{6-1}$$

$$r_y^e = R\left(\cos\theta\cos\Omega + \sin\theta\sin\Omega\cos i\right) \tag{6-2}$$

$$r_z^e = R\sin\theta\sin i \tag{6-3}$$

where

$$\theta = \theta_0 + (t - t_0)\frac{360}{43.082} \ \text{deg} \tag{6-4}$$

$$\Omega = \Omega_0 - (t - t_0)\frac{360}{86.164} \ \text{deg} \tag{6-5}$$

$$R = 26559.800 \ \text{km} \tag{6-6}$$

$$i \approx 55^{\text{o}} \tag{6-7}$$

The above equations result from simplifying the expressions for the satellite position given in Tab. A.2 (see Appendix A).

The parameter Ω is the right ascension of ascending node, that is, the ECI longitude where the orbital plane intersects the equatorial plane as the satellite crosses from the southern hemisphere to the northern hemisphere. The orbital plane is specified by Ω and i, the inclination of the orbit plane with respect to the equatorial plane. The θ parameter represents the location of the satellite within the orbit plane, and it is often referred to as mean anomaly; it is the angular phase in the circular orbit with respect to ascending node.

Tab. 6.1 gives the parameters Ω_0 and θ_0 for the GPS satellite constellation at the reference time t_0 (midnight July 1, 1993) [27].

Tab. 6.1 Ω_0 and θ_0 for the GPS constellation at reference time t_0

Satellite ID	Ω_0 (º)*	θ_0 (º)*	Satellite ID	Ω_0 (º)*	θ_0 (º)*
1	272.847	268.126	13	92.847	135.226
2	272.847	161.786	14	92.847	265.446
3	272.847	11.676	15	92.847	35.156
4	272.847	41.806	16	92.847	167.356
5	332.847	80.956	17	152.847	197.046
6	332.847	173.336	18	152.847	302.596
7	332.847	309.976	19	152.847	333.686
8	332.847	204.376	20	152.847	66.066
9	32.847	111.876	21	212.847	238.886
10	32.847	11.796	22	212.847	345.226
11	32.847	339.666	23	212.847	105.206
12	32.847	241.556	24	212.847	135.346

*Ω_0 and θ_0 are values at reference time t_0 (midnight July 1, 1993)

The baseline of the 24-satellite GPS constellation at the reference time t_0 is shown in Fig. 6.1, where the position of each satellite is expressed in terms of the orbital parameters Ω and θ; in such way, the six orbital planes, each containing four satellites, are clearly visible.

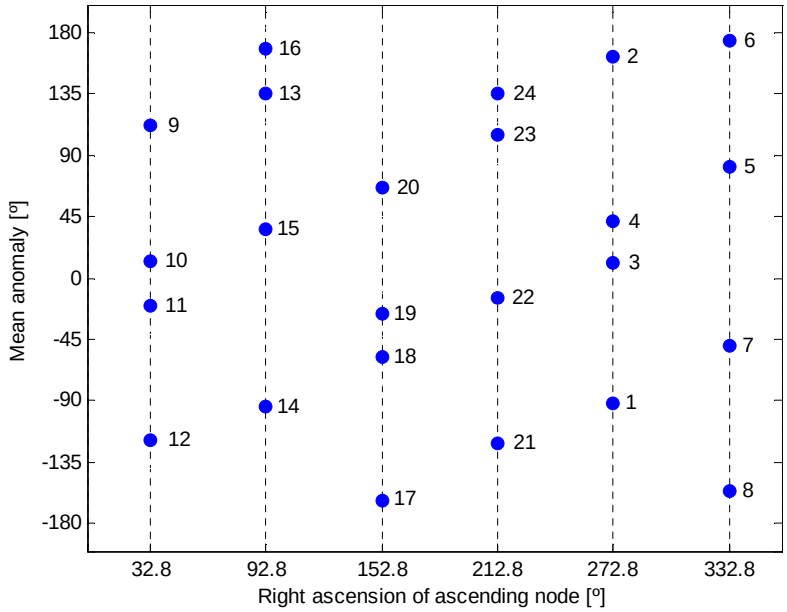

Fig. 6.1 GPS satellite constellation planar projection

6.4 Galileo.m

The function *Galileo.m* is similar to *GPS.m* in a way that it gives the satellite orbit coordinates for Galileo's constellation. The equations for the satellite position are the same presented in the previous section, with the only difference being the values of the orbit parameters. A brief description of the Galileo system and its satellite constellation is given in Appendix D.

The reason why this satellite constellation has been represented is to assess the performance of the integrated system when the number of available satellites is greatly increased. This analysis is presented in section 7.5.

6.5 GDOP.m

The GDOP evaluation is the criteria that has been used for the choice of satellites. In this routine all the possible combinations up to 9 satellites are considered in order to choose the best satellite geometry which will give the highest accuracy for the GPS solution. This function is executed periodically, based on a pre-defined time interval.

6.6 PV.m, PVA.m

These functions implement the PV and PVA filters for the loosely coupled integration. They perform all the calculations described in section 5.2.1, giving as output the estimates of the vehicle's position in the *n*-frame. Since the satellite position is known in ECEF coordinates, it is necessary to operate the coordinate transformation described in section 3.1.5 in order to obtain a solution in the navigation frame. These routines are executed based on the measurement update frequency of the GPS receiver (10 *Hz*).

6.7 EKF.m

This function implements the EKF algorithm. There are two different versions of this file, due to the reason that one applies to the LC integration and the other one to the TC integration. In both cases, a closed-loop scheme is utilized (see Fig. 5.1 and 5.6).

Chapter 7

Tests and Results

This chapter describes the tests and analysis results for the methods described in the previous chapters. The performance evaluation is carried out in a post-mission processing mode. Several types of performance analysis are considered: first, individual navigation systems are tested (INS and GPS); then the various integration strategies are studied and compared. For each case, two datasets representing different scenarios are available. The results are mainly discussed in terms of position, velocity, and attitude errors which are computed using the reference trajectories.

7.1 Datasets

Two datasets have been used to assess the performance of the navigation systems. The simulation time is 10 minutes for both cases, which differ only in terms of trajectory path and vehicle's maneuvering.

The first dataset represents a low dynamics trajectory (Fig. 7.1-a): the vehicle's motion determines a closed-loop path with slow and small variations of altitude. The maximum vertical speed is 4 *m/s*, while the maximum horizontal speed is approximately 55 *m/s*. Although the motion is not uniform, it is not characterized by significant accelerations and turn rates.

In the second dataset, the vehicle performs aggressive maneuvers: frequent turns at high velocity determine a more complex path, as illustrated in Fig. 7.1-b. The trajectory can be divided into three parts: an initial ascending spiral, with the vehicle accelerating upward and increasing the radius of curvature at the same time; the second part consists of a sequence of horizontal loops with a variable descending velocity; finally, a second ascending spiral is performed, but this time with the vehicle decelerating upward and decreasing the radius of curvature. In such scenario, the vehicle experiences considerable and

continuous accelerations and turn rates throughout the entire simulation. The maximum vertical speed is 6 *m/s*, and the maximum horizontal speed is approximately 100 *m/s*.

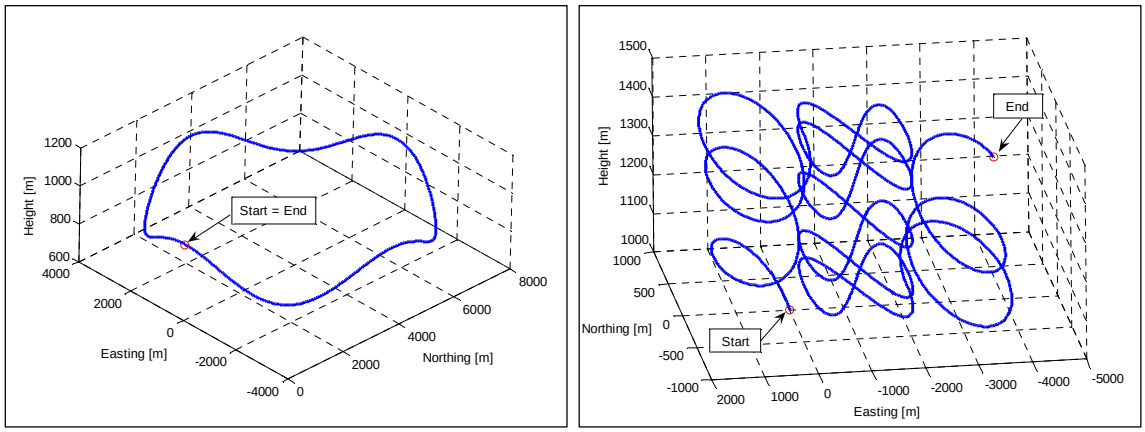

(a) Low dynamics **(b) High dynamics**

Fig. 7.1 Reference trajectories of simulated datasets

7.2 INS-only solution

The performance of the low-cost MEMS-IMU described in section 5.2.2.1 has been compared with other IMUs of different quality (i.e. accuracy level); the various existing categories have been outlined in section 3.7.4. Specifically, the following analysis includes the performance of a medium grade MEMS-IMU and a tactical grade FOG-IMU (Fiber-Optic-Gyro IMU). The characteristics of these sensors are taken from [35] and are here summarized in Tab. 7.1. Although the author does not mention the model and brand of the individual IMUs, the following characteristics are useful for a general comparison between the low-cost MEMS-IMU analyzed in this thesis with others of higher quality.

As previously mentioned, the quality of an IMU is often evaluated by the quality of the gyros contained in the sensor system. As can be noted from Tab. 7.1, the MEMS-IMU has an in-run bias significantly smaller than the one of the low-cost Crista IMU (see Tab. 5.2); such biases are completely negligible for higher grade IMUs. Given this great amount and intensity of errors in low-cost MEMS inertial sensors, traditional approaches for integrating INS and GPS are likely to fail, and some non-traditional algorithms and approaches are required.

Tab. 7.1 Characteristics of the MEMS-IMU and FOG-IMU

	MEMS-IMU	FOG-IMU
Accelerometers		
Turn-on bias	*0.049 m/s^2*	*0.049 m/s^2*
Bias drift*	*0.0098 m/s^2*	-
	3600 s	-
Scale factor error	*5000 ppm*	*200 ppm*
Random noise	*0.4 mg/√Hz*	*0.05 mg/√Hz*
Gyros		
Turn-on bias	*75 º/h*	*5 º/h*
Bias drift*	*3 º/h*	-
	3600 s	-
Scale factor error	5000 ppm	100 ppm
Random noise	18 º/h/√Hz	6 º/h/√Hz
Update rate	100 Hz	200 Hz

* Parameters of first-order Gauss Markov processes

Before testing the performance of the various IMUs, it is important to verify the correct operation of the INS mechanization algorithm described in section 3.3. Under ideal conditions, that is, with all sensors unaffected by error sources, the INS algorithm, run in post-processing mode, should reproduce precisely the reference trajectory. The results obtained with this ideal test, in terms of position, velocity, and attitude errors, are shown in the following figures.

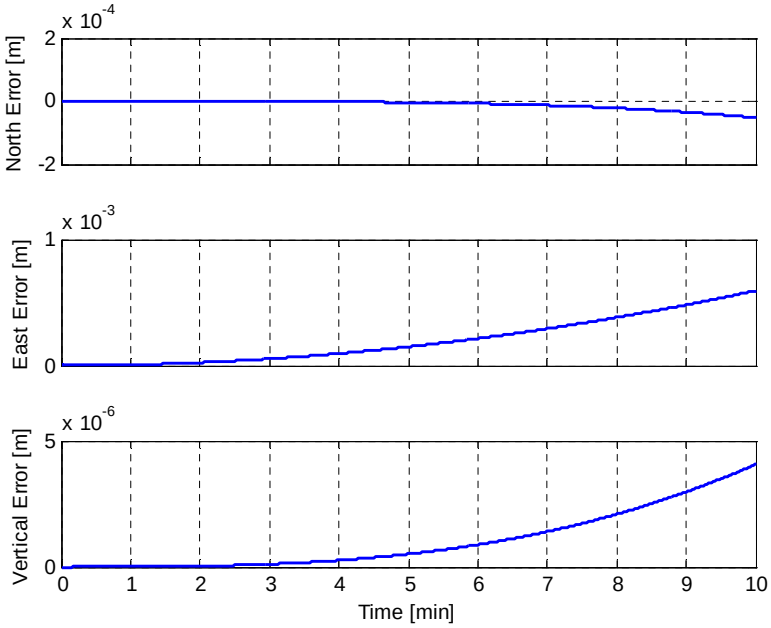

Fig. 7.2 Ideal results for INS position errors

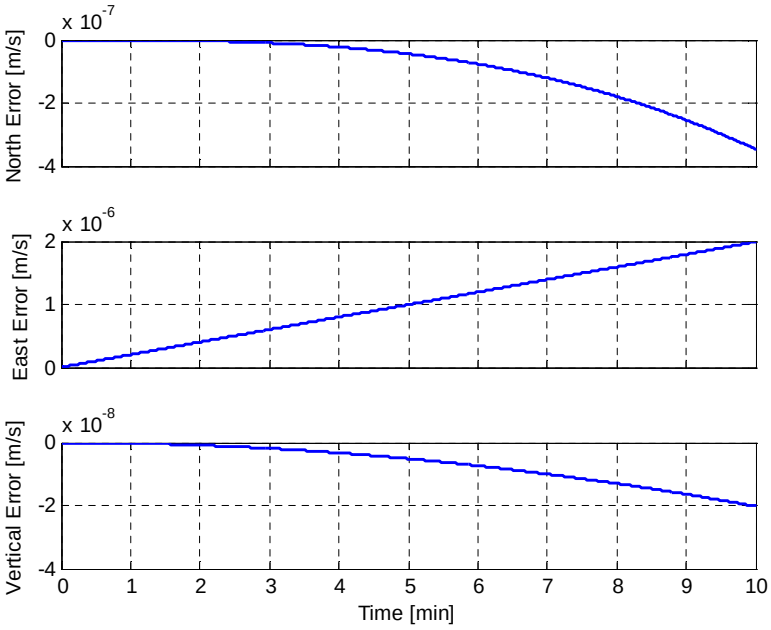

Fig. 7.3 Ideal results for INS velocity errors

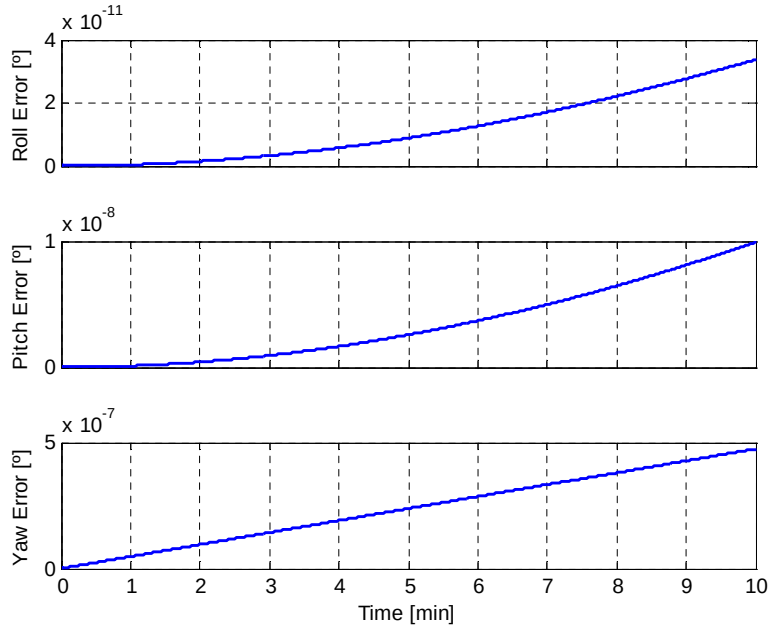

Fig. 7.4 Ideal results for INS attitude errors

For all cases, the errors are significantly small, proving that the INS mechanization algorithm works properly. With 10 minute simulations, the maximum position error is 0.5 *mm*, the maximum velocity error is 0.002 *mm/s*, and the maximum attitude error is 5 x 10^{-7} degrees. The fact that these errors grow slowly with time, even if we considered ideal sensors, depends on some

problems which are typical of strapdown inertial systems. The most important is known as sculling error. If the specific force vector were measured, transformed to navigation coordinates continuously, and integrated to obtain velocity, no error would occur. However, the accelerometers integrate acceleration in the body frame at discrete time intervals. The presence of combined rotation and acceleration, a phenomenon known as “sculling”, can lead to errors referred to as sculling errors. If these errors are not compensated, an average acceleration is erroneously computed [20]. In the algorithm implemented in this work, a first-order sculling correction has been applied: it consists in the computation of the cross-product between the gyro data and the accelerometer data to reduce the effect of these errors. Its implementation is visible in Eq. (3-36). Other typical strapdown problems, known as coning errors and size-effect errors, are not relevant in these simulations since they depend on the real motion of the gyros input axis and on the accelerometers locations, respectively [20].

After having verified the proper operation of the INS mechanization algorithm, it is now possible to assess the performance of the various IMUs. The first test is done using the INS in stand-alone mode, that is, without any sort of external aid and without using any calibration information; Fig. 7.5 shows the processing results.

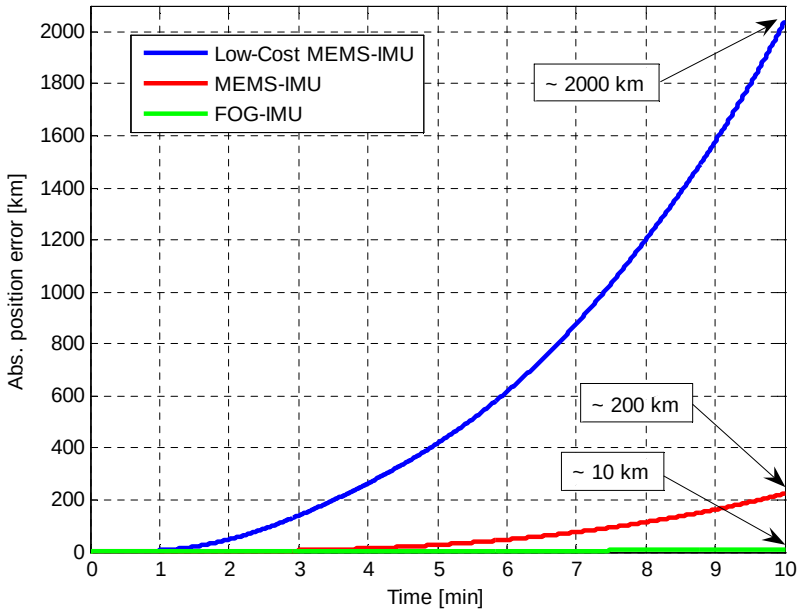

Fig. 7.5 Positional error for different IMUs (without initial calibration)

Without any external aid, the positional error grows exponentially due to the integration step in the INS mechanization algorithm, which amplifies the effects of the IMU's errors along time. In Fig. 7.5, the maximum error reached by each IMU after a 10 minutes simulation is marked. The results clearly show the consequences of the different quality of these sensors: the FOG-IMU reaches a maximum error of 10 *km*, in conformity with the accuracy level indicated in Tab. 3.4; the MEMS-IMU reaches a value which is approximately 20 times greater, while for the low-cost MEMS-IMU it is 200 times greater.

Upon the evidence of these results, we shall expect a quick error growth for the lower grade IMUs even when an initial calibration procedure is performed; in fact the in-run variations of bias (and scale factor) are significant even on a short time scale, as visible from Fig. 7.6. An initial calibration simply delays the effects of the error propagation; however, the absolute position error still becomes unacceptable after a very short period of time for all of the sensors tested. Note that, in a simulation context, the initial calibration consists of assuming as known the values of the turn-on biases for both accelerometers and gyroscopes.

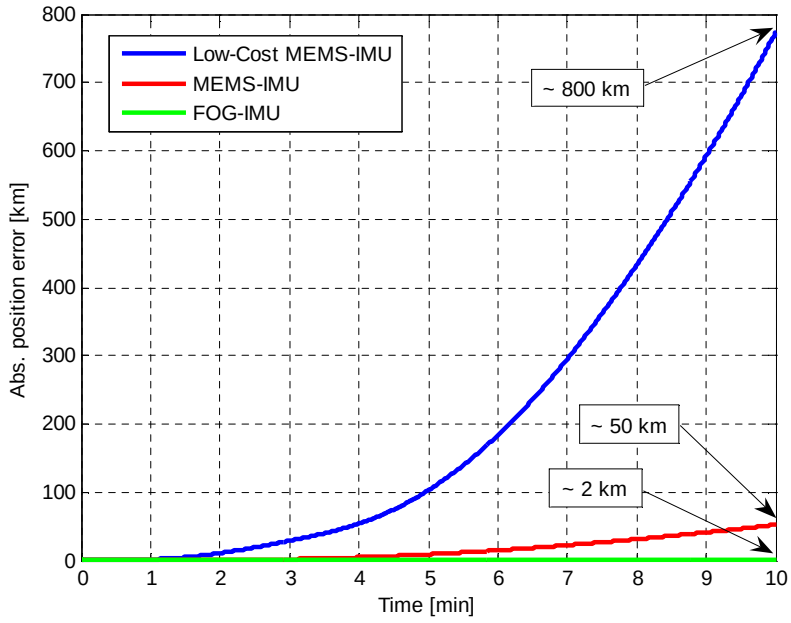

Fig. 7.6 Positional error for different IMUs (with initial calibration)

Finally, it is important to note that in the previous simulations the vehicle's initial position and orientation are supposed known with no error; in a real situation this information cannot be so accurate causing the INS performance to degrade with even higher rapidity.

7.3 GPS-only solution

In this section the performance of the GPS solution is investigated in order to assess the GPS data quality. This is an important part since the GPS is the aiding source of the integrated navigation system. A further objective is to compare the accuracy obtained using a PV or a PVA filter (both described in section 5.2.1). To accomplish these goals, two simulations have been run: one with the low dynamics trajectory, and the other with the high dynamics one; the GPS receiver sampling frequency is 10 *Hz*. The maximum number of satellites is 9, and the minimum is 5, with an average of 8; this implies a 100% satellite availability during the entire simulation. Fig. 7.7 shows the satellite dilution of precision and the number of available satellites during the test run.

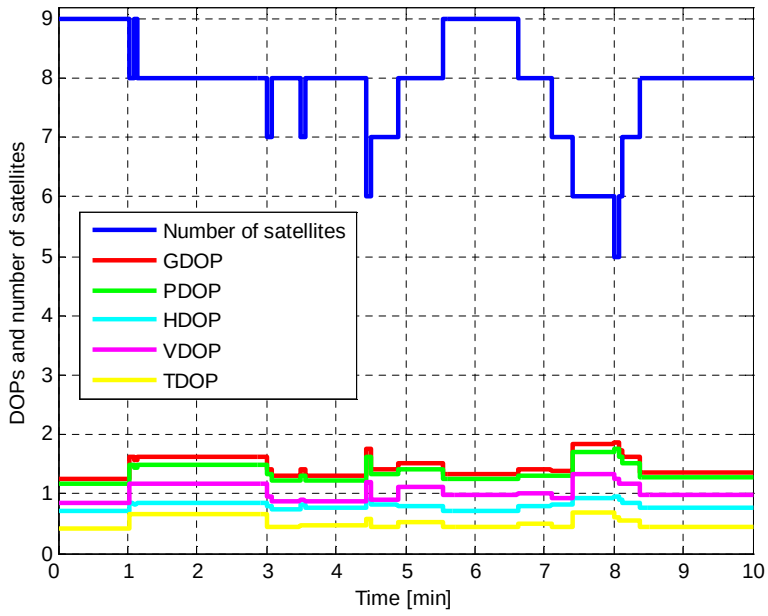

Fig. 7.7 Dilution of precision and availability during the simulation test

It is possible to verify that the DOPs are correlated with satellite availability, as expected. For example, after 4.4 minutes, a decreased satellites number from 8 to 6 caused DOP values to increase almost 50%. This consequently will affect the position and velocity accuracies. However, HDOP and VDOP values lower than two are still good enough to guarantee a good satellite geometry.

Another important observation is that the VDOP, related to the accuracy along the vertical direction, is larger (i.e. worse) than the HDOP, which corresponds to the accuracy in the local horizontal plane (East-North). It is possible to define two more DOP parameters associated with the accuracy in the East and North direction independently; in accordance with the notation used in section 2.5 we have:

$$EDOP = \sqrt{V_{11}} \tag{7-1}$$

$$NDOP = \sqrt{V_{22}} \tag{7-2}$$

where the GDOP matrix V was introduced in Eq. (2-32). The values assumed by these parameters during the simulation test are shown in Fig. 7.8.

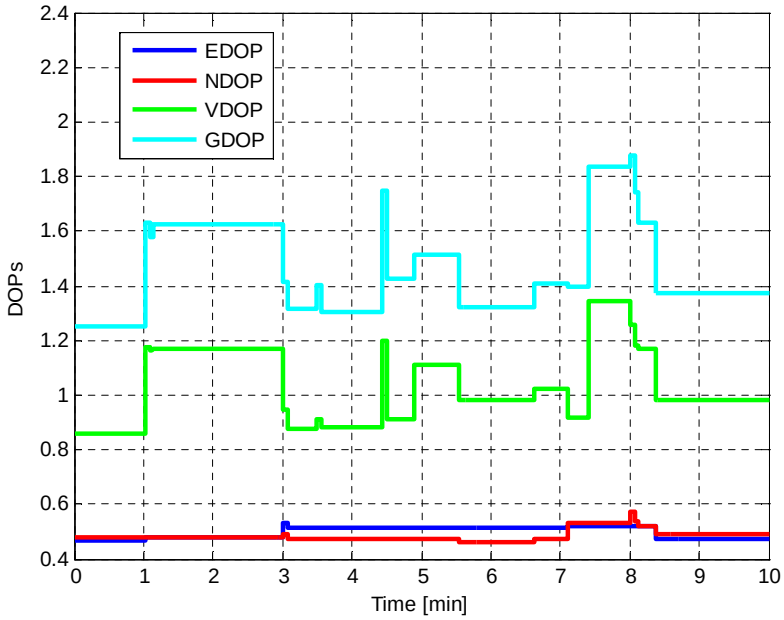

Fig. 7.8 Various DOPs during the simulation test

The EDOP and NDOP range around 0.5 for the majority of time; the VDOP assumes values which are approximately twice as large as the other two parameters. It is clearly visible that the major contribution to the value of the GDOP parameter, which is the one utilized to choose the best satellite geometry, is given by the VDOP (since the TDOP is characterized by small values as well). The main consequence of these results will be a less accurate information about the vehicle's altitude, compared to the information about relative northing and easting, determined by the GPS receiver.

The effects of higher DOP values in the vertical direction are immediately visible from the plots of the position and velocity error variations versus time (Fig. 7.9 and 7.10, respectively), obtained using the PV filter and the first dataset.

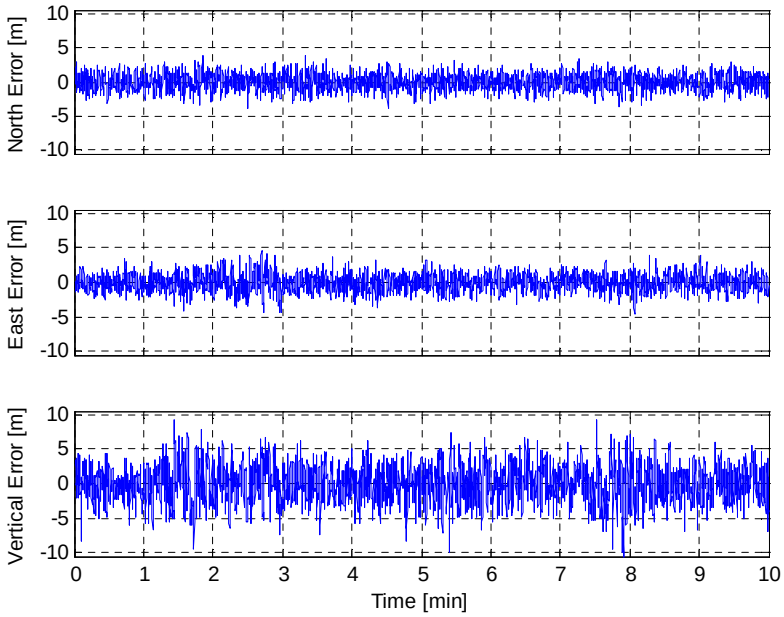

Fig. 7.9 Position error versus time (first dataset)

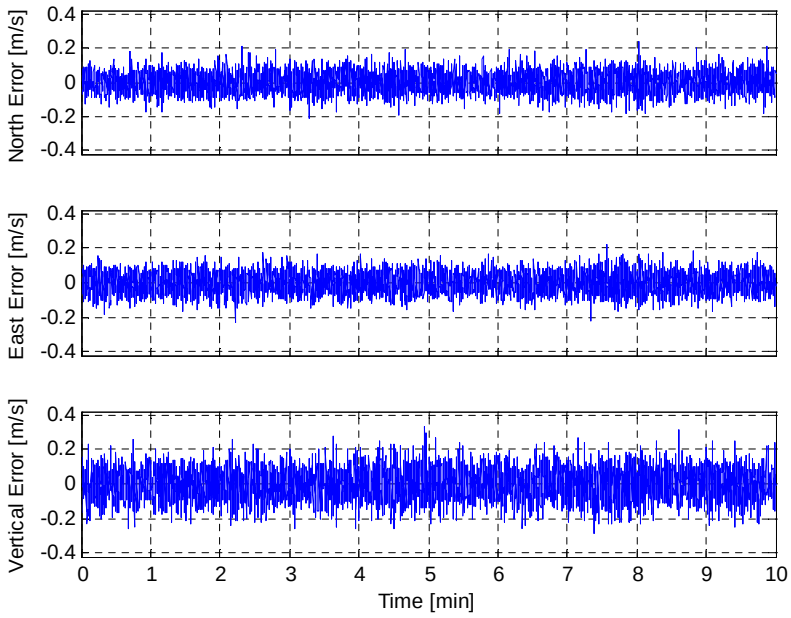

Fig. 7.10 Velocity error versus time (first dataset)

By examining these graphs, it is evident that both position and velocity in the vertical direction are less accurate than the corresponding quantities in the horizontal plane. The maximum horizontal position error is 4.67 *m* and the maximum horizontal velocity error is 0.238 *m/s*, while for the vertical direction the maximum position error is 10.53 *m* and the maximum velocity error is 0.332 *m/s*.

The influence of a variable number of available satellites is not so clear from the visualization of these error plots, since the satellite geometry is good during the entire simulation. However, in the interval between 7 and 8 minutes, where the number of satellites drops to the lowest values, a higher spreading of the error is somehow visible, mainly for the vertical position error.

In order to assess the different performance of the PV and PVA filters, several simulations have been run considering both datasets; the results are summarized in Tab. 7.2. In the table, LD and HD refer to low dynamics and high dynamics, respectively. With the first dataset, the results obtained with the two filters do not show significant differences; in this case, the PVA filter offers a better accuracy in the order of only a few centimeters. The importance of using a PVA filter becomes evident when considering high dynamics: with the second dataset, in fact, the performance of the PV filter deteriorated considerably, showing RMS errors which are 3 to 4 times larger than in the previous situation.

As for the PVA filter, its performance is also poorer, but the decrease in accuracy is smaller.

Tab. 7.2 Mean and RMS values of position errors of various simulations

	PV		PVA	
	LD	**HD**	**LD**	**HD**
Mean (m)				
North	*-0.00*	*0.05*	*-0.00*	*0.02*
East	*-0.01*	*0.03*	*0.01*	*0.02*
Up	*-0.08*	*-0.14*	*-0.05*	*-0.08*
RMS (m)				
North	*1.06*	*3.99*	*1.05*	*1.55*
East	*1.16*	*3.29*	*1.14*	*1.31*
Up	*2.49*	*5.61*	*2.43*	*2.71*
2D	*1.57*	*5.17*	*1.55*	*2.03*
3D	*2.94*	*7.63*	*2.88*	*3.39*

A further consideration about these last results addresses to the accuracy obtained in the vertical direction and in the local horizontal plane (2D solution). Regardless of the type of filter or dataset used, the vertical error is always higher than the 2D error. Once again, we can see the correspondence between the positional errors and the values obtained for the DOP parameters for these simulations, in which the VDOP is all the time greater than the HDOP.

The comparison of computational loads of the PV and PVA filters, given in section 5.4.2, showed that the former requires a number of operations that is approximately a half of those required by the latter. However, when these filters are considered as part of an integrated INS/GPS system, we saw that this difference becomes less relevant. For such reason, and for the results obtained in this section, the PVA filter will be employed in all the following simulations. Because of its consistent accuracy, it can be used for position and velocity updates in the INS/GPS system.

7.4 INS/GPS solution

This section presents the results obtained with the integrated system, which are of most interest according to the objectives of this thesis. Many types of simulations and comparisons will be illustrated, with principal focus on the

performance of the low-cost MEMS-IMU in both the loosely and tightly coupled configurations.

7.4.1 Results with full GPS data availability

The first analysis deals with a situation of full GPS data availability during the entire simulation. The satellite dilution of precision is the one previously illustrated in Fig. 7.7. Firstly, the results obtained with the integration of GPS with the low-cost MEMS-IMU are presented. The two strategies adopted are those described in Chapter 5, namely, the loosely coupled and the tightly coupled integrations. Same considerations apply to the types of filters: it will be seen, in fact, that for better quality IMUs the filters dimensions are smaller (i.e. the state vector to be estimated contains a smaller number of states).

Since the accuracy of the integrated system depends on the accuracy of the GPS solution (at least in the situation of complete data availability), a similar level of accuracy can be expected from the integrated solution as well. This is proved by Fig. 7.11 and 7.12, which present the position and velocity errors obtained with both integration strategies. Since the GPS satellite availability is good throughout the simulation, the INS navigation parameters are corrected continuously, preventing the errors from accumulating.

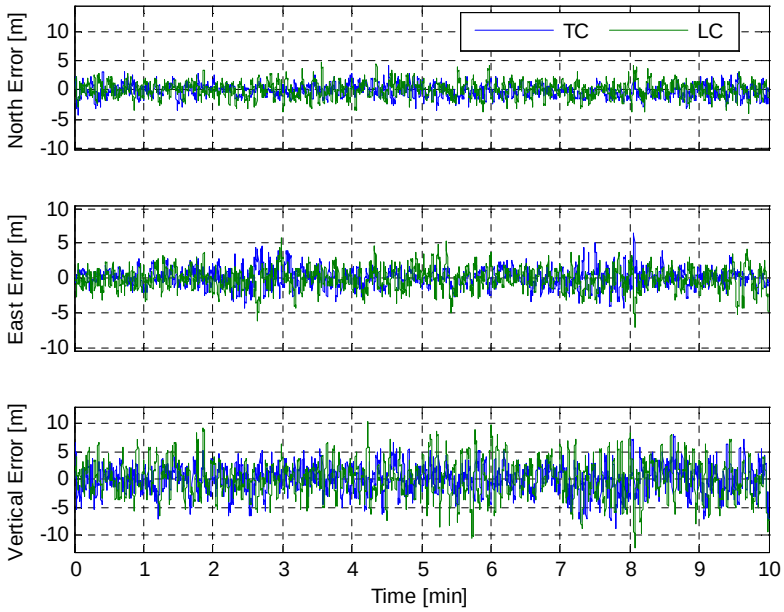

Fig. 7.11 Position errors for low-cost INS/GPS (no GPS outages)

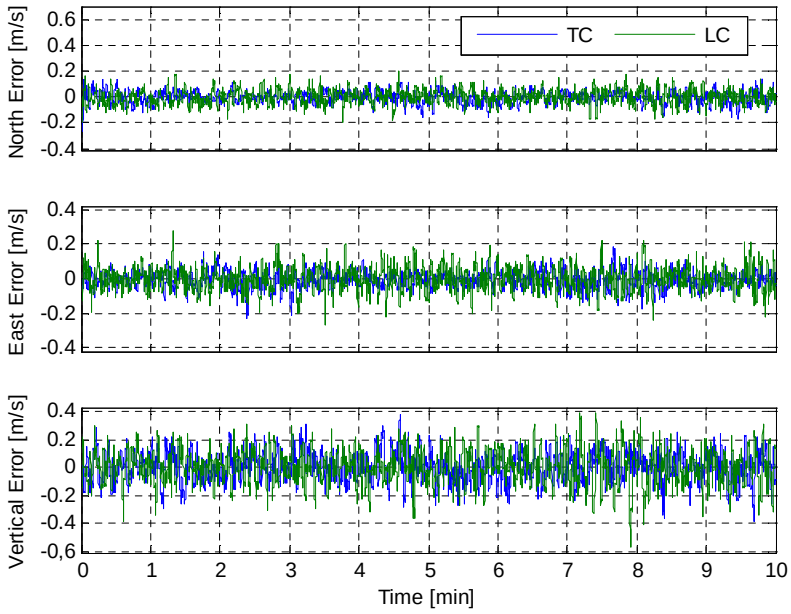

Fig. 7.12 Velocity errors for low-cost INS/GPS (no GPS outages)

The level of accuracy is the same obtained with the GPS-only solution. The TC and LC integrations do not show significantly different performances in a situation of full satellite availability. It is possible to observe that both position and velocity errors present a time lag. This is due to the problem in the choice of the INS filter covariance matrix Q_k, which was discussed in section 5.2.2.2. The values of the elements of Q_k have been manually increased in order to stabilize the filter; however, while the filter becomes more stable, the resulting estimates turn out to be noisier due to the free passage of the measurement noise. On the other hand, small values of Q_k can reduce the noise passage, but, at the same time, they cause the appearance of a time lag in the estimates. Thus, the final values that have been chosen for the elements of Q_k are based on a compromise to reduce as much as possible the effects of these two issues. The time lag problem is more evident for the estimates of the attitude errors, as shown in Fig. 7.13.

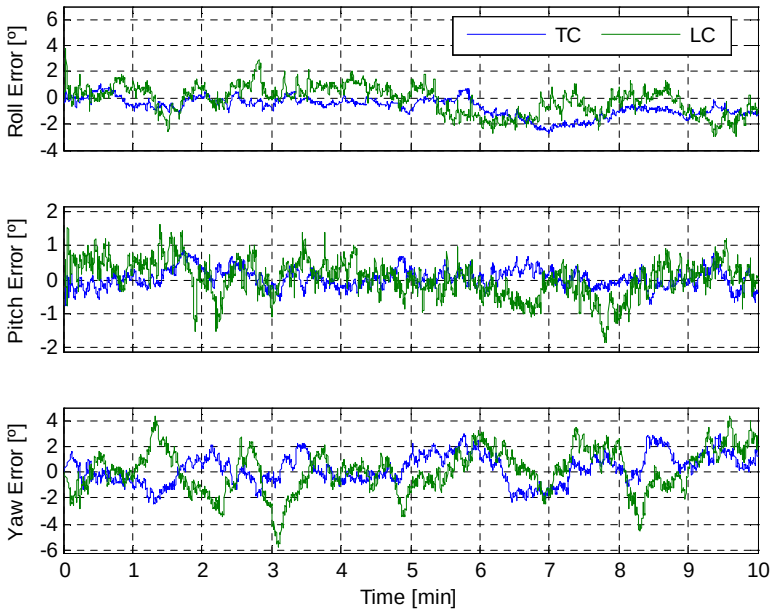

Fig. 7.13 Attitude errors for low-cost INS/GPS (no GPS outages)

The attitude errors seem to vary less rapidly than those obtained for position and velocity. The level of accuracy is approximately the same for all the three angles. However, it can be proved that this result is not general: the fact of having considered a trajectory with both vertical and horizontal accelerations permits to have all these errors observable. For example, without a horizontal acceleration, the yaw angle error becomes not observable and starts to increase. In order to demonstrate this problem, a simple trajectory of a vehicle traveling in a straight line at a constant velocity has been generated. While this new dataset did not cause any problem in the determination of position and velocity, it was useful for verifying the non-observability of the yaw angle, as shown in Fig. 7.14. The roll and pitch errors maintain the same level of accuracy already seen before, except for a very short initial period where the filter is still stabilizing. The yaw error, instead, grows rapidly and becomes very large after only 30 seconds. A possible solution to this problem is to utilize an external aiding source which is able to determine the yaw angle separately from the INS/GPS navigation system (for instance, a magnetic compass); such information can be subsequently used as an additional measurement available for the INS filter, turning the yaw angle error into an observable variable.

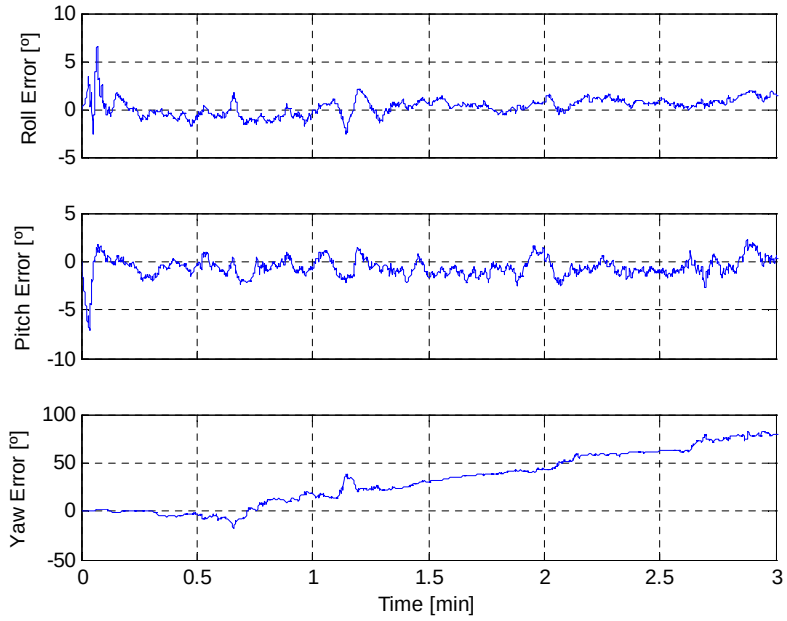

Fig. 7.14 Attitude errors obtained with a straight uniform trajectory

The last part of this section deals with the comparison of the performance obtained using different types of IMUs in the integration with GPS.

First, it is important to note that when considering sensors of better quality the size of the INS filter is reduced. In fact, a higher IMU's grade is directly associated with a fewer number of sensor errors, or with errors that are maintained constant during the operation. If in-run variations are absent or non-significant, it is possible to eliminate the dynamics of such errors from the INS system equations, thus decreasing the dimension of the system state vector. For example, the FOG-IMU, whose characteristics are illustrated in Tab. 7.1, is affected only by a turn-on bias and scale factor error, which have no time variations; in such case, the six equations related with the bias drift dynamics (for both accelerometers and gyros) can be eliminated from the INS filter, decreasing consequently the number of variables to estimate. This not only reduces the computational load required for the filter, but it also makes it more efficient since it facilitates the estimation of the various errors which now are fewer in number.

Therefore, modified reduced versions of the INS filter have been created to run simulations with other types of IMUs. The results proved that in a situation of good satellite availability the overall performance of the integrated system

depends almost exclusively on the accuracy of the GPS solution. Since we already saw that no significant differences are shown by the two integration strategies (for this specific situation), only one was used to run these tests, namely, the tightly coupled. The RMS position accuracy obtained in the various tests is illustrated in Fig. 7.15; these values are also listed in Tab. 7.3.

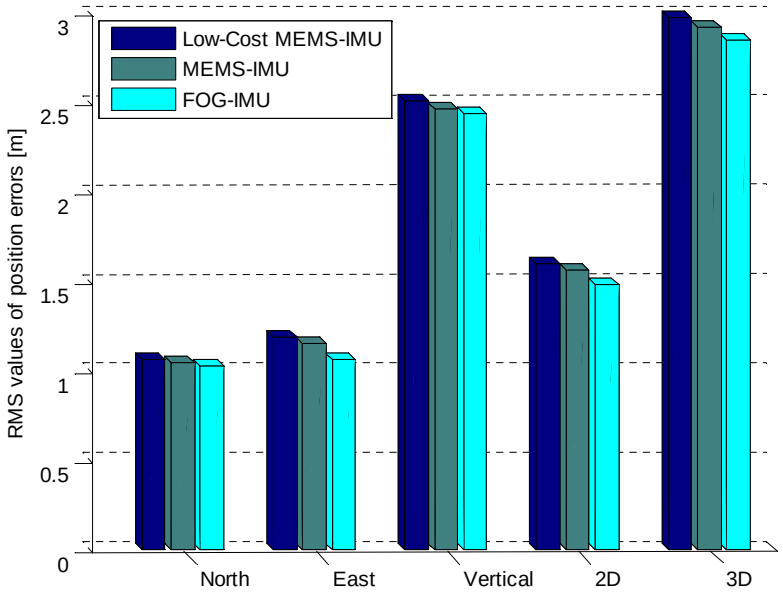

Fig. 7.15 Bar plot of RMS position errors for different IMUs

Tab. 7.3 RMS position errors for different IMUs

RMS (m)	Low-Cost MEMS-IMU	MEMS-IMU	FOG-IMU
North	*1.07*	*1.05*	*1.03*
East	*1.19*	*1.16*	*1.07*
Up	*2.51*	*2.47*	*2.44*
2D	*1.60*	*1.56*	*1.49*
3D	*2.98*	*2.92*	*2.86*

The performance of the integrated system hardly improves using higher quality IMUs. When GPS measurements are continuously available, it is the GPS accuracy that determines the overall navigation solution accuracy, since it is the GPS-only solution that is used as a reference to correct the results given by the inertial system. The importance of having better quality IMUs will be evident in the case of partial or total GPS outages, because it is in such situations that the system relies more (or exclusively) on the INS measurements.

Tab. 7.4 specifies the positioning accuracy requirements for all flight categories up to precision approach [8]. It is possible to see that the accuracy requirements for category I should be achieved most of the time by the integrated system being studied here; concerning the other two categories, the vertical accuracy is much more restrictive and this system, even under benign operational conditions, does not permit the fulfillment of such requirements.

Tab. 7.4 Positioning accuracy requirements for all flight categories

	Horizontal	Vertical
Category I	*17.1 m*	*4.1 m*
Category II	*5.2 m*	*1.7 m*
Category III	*4.1 m*	*0.6 m*

7.4.2 Results with simulated GPS outages

As previously mentioned, a major advantage of the tightly coupled INS/GPS system compared to a loosely coupled approach is the aiding capability in the case of fewer than four visible satellites.

In order to prove how GPS outages can easily occur in practical situations, a simulation of an helicopter flying through a canyon has been run, and the results are illustrated in the following subsection.

7.4.2.1 Simulation of a canyon flight

The scenario reproduced for this simulation is illustrated in Fig. 7.16. The objective is to evaluate the number of visible satellites as the helicopter varies its altitude h inside the canyon. The helicopter is located between two cliffs having the same height H and being separated by a distance L. The semi-aperture of the cone representing the visible sky area from the helicopter's point of view has been called θ, while $\phi = 90^{\circ} - \theta$ is the angle between the local horizontal plane and the cone.

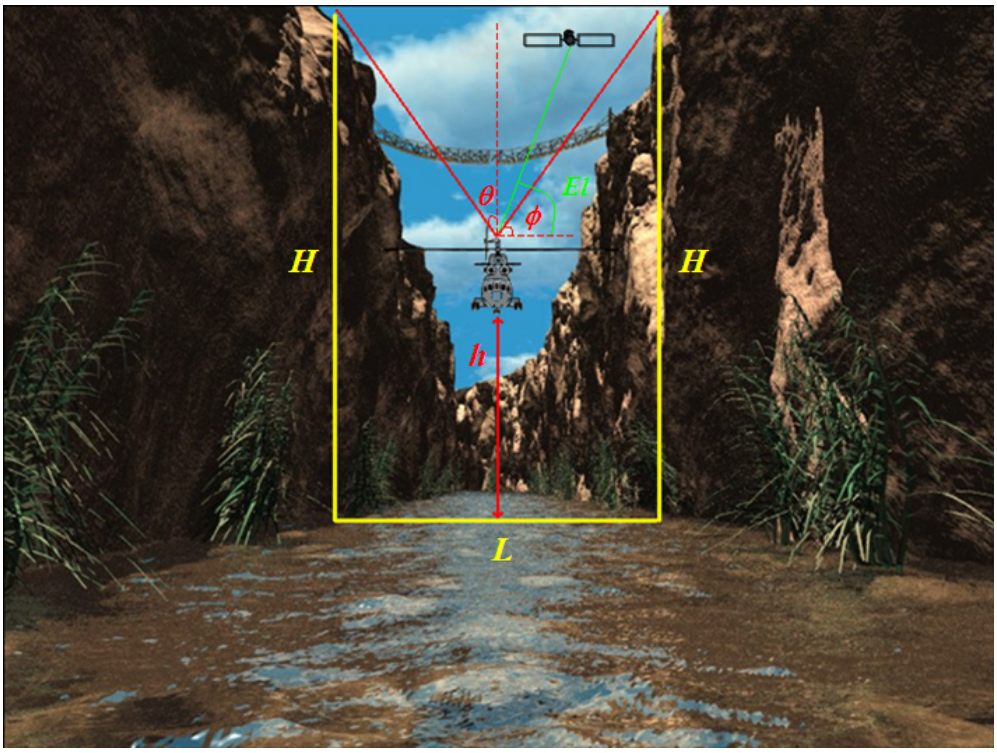

Fig. 7.16 Representation of the simulation's scenario

It is simple to verify that the satellite's angle of elevation, El, has to satisfy the following restrictions in order to be visible by the helicopter:

$$\phi \leq El \leq 90^{o} \tag{7-3}$$

Since we are interested in determining the satellite visibility based on the helicopter's altitude, the angle ϕ must be defined as a function of h. First, the angle θ is determined:

$$\theta = \tan^{-1}\left(\frac{L/2}{H-h}\right) \tag{7-4}$$

Then, by observing that ϕ and θ are complementary angles, we obtain the desired expression:

$$\phi = 90^{o} - \tan^{-1}\left(\frac{L/2}{H-h}\right) \tag{7-5}$$

As the helicopter's altitude increases, the angle ϕ becomes smaller. The limit case is when $h = H$: the helicopter is located at the top edge of the canyon, no obstacles block the GPS signals, therefore it corresponds to a situation of full satellite visibility.

The results of Fig. 7.17 show the variation of the number of visible satellites with the helicopter's altitude, where it was assumed $H = L = 1000\ m$. The various lines refer to different initial positions: the latitude is fixed (vehicle located at the equator), while some different longitude values have been considered.

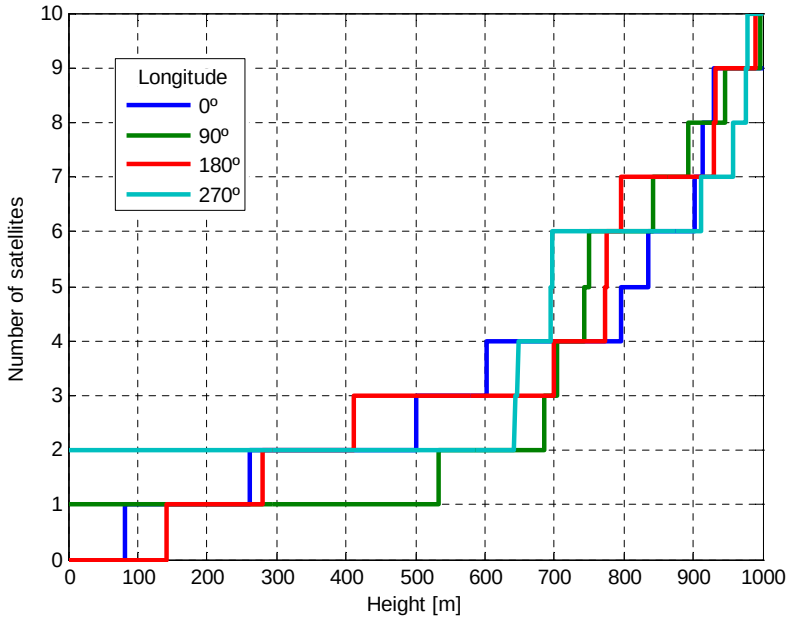

Fig. 7.17 Number of visible satellites as a function of the vehicle's height

In the worst case, the number of visible satellites is maintained below four until an altitude of 700 *m*. With 90º longitude, only one satellite is visible up to 530 *m* approximately. These results demonstrate how a GPS-only navigation system can be unreliable under such conditions.

The same results can be represented in a more elucidative way, by showing the sky portion that is visible from the helicopter's point of view. The real shape of this area is complex, as shown in Fig. 7.18; however it can be approximated as rectangular without great loss of accuracy.

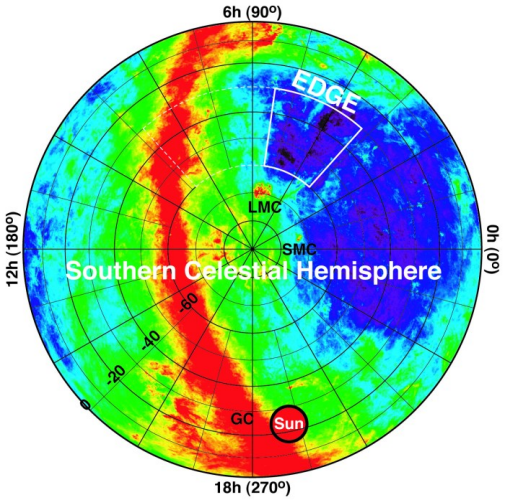

Fig. 7.18 Real shape of visible sky portion

Fig. 7.19 shows the results obtained with the vehicle located at the geodetic coordinates $(0^o, 0^o)$. The GPS satellite constellation represented in Fig. 6.1 has been considered; however, this time, the satellite position is given in terms of geodetic longitude and latitude, and a planar projection is plotted. Until a altitude of 200 *m* only satellite 17 is visible; a 200 *m* increment only causes the addition of satellite 11. The situation of four visible satellites, which permits the determination of a GPS navigation solution, is obtained only at 600 *m* height. At 950 *m* the number of satellites is 9, and a final increment of other 50 *m* permits to reach the maximum value of 10 satellites, corresponding to the situation of full visibility.

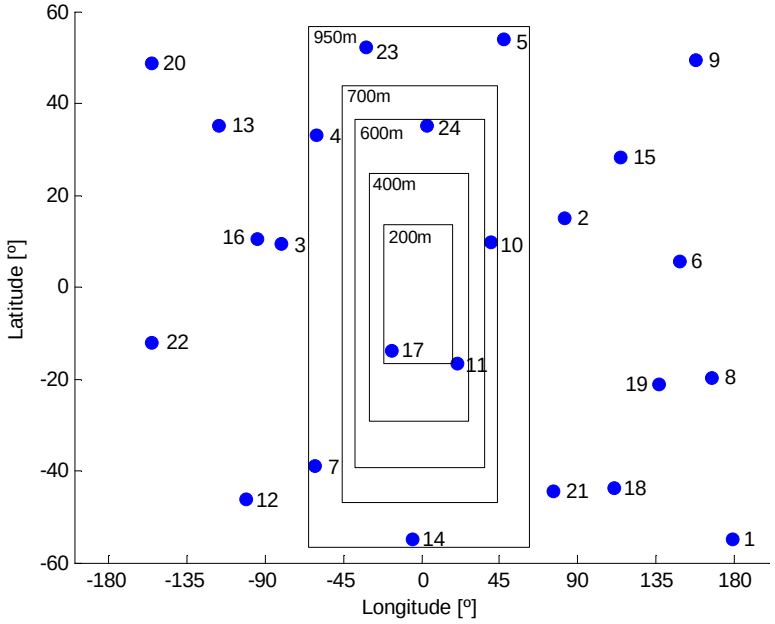

Fig. 7.19 Approximation of the visible sky portion for different altitudes

It can be proved that, even when four satellites are visible, the GPS cannot give a reliable navigation solution because of the bad satellite geometry. In fact, since the visible sky portion is limited to a narrow region, all the satellites, whose transmitted signals are used to determine the receiver's position, are not widely spread in the sky and, for this reason, they cause a lower accuracy of the solution. An easy way to demonstrate this problem is through the visualization of the DOP parameters. Considering again the case with the vehicle located at geodetic coordinates $(0^o, 0^o)$, Fig. 7.20 shows the values of the main DOPs as a function of the height inside the canyon.

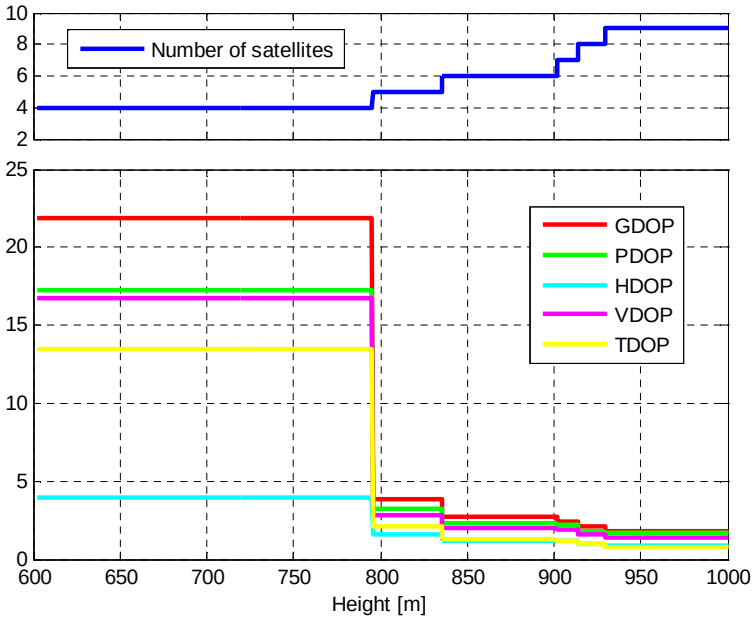

Fig. 7.20 DOP values versus height inside the canyon

Note that the dilution of precision can be evaluated only when the number of satellites is at least equal to four; in Fig. 7.17 it is possible to see that, for the situation considered here, a fourth satellite becomes visible at a height of 600 *m*. The situation of four visible satellites is maintained until approximately 800 *m*; however, during this interval the DOPs exceed reasonable values (for example, the GDOP is equal to 22). Theoretically, a navigation solution can be computed, but such high DOP values would lead to a positioning solution characterized by unacceptable accuracy. As a fifth satellite becomes available, the DOPs drop to more reasonable values; yet, the GDOP is approximately

equal to 4, which is still a high enough value to cause low positioning accuracy. Only with the addition of another satellite (which occurs around 840 *m*) the DOPs can be assumed low enough for obtaining a good solution. The GDOP is approximately equal to 3 until 900 *m*; then, the number of satellites quickly increases up to 10, and optimal DOP values are achieved.

7.4.2.2 Performance during partial and complete GPS outages

In order to assess the performance of the integrated system in situations similar to the one presented above, numerical simulations with partial GPS availability have been run. Specifically, several GPS outages (or gaps) were simulated: each gap has a duration of 40 seconds, and their individual location is illustrated in Fig. 7.21.

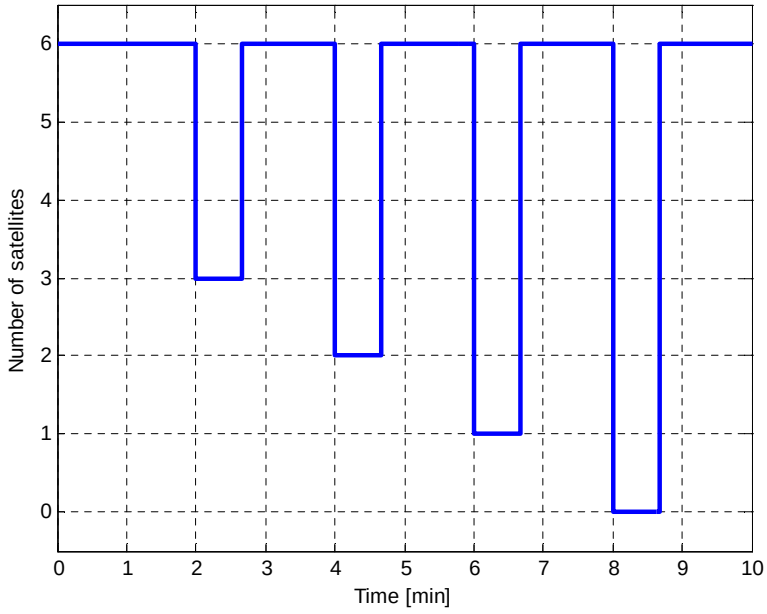

Fig. 7.21 Number of satellite for simulations with GPS data gaps

During all other periods, the number of satellites is set to six. Although this simulation might not seem realistic, the reason why it was run is to evaluate the level of deterioration in accuracy of the integrated system when three, two, one or no GPS measurements are available.

Similarly to what was done in section 7.4.1, we begin with the analysis of the results obtained for the low-cost MEMS-IMU using the two integration approaches. In this case, it is more interesting to observe the performance in terms of absolute position and velocity errors, which are shown in Fig. 7.22 and 7.23 for the loosely coupled and tightly coupled integrations, respectively.

For the loosely coupled integration, a number of satellites lower than four implies the absence of the GPS solution. Therefore in all situations of GPS outages, regardless the number of available satellites, the overall solution of the integrated system is the INS-only solution without any external aid. From Fig. 7.22 it is possible to see that the error growth, for both position and velocity, is similar during all the simulated gaps except for the first one. This result is associated to the current performance given by the filter for the estimation of the INS errors. This part related to the sensor error estimation will be comprehensively analyzed in the following section.

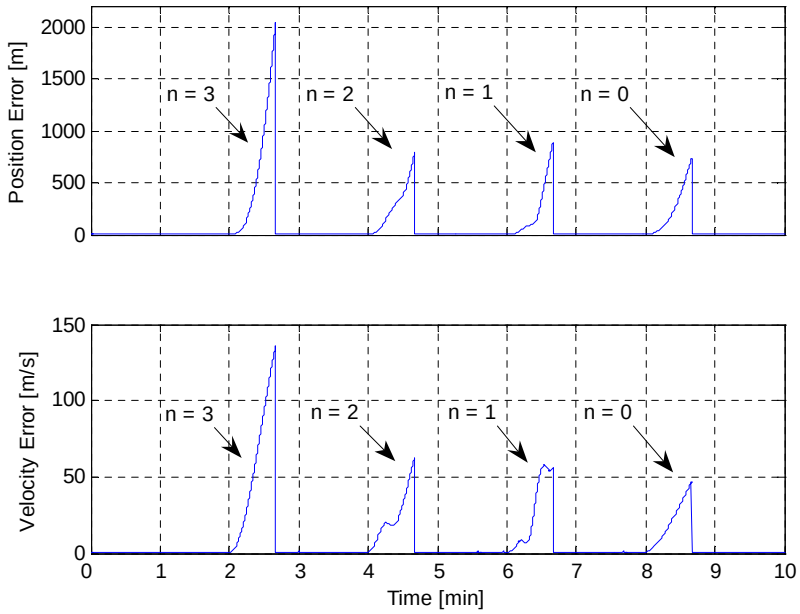

Fig. 7.22 Absolute position and velocity errors (LC integration)

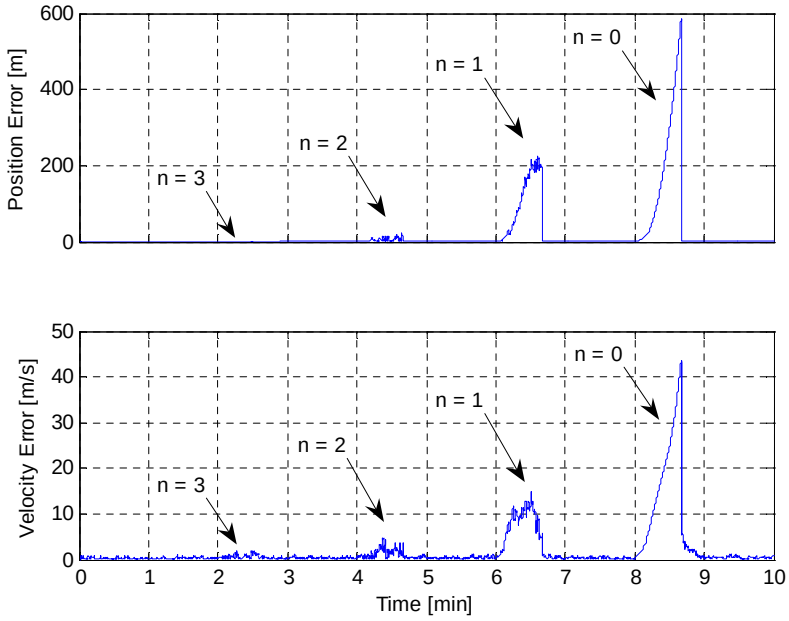

Fig. 7.23 Absolute position and velocity errors (TC integration)

For the tightly coupled integration the performance is significantly improved. With a number of satellites lower than four the integrated system can still give a solution with a level of accuracy that may be satisfactory depending on the specific application. With three satellites available the loss of accuracy is scarcely visible. With two satellites the errors start to grow reaching a maximum value of approximately 20 *m* for position, and 4 *m/s* for velocity. In the last two intervals, with one or no visible satellites, the errors become very large. It is interesting to notice that, for both the integration approaches, at the end of each GPS data gap, the errors become small again after a very short period of time (1 or 2 seconds).

The 3D navigation solutions, obtained with the two integration approaches, and the reference trajectory are shown in Fig. 7.24. Even though the axes scales are not set equal, it is possible to verify that the position error is larger along the vertical direction, as expected.

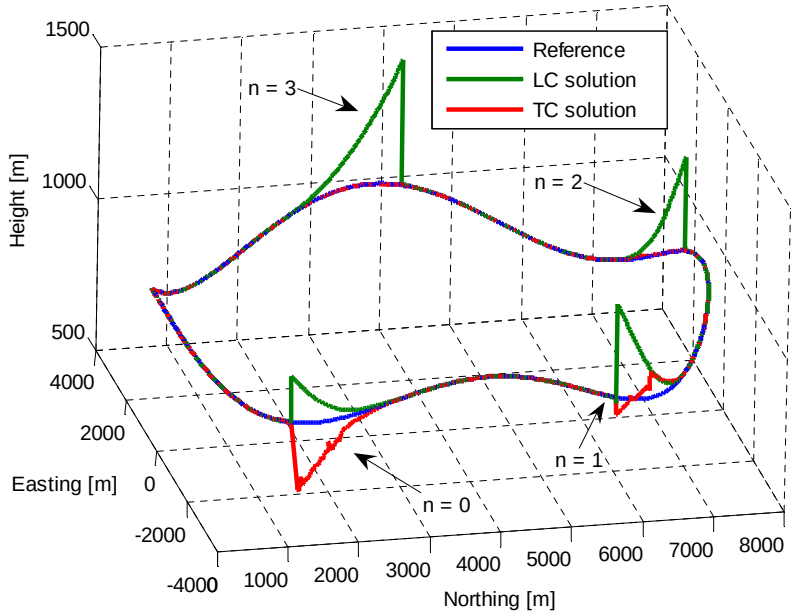

Fig. 7.24 3D navigation solutions and reference trajectory

For the attitude errors, the tightly coupled scheme also gives better results than the loosely coupled, as visible from Fig. 7.25.

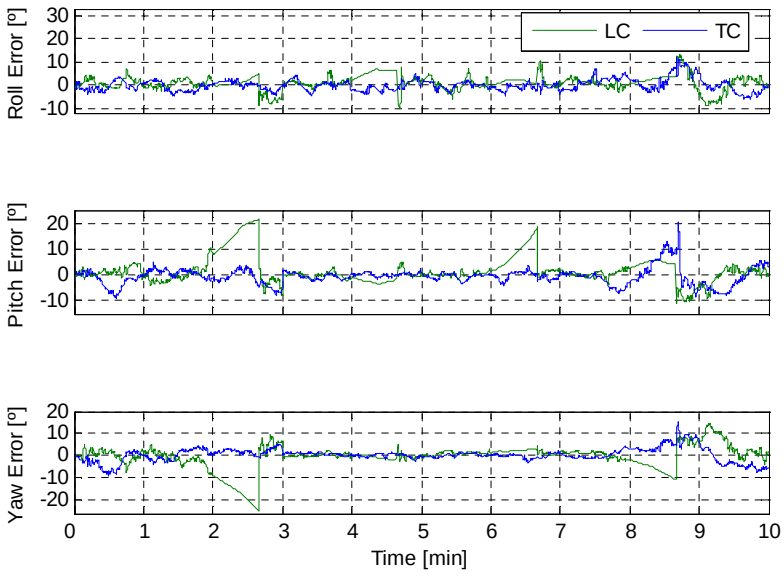

Fig. 7.25 Attitude errors for LC and TC integrations

During the gaps the errors become very large with the LC integration, reaching a maximum absolute value of approximately 20 degrees. For the TC integration,

the only interval where the error is clearly larger is the last one where no satellites at all are available. Note that the attitude errors during the periods where the satellite visibility is good are slightly higher than the ones obtained in the previous section. There are two possible reasons that caused this partial deterioration: firstly, the number of satellites during these periods is equal to six, while for the previous simulations it was averagely eight; secondly, the continuous losses of GPS signals make it more difficult for the INS filter to estimate precisely the sensor errors.

Finally, in the same way as it was done for the situation of full satellite availability, the solutions obtained with IMUs of different quality have been compared. This time it is more interesting to plot the maximum absolute error reached during each GPS data gap rather than the RMS values. These results are shown in Fig. 7.26 and are also summarized in Tab.7.5.

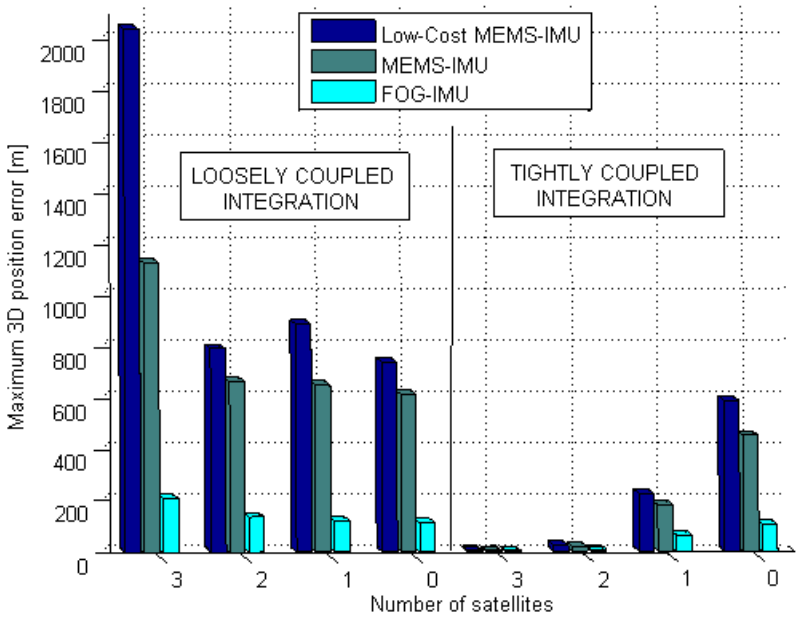

Fig. 7.26 Maximum 3D position errors with GPS outages for different IMUs

Tab. 7.5 Maximum 3D position errors with GPS outages for different IMUs

Maximum 3D error (m)	LC				TC			
Number of satellites	3	2	1	0	3	2	1	0
Low-Cost MEMS-IMU	*2033*	*791*	*885*	*738*	*4.8*	*23.4*	*226*	*585*
MEMS-IMU	*1125*	*663*	*649*	*612*	*4.2*	*18.7*	*180*	*449*
FOG-IMU	*210*	*137*	*121*	*111*	*3.9*	*7.8*	*62*	*103*

Once again, these results confirm the better performance of the tightly coupled integration. In the situations with one or no satellites available, the INS system assumes the major role in the determination of the navigation solution, since the GPS aid is very limited. Therefore, with better quality IMUs, the accuracy of the integrated system is significantly affected. The performance of the two MEMS-based IMUs are slightly different; instead, a great improvement is given by the FOG-IMU, which reaches a maximum position error of 103 *m* during the period of complete GPS outage (with the tightly coupled scheme).

7.4.3 Analysis of observability

Using pseudorange and Doppler measurements, the position and velocity errors are directly observable. However, an observability analysis of the system is of most interest since a large number of variables has to be estimated: besides position and velocity errors, there are the attitude errors, as well as all the sensor errors (turn-on bias, bias drift, and scale factor error). Only when the system is completely observable can the rest of the states be estimated from the pseudorange and Doppler measurements.

In general, a discrete-time system with dynamics matrix F and design matrix H (as described in section 4.1) is observable if the observability matrix below is non-singular [16]:

$$K_O = \begin{bmatrix} H^T & F^T H^T & F^{T^2} H^T & \cdots & F^{T^{n-1}} H^T \end{bmatrix} \tag{7-6}$$

where *n* is the number of states. The system is completely observable if the rank of the observability matrix is equal to the system dimension:

$$rank\left(K_O\right) = n \tag{7-7}$$

If Eq. (7-7) is satisfied it means that the attitude errors as well as the sensor errors are all observable within the Kalman filter. However, if the rank of the observability matrix is less than *n*, it means that some of the state components

are unobservable within the Kalman filter. As a result, the accuracy of all state estimates that are not directly measured cannot decrease below a certain bound. For INS/GPS integration, the states may also be non-orthogonal to each other causing the system to be only partially observable.

Considering our problem, theoretically deriving the analytical expression of Eq. (7-6) is very difficult; however, a numerical approach can be used. The observability matrix is determined at each filtering step, and its rank is evaluated.

Fig. 7.27 illustrates the results obtained in the situation of full GPS data availability with good satellite geometry.

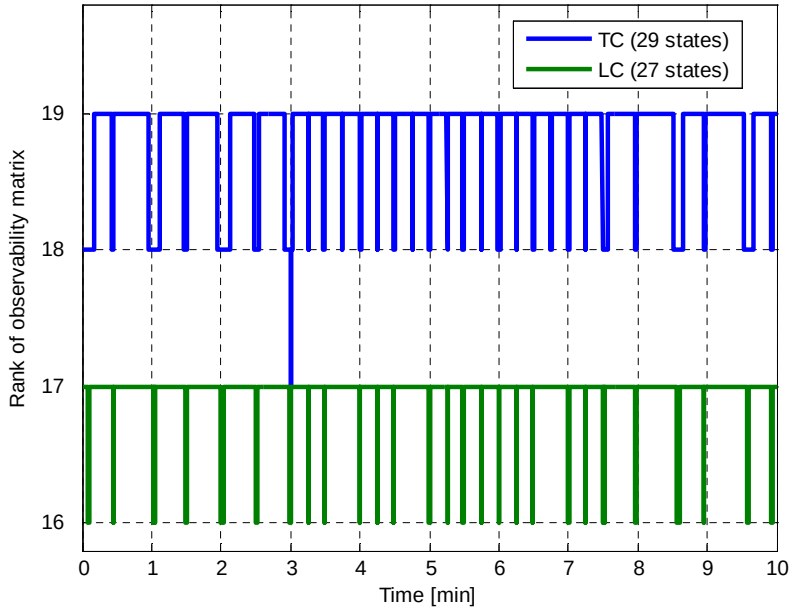

Fig. 7.27 System observability (no GPS outages)

For both the TC and LC integrations the system is not completely observable, with the number of non-observable states varying between 10 and 11. Although these results may appear quite negative, it was proved experimentally that the filter estimates do not diverge substantially. To give an idea of how this partial system observability affects the filter estimates, Fig. 7.28, 7.29, and 7.30 show the results obtained during one simulation using the TC integration. These plots represent the comparisons between the real sensor error values and their corresponding estimates, including all the accelerometers and gyros errors along the three body axes.

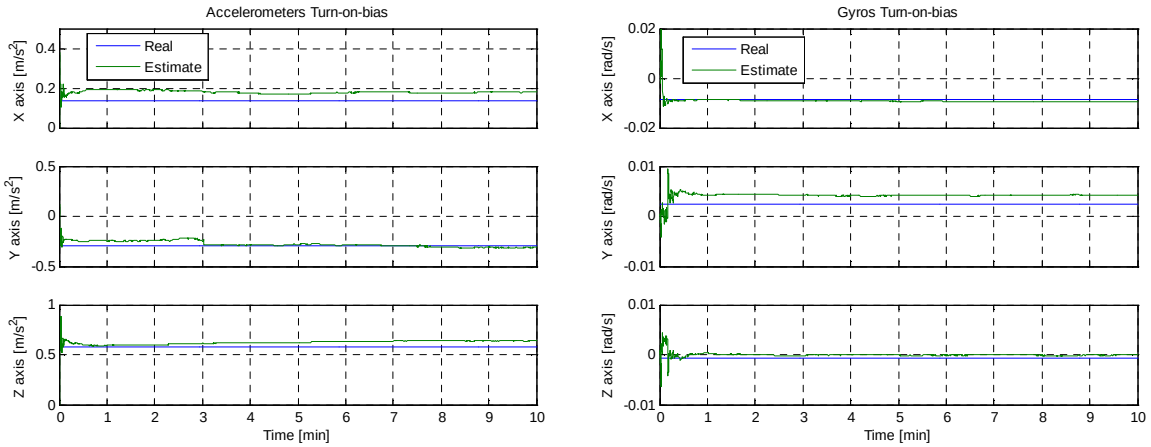

(a) Accelerometers **(b) Gyros**

Fig. 7.28 Tri-axial turn-on-bias estimates

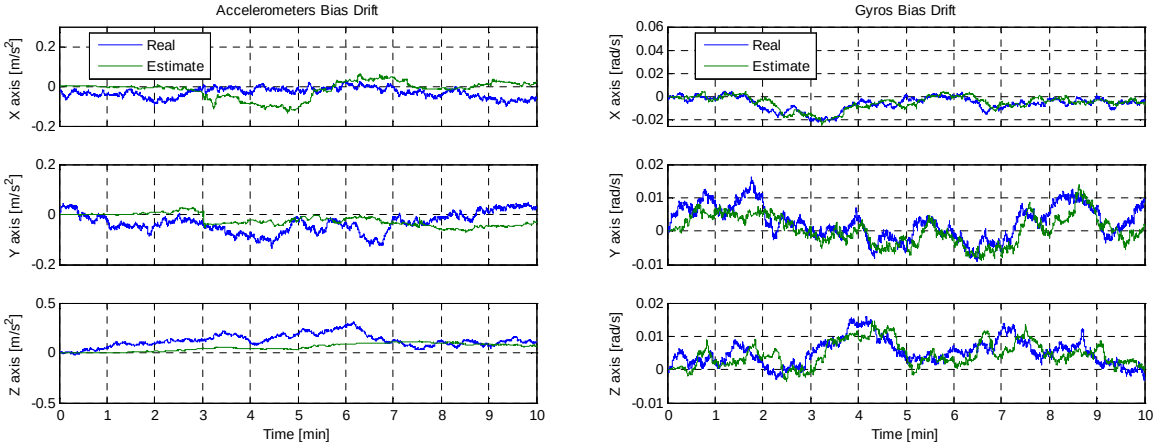

(a) Accelerometers **(b) Gyros**

Fig. 7.29 Tri-axial bias drift estimates

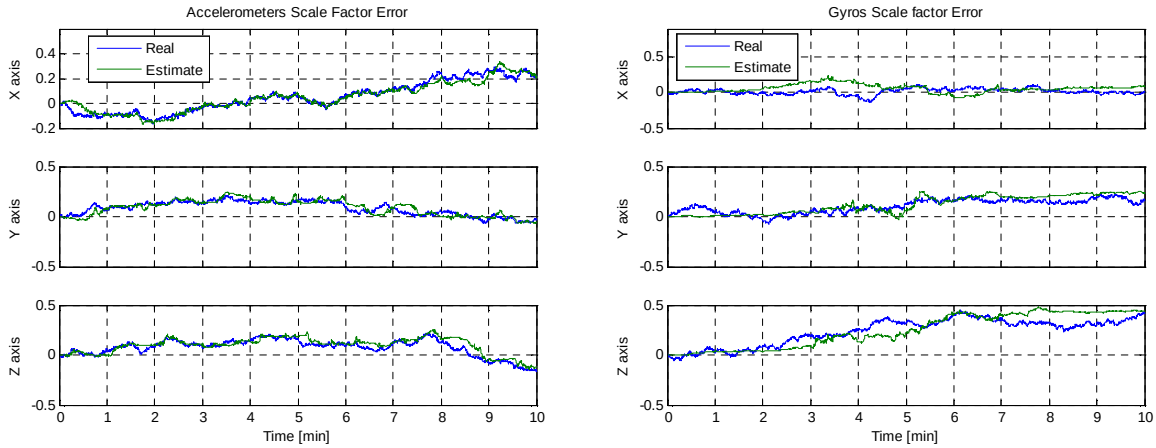

(a) Accelerometers **(b) Gyros**

Fig. 7.30 Tri-axial scale factor error estimates

In general, these results confirm the difficulty of the filter to estimate precisely all the errors. As expected, the results vary depending on the direction considered. The turn-on bias estimates show a residual error that the filter is not capable to eliminate; some of these residuals are very large, depending on the particular axis. It is possible to evaluate the relative error, expressed as a percentage, by using the following equation:

$$relative\ error = \frac{estimate - real\ value}{real\ value} \cdot 100 \tag{7-8}$$

Tab. 7.6 contains the relative errors calculated for both accelerometers and gyros. Of all the three directions, only one value is significantly higher than the others: for the accelerometers it is 25.2%, obtained along the *X* axis; for the gyro it is 53.8% along the *Y* axis. This proves that the actual vehicle's maneuvering has a great influence on the capability of the filter to provide good estimates. Theoretically, the more variable with time the sensor measurements are, the better will be the filter performance.

Tab. 7.6 Residual errors of turn-on-bias estimates

Residual Error	X	Y	Z
Accelerometers	*25.2%*	*5.0%*	*8.8%*
Gyros	*9.1%*	*53.8%*	*7.1%*

The bias drift estimates are in general good for the gyros, while for the accelerometers they show some difficulties in tracking precisely the corresponding real quantities. We can associate these less precise results to the fact that these variables are among the non-observable ones during the entire simulation.

Finally, the scale factor error estimates seem to have less problems to follow the real values, and for both accelerometers and gyros the results present a similar good level of accuracy.

A completely different result is obtained when considering the estimates of the GPS receiver clock errors. The loosely coupled integration has a specific GPS filter to estimate these quantities; the tightly coupled INS/GPS filter must contain

the states corresponding to these errors since the GPS filter is eliminated with this configuration (see Chapter 5). However, the GPS measurements (pseudorange and Doppler) are directly related to these errors; thus, their estimations will be extremely accurate along the entire simulation, regardless the type of approach being used. This is clearly visible from Fig. 7.31, where the errors are presented in terms of equivalent position and velocity. Note that it is essential to obtain good estimates of the clock errors because they assume large values after a short period of time.

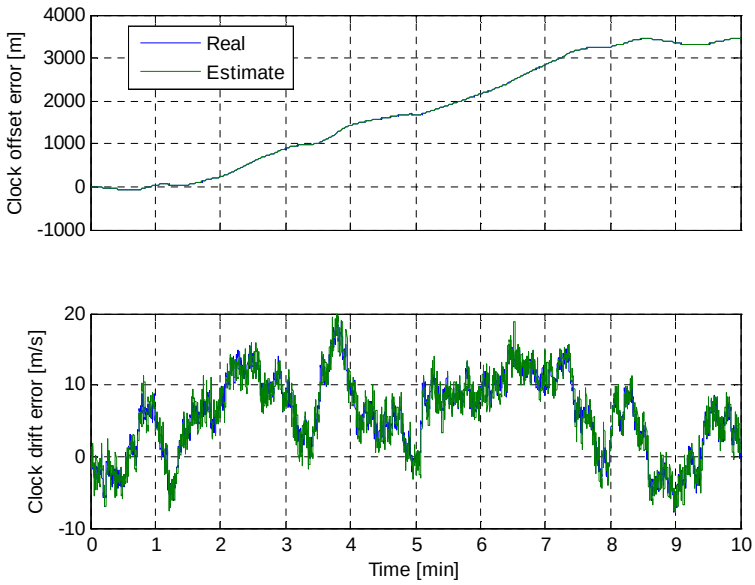

Fig. 7.31 GPS receiver clock errors estimates

We saw that the vehicle's type of maneuvering affects the filter performance. As an example, in section 7.4.1 a simulation with the vehicle moving in a straight line with a constant velocity was run to show that the yaw angle error becomes non-observable in such situation. A further proof of this result is given by Fig. 7.32, which shows the rank of the observability matrix evaluated during this specific simulation. When comparing these results with the ones obtained in Fig. 7.27, it is easy to verify that, in average, the number of observable states decreased of approximately one unit.

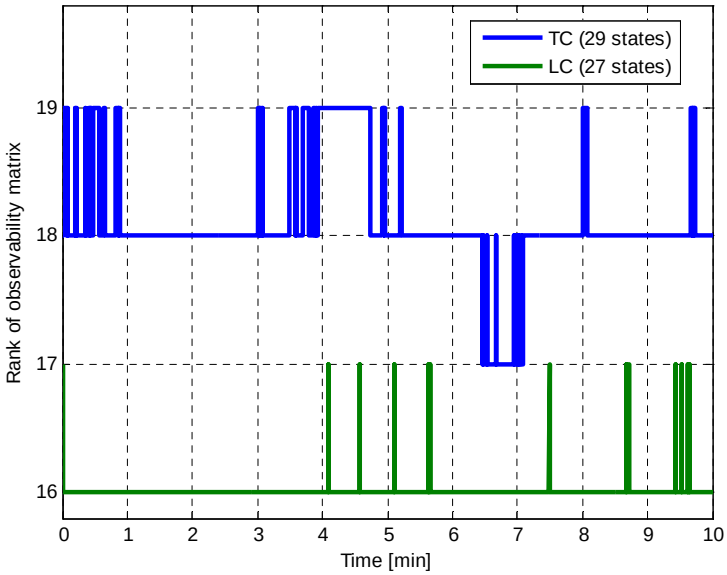

Fig. 7.32 System observability for a vehicle in straight uniform motion

The results presented so far in this section correspond to a situation of full GPS data availability with good satellite geometry. However, as the number of visible satellites drops down, the system observability is consequently affected. Using the satellite geometry illustrated in Fig. 7.21, the rank of the observability matrix has been evaluated for both the TC and LC integrations; the corresponding results are shown in Fig. 7.33.

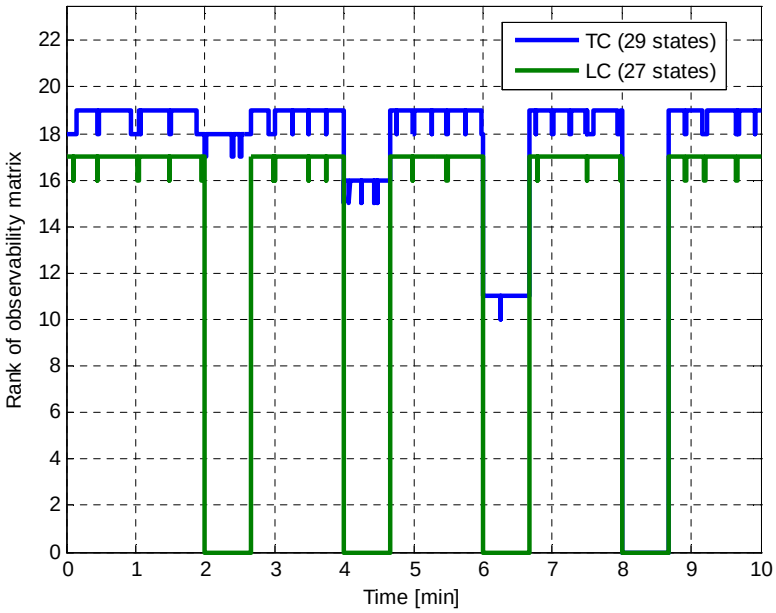

Fig. 7.33 System observability (with GPS outages)

With less than four satellites the GPS-only solution is not available and the LC integrated system can only provide the INS solution; in this case the Kalman filter algorithm for the errors estimation cannot be executed, thus explaining why the rank of the observability matrix falls to zero during the GPS outages. The tightly coupled integration, instead, can always execute the EKF, as long as at least one satellite signal is available. The system observability is gradually affected, depending on the specific number of satellites; for the worst case (one satellite), the number of observable states is equal to 10-11.

The final conclusions that can be drawn from the above observability analysis is that the filter has a limited ability in estimating accurately all the errors. The level of observability depends not only on the number of measurements available, but also on the vehicle's actual motion. However, a reduced system observability does not necessarily affect significantly the accuracy of the overall INS/GPS navigation solution when the GPS measurements are available continuously and in sufficient quantity. Some problems can occur when the number of measurements decreases and the INS solution assumes a greater importance. Poor sensor error estimates, in fact, will cause the navigation solution to diverge quickly from the correct values.

7.5 Augmentation of the INS/GPS system with Galileo

The goal of this final analysis is to assess the impact of the augmentation of the INS/GPS navigation system, using a TC integration, with Galileo (see Appendix D for a brief description of the Galileo system). Specifically, the main objective is to quantify the benefits provided by this innovative integrated system in terms of availability and accuracy of the navigation solution, as well as the system observability.

If we consider that Galileo and GPS are operated together to constitute a super-constellation, the geometry of both systems improves dramatically, as shown in Tab. 7.7 [30].

Tab. 7.7 Assumed DOPs for Galileo and GPS

Accuracy of the position (95%)	PDOP	HDOP	VDOP
GPS-only	*2.70*	*1.20*	*2.40*
Galileo-only	*2.70*	*1.20*	*2.40*
GPS+Galileo	*1.12*	*0.50*	*1.00*

To compute the total positioning error resulting from processing signals coming from Galileo and GPS, the following expression is employed [30]:

$$err_{GPS+GAL} = \sqrt{\frac{2}{\frac{1}{\sigma_{GPS}^2} + \frac{1}{\sigma_{GAL}^2}}} \cdot DOP_{GPS+GAL} \tag{7-9}$$

where σ refers to the UERE budget of Galileo and GPS, respectively. The worst and typical cases of UERE budgets for Galileo and GPS services, obtained with a narrow correlator receiver with two different signal bandwidths (namely, 8 *MHz* and 24 *MHz*), are displayed in the following table [30].

Tab. 7.8 Galileo and GPS UERE budgets for typical and worst cases

UERE budget (m)	$L1_{B,C}$ (8 MHz)	$L1_{B,C}$ (24 MHz)	C/A (8 MHz)	C/A (24 MHz)
Typical case	*4.18*	*3.64*	*5.50*	*5.14*
Worst case	*9.82*	*7.57*	*10.36*	*8.31*

Tab. 7.9 gives the 3D RMS values for position, velocity, and attitude errors obtained through simulations of a simple INS/GPS system, and of a INS/GPS+Galileo system using the UERE budgets for a typical case. The augmented system has, in average, a number of available measurements equal to 16 (the double as for the other case).

Tab. 7.9 3D RMS accuracy for INS/GPS and INS/GPS+GALILEO systems

3D RMS accuracy	Position	Velocity	Attitude
INS/GPS	*2.98 m*	*0.165 m/s*	*1.80º*
INS/GPS+GALILEO	*1.36 m*	*0.116 m/s*	*1.39º*

All quantities show some degree of improvement; the most significant is obtained for the position error, where a 54% increase of accuracy is achieved. Although a more accurate overall navigation solution can be obtained, the

increased number of available measurements (pseudorange and Doppler) does not improve significantly the system's estimation capabilities. This is proved by the analysis of the system observability, shown in Fig. 7.34 (for the TC integration).

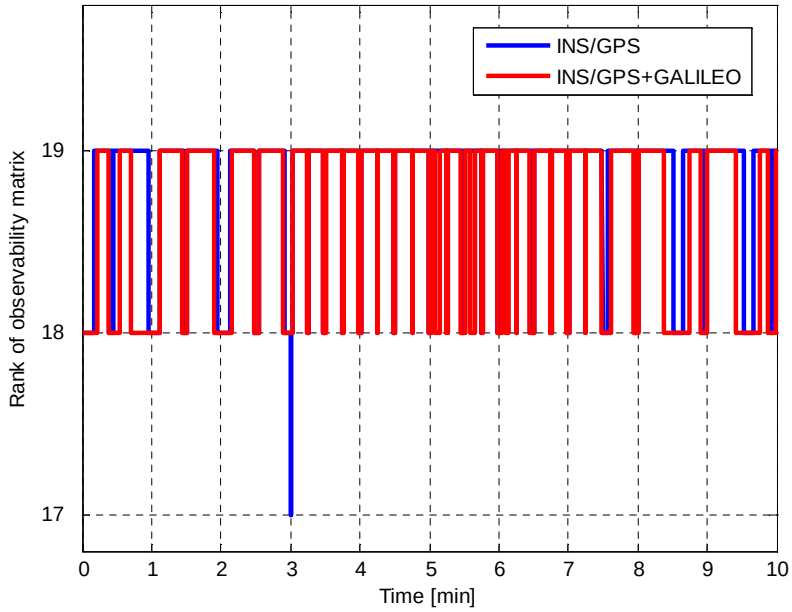

Fig. 7.34 Observability of INS/GPS and INS/GPS+GALILEO systems

Once again, the maximum number of observable states is limited to 19. An interesting comment is that the variation with time of the rank of the observability matrix for the two systems is very similar, and for some periods it is exactly coincident. This proves that the actual vehicle's motion has a greater influence than the actual number of available measurements.

Whereas no significant improvement is visible from the figure above, another important advantage (besides the increased accuracy of the solution) can be outlined by considering once again the example of a helicopter's canyon flight (see section 7.4.2.1). Fig. 7.35 shows the total number of GPS/Galileo satellites as a function of the vehicle's height inside the canyon. When comparing these results with those of Fig. 7.17, it is possible to see that a great improvement is obtained. With the GPS constellation only, a situation of 4 visible satellites is reached at 600 *m* altitude (in the best case); with the addition of Galileo, this condition is achieved much earlier (around 200 *m* for the vehicle located at -90º longitude).

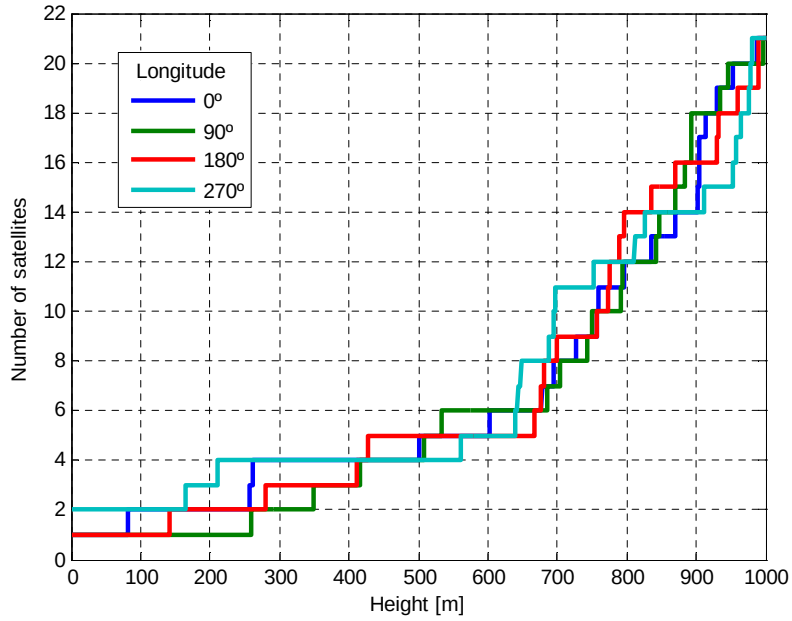

Fig. 7.35 Number of visible satellites as a function of the vehicle's height

Another way to visualize the improvement obtained with the addition of Galileo is through Fig. 7.36, which gives a 2D representation of the two satellite constellations and of the approximated visible sky portion from the point of view of the vehicle, displayed for different altitudes.

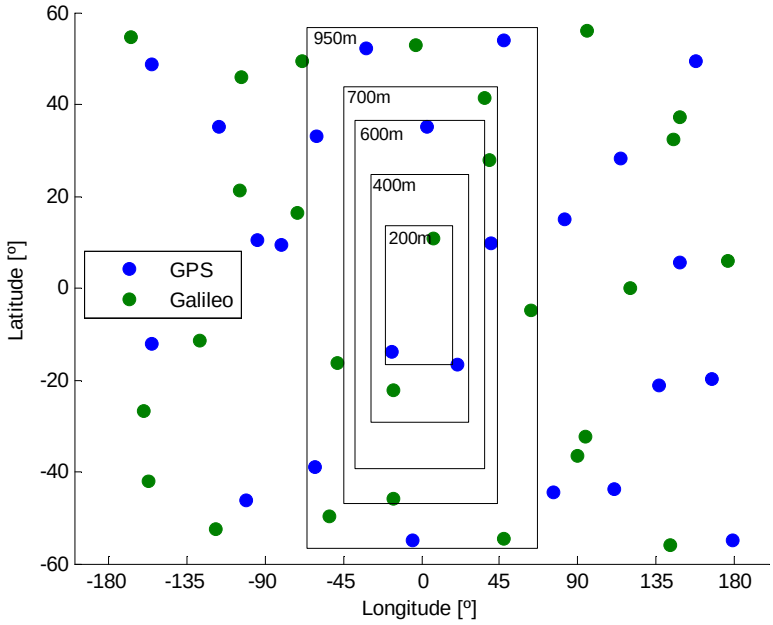

Fig. 7.36 Approximated visible sky portion and GPS/GALILEO satellites

Note that, although the Galileo satellite constellation has been already defined, the relative position with respect to the GPS constellation is not known at the moment. Thus, various simulations with different initial Galileo satellite positions have been run, and it has been verified that the results are not significantly affected by these variations. A maximum difference of 1-2 visible satellites has been obtained for intervals shorter than 100 *m*.

The main conclusion that can be drawn from this last analysis is that the major advantages of the augmentation of an INS/GPS system with Galileo are mostly related with increased accuracy and availability of the navigation solution. In other words, this new integrated system is characterized by higher reliability and robustness, in a sense that it is able to provide an accurate navigation solution with more availability. However, the addition of another satellite navigation system, based on the same working principle as the GPS and offering the same type of measurements, does not improve the estimation capabilities of the integrated system.

Chapter 8

Conclusions and Recommendations

This chapter contains a summary of the research presented in this thesis, the conclusions drawn from the tests results, and some recommendations for future work in INS/GPS integration.

8.1 Summary

The work presented in this thesis dealt with the assessment of a low-cost INS/GPS integrated system for airborne applications. The motivation for using an integrated system is that the GPS signal does not always reach the user, and thus continuous positioning is not possible through a navigation system based exclusively on GPS (canyon effect).

The GPS and INS sensors have been integrated using two approaches, namely, the loosely coupled and the tightly coupled. Both these strategies have been implemented using a closed-loop configuration. Two types of GPS filters have been implemented, a PV and a PVA. The INS filter contains the navigation error states (position, velocity, and attitude), and the inertial sensor error states based on the typical characteristics of low-cost inertial sensors; additionally, for the case of tightly coupled integration, the filter (which has been referred to as INS/GPS filter) is also augmented with the two error states of the GPS receiver clock.

Both the integration strategies have been used to evaluate the performance of the INS/GPS system; the main differences, specific advantages, and limitations of each approach have been outlined. An innovative INS/GPS+Galileo system has also been analyzed.

8.2 Conclusions

The main objective of this thesis was to develop and test different INS/GPS strategies for low-cost airborne navigation. This goal has been met with the development of a software through which it has been possible to perform several types of simulations and tests.
The following conclusions can be drawn from the results obtained:

- The low-cost MEMS-based IMU, characterized by several types of error sources, shows a very poor performance when compared to other IMUs of higher quality. The errors of its navigation solution become unacceptable after short periods of time, even when an initial calibration is performed.
- The PV and PVA models for the GPS filter show no significant difference in their performance for vehicle's low dynamics. However, the importance of using a model which takes into account the quick variations of acceleration is evident in situations of vehicle's high dynamics.
- The INS/GPS integrated system provided a level of position accuracy which is directly associated to the GPS-only solution in a situation of good satellite geometry and no GPS outages.
- Velocity error trends are analogous to position error trends under consistent GPS availability.
- The attitude errors show a behavior that is less GPS-dependent, in a way that they appear to be less noisy and with slower time variations. The maximum error values that have been obtained might not be acceptable for some specific applications. This validates the requirement for additional external aiding (for instance, a magnetic compass).
- Under full satellite visibility, the performance of the low-cost INS/GPS system is comparable to the one of an integrated system which uses a better quality MEMS-IMU, or even a tactical grade IMU.
- The loosely coupled and tightly coupled integrations provide similar accuracy under full satellite visibility. Under such conditions, a loosely coupled integration strategy is preferred due to its easier implementation and lower computational load.

- In contrast, the tightly coupled scheme has shown a superior performance relative to the loosely coupled case in situations of partial or complete GPS outages. With this strategy, the integrated system is able to maintain the errors under a reasonable bound even when only 3 or 2 satellites are available. With 1 or no satellites at all, the errors become too large after a 40 *s* outage due to the low quality of the inertial sensors, which assume much importance during these periods.
- The quick growth of navigational errors during GPS outages is partially due to the difficulty of the INS filter to estimate correctly and precisely the numerous error sources of the inertial sensors. In terms of observability, the integrated system has shown some limitations even in situations of full satellite visibility.
- The augmentation of the INS/GPS system with Galileo has shown some improvements in terms of accuracy and availability of the solution; with a greater number of available measurements, the integrated system becomes more reliable and robust. However, in terms of system observability and sensor error estimation, no improvements have been obtained.
- The ultimate conclusion of this work is that the low-cost INS/GPS integrated system performs reasonably well in different operating environments and partially outperforms the GPS-only system in terms of navigation solution accuracy, availability, and reliability. At times, the performance of the low-cost INS/GPS system has shown to be comparable to the one of an integrated system using a tactical grade IMU. Therefore the results presented in this work strongly indicate the potential of low-cost INS/GPS for use in airborne applications.

8.3 Recommendations

The following recommendations can be made for future investigation on low-cost INS/GPS systems:

- The investigation of the system performance through the addition of measurements from other navigation instruments is necessitated. Typically, in airborne applications, such instruments can be a barometric altimeter, a magnetic compass, a VOR, etc. More measurements from systems which are based on different physical principles can aid the errors estimation and improve the system observability.
- The use of vehicle's position and velocity constraints during some non-crucial flight phases (for example, en-route) can provide some improvements in situation of partial GPS outages.
- The INS/GPS performance can be further improved by using recently developed map-matching techniques. Such methods provide additional map-derived motion constraints, that can potentially help to maintain the INS errors smaller in the complete absence of GPS signals [3].
- The usage of multiple GPS antennas can provide more accurate attitude information in situations of full satellite availability. This technique, called Attitude Heading Reference System (AHRS), permits to use lower quality IMUs and, thus, is more economical to implement than other conventional techniques [12].
- The estimation technique used in this work is the (extended) Kalman filter. Further investigation may be oriented to the use of other adaptive and nonlinear filtering methods, including particle filters [18].
- In the thesis, GPS-inertial systems have been mechanized by combining the information from GPS and INS using either a loose integration or tight integration. A third scheme of integration could be implemented instead, in which the inertial sensors would be used to aid the GPS phase/frequency and code tracking loops directly. This level of coupling is usually referred to as ultra-tight or deep integration [1], and it seems to offer potential improvements to GPS performance such as more resistance to radio frequency interference or multipath effect.

References

[1] Alban, S., Akos, D. M., Rock, S. M., and Gebre-Egziabher, D. (2003). *Performance Analysis and Architectures for INS-Aided GPS Tracking Loops*. ION National Technical Meeting Proceedings, pp. 611-622, Anaheim, CA.

[2] Bao J., and Tsui, Y. (2000). *Fundamentals of Global Positioning System Receivers: A Software Approach*. John Wiley & Sons, Inc., New York, NY.

[3] Basnayake, C., et al. (2005). *An HSGPS, Inertial and Map-Matching Integrated Portable Vehicular Navigation System for Uninterrupted Real-Time Vehicular Navigation*. International Journal of Vehicle Information and Communication Systems, Vol. 1, No. 1/2, pp. 131-151, Inderscience Enterprises Ltd.

[4] Beeby, S., Graham, E., Kraft, M., White, N. (2004). *MEMS Mechanical Sensors*. Artech House, Inc., Boston, MA.

[5] Bottasso, C. L. (2005). *Three-Dimensional Rotations*, Lecture Notes, Dept. of Aerospace Eng., Politecnico di Milano, Milan, Italy.

[6] Brown, R. G., and Hwang, P. Y. C. (1997). *Introduction to Random Signals and Applied Kalman Filtering, 3rd ed*. John Wiley & Sons, Inc., New York, NY.

[7] Crista Inertial Measurement Unit Interface/Operation Document, (2004). http://www.cloudcaptech.com, Cloud Cap Technology, Hood River, OR.

[8] El- Mowafy, A. (2005). *Multiple Reference Station GPS Networks for Airborne Navigation*. Journal of Global Positioning Systems, Vol. 4, No. 1-2, pp. 2-11, CPGPS, Calgary, Canada.

[9] El-Rabbany, A. (2002). *Introduction to GPS: the Global Positioning System*. Artech House, Inc., Boston, MA.

[10] European Commission. (2007). *GALILEO - European Satellite Navigation System*. (Updated 02 June 2006). Available from: http://ec.europa.eu/dgs/energy_transport/galileo/

[11] Farrel, J. A., and Barth, M. (1999). *The Global Positioning System and Inertial Navigation*. McGraw-Hill, New York, NY.

[12] Gebre-Egziabher, D., Hayward, R. C., and Powell, J. D. (1998). *A Low-Cost GPS/Inertial Attitude Heading Reference System (AHRS) for General Aviation Applications*. Position Location and Navigation Symposium, IEEE, pp. 518-525, Palm Springs, CA.

[13] Godha, S., and Cannon, M. E. (2005). *Integration of DGPS with a Low Cost MEMS-Based Inertial Measurement Unit (IMU) for Land Vehicle Navigation Application*. Proceedings of ION GNSS, pp. 333-345, San Diego, CA.

[14] Godha, S. (2006). *Performance Evaluation of Low-Cost MEMS-Based IMU Integrated with GPS for Land Vehicle Navigation Application*. MSc Thesis, Dept. of Geomatics Eng., University of Calgary, Calgary, Canada.

[15] Goldstein, H., Poole, C., and Safko, J. (2002). *Classical Mechanics, 3rd ed.* Addison-Wesley, Cambridge, MA.

[16] Grewal, M. S., and Andrews, A. P. (2001). *Kalman Filtering: Theory and Practice Using MATLAB*. John Wiley & Sons, Inc., New York, NY.

[17] Grewal, M. S., Weill, L. R., and Andrews, A. P. (2001). *Global Positioning Systems, Inertial Navigation, and Integration*. John Wiley & Sons, Inc., New York, NY.

[18] Gustafsson, F., et al. (2001). *A framework for Particle Filtering in Positioning, Navigation and Tracking Problems*. Proceedings of the 11th IEEE Signal Processing Workshop, Vol. 50, Issue 2, pp. 34-37.

[19] Kaplan, E. D., and Hegarty, C. J. (2006). *Understanding GPS: Principles and Applications, 2nd ed*. Artech House, Inc., Boston, MA.

[20] Kayton, M, and Fried, W. (1997). *Avionics Navigation Systems, 2nd ed.* John Wiley & Sons, Inc., New York, NY.

[21] Levy, L. J. (1997). The *Kalman Filter: Navigation's Integration Workhorse*. Innovation Column of GPS World. Available from: http://www.cs.unc.edu/~welch/kalman/Levy1997.

[22] Li, Y., Mumford, P., Wang, J., and Rizos, C. (2006). *Development of a GPS/INS Integrated System on the Field Programmable Gate Array Platform*. Proceedings of ION GNSS, pp. 2222-2231, Fort Worth, TX.

[23] Marion, J. B., and Thornton, S. T. (1995). *Classical Dynamics of Particles and Systems, 4th ed.*,Harcourt, Inc., Orlando, FL.

[24] MATLAB R2007a, Product Documentation. Available from: http://www.mathworks.com, The MathWorks, Inc., Natick, MA.

[25] Nunes, F. D. (2004). *Air Traffic Control Systems*, Lecture Notes (in Portuguese), Dept. of Electric and Computer Eng., Instituto Superior Técnico, Lisbon, Portugal.

[26] Park, M. (2004). *Error Analysis and Stochastic Modelling of MEMS based Inertial Sensors for Land Vehicle Navigation Applications*. MSc Thesis, Dept. of Geomatics Eng., University of Calgary, Calgary, Canada.

[27] Parkinson, B. W., and Spilker, J. J. Jr. (1996). *Global Positioning System: Theory and Applications, Vols. I and II*. American Institute of Aeronautics and Astronautics, Inc., Washington, DC.

[28] Petovello, M. G. (2003). *Real-Time Integration of a Tactical-Grade IMU and GPS for High-Accuracy Positioning and Navigation*. PhD Thesis, Dept. of Geomatics Eng., University of Calgary, Calgary, Canada.

[29] Qi, H., and Moore, J. B. (2002). *Direct Kalman Filtering Approach for GPS/INS Integration*. IEEE Transactions on Aerospace and Electronic Systems, Vol. 38, Issue 2, pp. 687-693.

[30] Rodriguez, J. A. A., et al. (2004). *Combined Galileo/GPS Frequency and Signal Performance Analysis*. ION GNSS 17th International Technical Meeting of the Satellite Division, Long Beach, CA.

[31] Schultz, C. E. (2006). *INS and GPS integration*. MSc Thesis, Technical University of Denmark, Lingby, Denmark.

[32] Shin, E.-H. (2001). *Accuracy Improvement of Low Cost INS-GPS for Land Application*. MSc Thesis, Dept. of Geomatics Eng., University of Calgary, Calgary, Canada.

[33] Shin, E.-H. (2005). *Estimation Techniques for Low-Cost Inertial Navigation*. PhD Thesis, Dept. of Geomatics Eng., University of Calgary, Calgary, Canada.

[34] Tapia, R. A., and Lanius, C. (2001). *Computational Science: Tools for a Changing World*. Available from: http://ceee.rice.edu/Books/CS, Rice University, Houston, TX.

[35] Wendel, J., Metzger, J., Moenikes, R., Maier, A., Trommer, G. F. (2005). *A Performance Comparison of Tightly Coupled GPS/INS Navigation Systems based on Extended and Sigma Point Kalman Filters*. Proceedings of ION GNSS, pp. 456-466, San Diego, CA.

[36] *World Geodetic System 1984 (WGS-84) - Its Definition and Relationships with Local Geodetic Systems*. NIMA TR8350.2, 3rd ed., National Imagery and Mapping Agency, St. Louis, MO.

[37] Zandbergen, R., and Navarro, D. (2006). *Specifications of Galileo and Giove Space Segment Properties Relevant for Satellite Laser Ranging*. ESA-EUING-TN/10206, Galileo Project Office, European Space Agency, Paris, France.

Appendix A

GPS Navigation Message and Orbital Parameters

Each GPS satellite broadcasts continuously a navigation data message at 50 bits per second. The message is formatted into frames of 1500 bits, which corresponds to a frame duration of 30 seconds. Each frame is organized into 5 subframes. Subframes 1-3 typically repeat the same information from frame to frame. However, subframes 4-5 of consecutive frames contain different “parts” of the navigation message. It takes 25 frames (12.5 minutes) to transfer the complete navigation message. The structure of a frame is shown in Fig. A.1. [27].

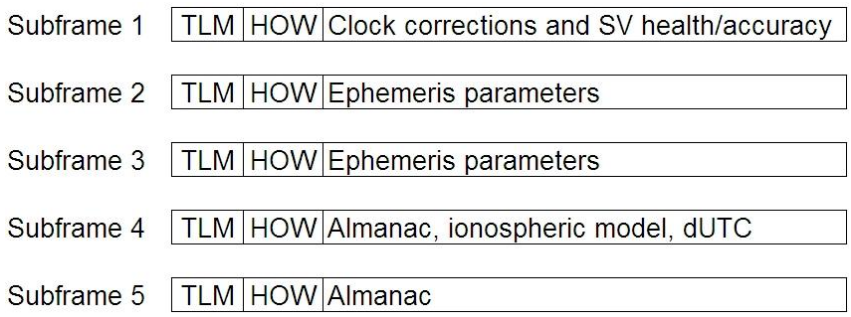

Fig. A.1 Structure of a GPS frame

The first two words of each subframe are the telemetry word (TLM) and the hand-over word (HOW). The TLM contains a synchronization pattern, while the HOW provides time information (seconds into the week) to allow the receiver to acquire the P (Y) code.

Each satellite broadcasts its own *ephemeris* in its navigation message. A coarse version of the ephemeris of all satellites in the constellation is also transmitted in the form of an *almanac*. The goal of the almanac is to permit the receiver to know the subset of satellites that are visible when a coarse position of the receiver is known.

The purely elliptical Keplerian orbit (Fig. A.2) is not sufficiently precise to define the actual GPS satellite orbit due to many perturbations to the ideal orbit, including nonspherical Earth gravitational harmonics, Lunar/Solar gravitational attraction, and solar flux [27].

Thus, the GPS orbit is modeled as a modified elliptical orbit with correction terms:

- *sin*, *cos* perturbations to the argument of latitude, orbit radius, and angle of inclination;
- rate of change of right ascension and inclination angle.

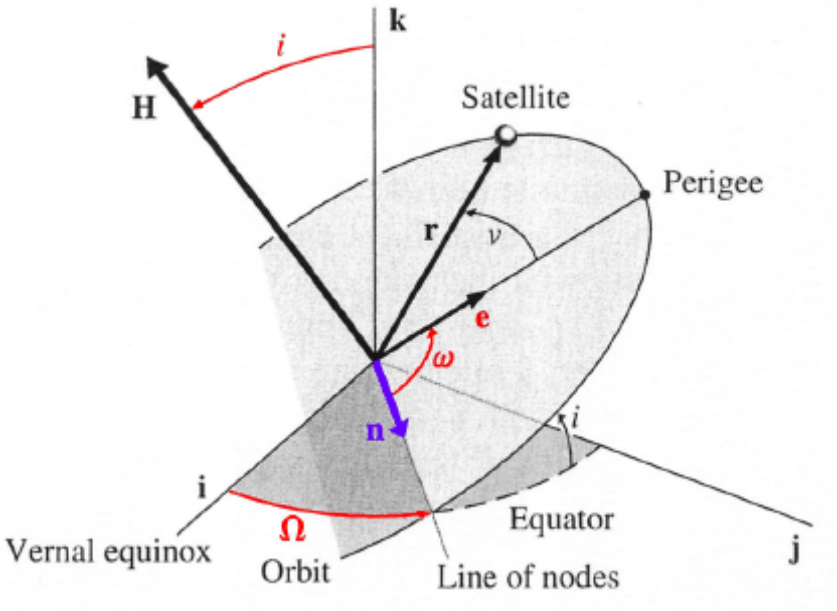

Fig. A.2 Characterization of an ideal (Keplerian) orbit

The notation used in the figure above is summarized as follows:

e	eccentricity;
i	inclination;
ν	true anomaly (at a given epoch t)
ω	argument of perigee;
Ω	right ascension of ascending node;

The last parameter that is required to completely specify the ideal elliptical orbit is the semi-major axis (*a*).

Tab. A.1 shows ephemeris model parameters which includes the sinusoidal perturbations to the orbit radius, the angle of inclination and argument of latitude, the rate of change of inclination angle, the angular rate of change of the right ascension, and the basic Keplerian parameters. The parameters for the orbit model are changed periodically and are transmitted in the ephemeris subframes. This navigation data is also transmitted in the almanac, although with a reduced precision.

Tab. A.1 Ephemeris data definition (adopted from [27])

Symbol	Definition
M_0	Mean anomaly at reference time
Δ_n	Mean motion difference from computed value
e	Eccentricity of the orbit
$(A)^{1/2}$	Square root of the semimajor axis
$(\text{OMEGA})_0$	Longitude of ascending node of orbit plane at reference time
I_0	Inclination angle at reference time
ω	Argument of perigee
OMEGADOT	Rate of right ascension
IDOT	Rate of inclination angle
C_{uc}	Amplitude of the cosine harmonic correction term to the argument of latitude
C_{us}	Amplitude of the sine harmonic correction term to the argument of latitude
C_{rc}	Amplitude of the cosine harmonic correction term to the orbit radius
C_{rs}	Amplitude of the sine harmonic correction term to the orbit radius
C_{ic}	Amplitude of the cosine harmonic correction term to the angle of inclination
C_{is}	Amplitude of the sine harmonic correction term to the angle of inclination
T_{oe}	Reference time for ephemeris
IODE	Issue of data (ephemeris)

Finally, the equations in Tab. A.2 give the center position of the satellite antenna in the WGS-84 Earth-Centered Earth-Fixed (ECEF) coordinate system for any time epoch *t*.

Tab. A.2 Elements of ephemeris model equations [27]

$\mu = 3.986005 \times 10^{14}$ m^3/s^2	WGS-84 value of the Earth's universal gravitational parameter
$\dot{\Omega}_e = 7.2921151467 \times 10^{-5}$ rad/s	WGS-84 value of the Earth's rotation rate
$A = (\sqrt{A})^2$	Semimajor axis
$n_0 = \sqrt{\mu/A^3}$	Computed mean motion–rad/s
$t_k = t - t_{oe}$[a]	Time from ephemeris reference epoch
$n = n_0 + \Delta n$	Corrected mean motion
$M_k = M_o + nt_k$	Mean anomaly
$\pi = 3.1415926535898$	GPS standard value for π
$M_k = E_k - e \sin E_k$	Kepler's equation for the eccentric anomaly E_k (may be solved by iteration), rad
$\nu_k = \tan^{-1}\left\{\frac{\sin \nu_k}{\cos \nu_k}\right\} = \tan^{-1}\left\{\frac{\sqrt{1-e^2}\sin E_k/(1-e\cos E_k)}{(\cos E_k - e)/(1-e\cos E_k)}\right\}$	True anomaly υ_k as a function of the eccentric anomaly
$E_k = \cos^{-1}\left\{\frac{e + \cos \nu_k}{1 + e\cos \nu_k}\right\}$	Eccentric anomaly
$\Phi_k = \nu_k + \omega$	Argument of latitude
$\delta u_k = C_{us} \sin 2\Phi_k + C_{uc} \cos 2\Phi_k$	Argument of latitude correction } Second harmonic perturbations
$\delta r_k = C_{rs} \sin 2\Phi_k + C_{rc} \cos 2\Phi_k$	Radius correction
$\delta i_k = C_{is} \sin 2\Phi_k + C_{ic} \cos 2\Phi_k$	Inclination correction
$u_k = \Phi_k + \delta u_k$	Corrected argument of latitude
$r_k = A(1 - e\cos E_k) + \delta r_k$	Corrected radius
$i_k = i_0 + \delta i_k + (\text{IDOT})\, t_k$	Corrected inclination
$x_k' = r_k \cos u_k$ $y_k' = r_k \sin u_k$	Satellite position in orbital plane
$\Omega_k = \Omega_0 + (\dot{\Omega} - \dot{\Omega}_e)\, t_k - \dot{\Omega}_e\, t_{oe}$	Corrected longitude of ascending node
$x_k = x_k' \cos \Omega_k - y_k' \cos i_k \sin \Omega_k$ $y_k = x_k' \sin \Omega_k + y_k' \cos i_k \cos \Omega_k$ $z_k = y_k' \sin i_k$	Satellite position in Earth-centered, Earth-fixed coordinates

[a] t is GPS system time at time of transmission; i.e., GPS time corrected for transit time (range/speed of light). Furthermore, t_k shall be the actual total time difference between the time t and the epoch time t_{oe} and must account for beginning or end of week crossovers. That is, if t_k is greater than 302,400 s, subtract 604,800 s from t_k. If t_k is less than 302,400 s, add 604,800 s to t_k.

Appendix B

Quaternion algebra

The classical analysis of the rotation problem shows that transformations between three-dimensional vectors are accomplished by a tensor, known as the *rotation tensor*, which is usually expressed as a function of its associated vector quantity, the *rotation vector* (Fig. B.1).

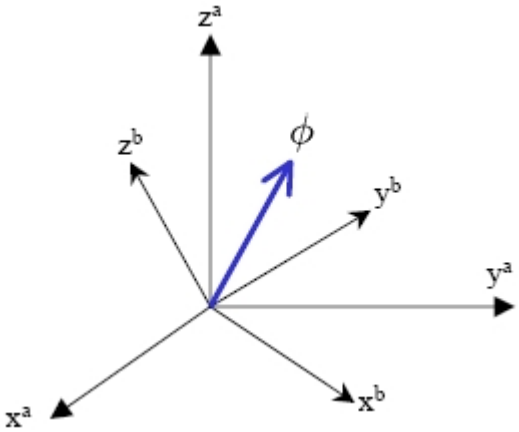

Fig. B.1 The rotation vector $\underline{\phi}$

However, rotations can be expressed in terms of parameters other than the rotation vector. The choice of a parameterization is usually made by considering the characteristics of a specific application, for example for avoiding singularities or for reducing the computational cost of certain operations [5].
Among the numerous techniques used for representing three-dimensional rotations, the quaternion algebra is frequently adopted. A quaternion is a four-dimensional vector defined as [32]

$$\underline{q} = \begin{bmatrix} q_1 \\ q_2 \\ q_3 \\ q_4 \end{bmatrix}^T = \begin{bmatrix} (\phi_x/\phi)\sin(\phi/2) \\ (\phi_y/\phi)\sin(\phi/2) \\ (\phi_z/\phi)\sin(\phi/2) \\ \cos(\phi/2) \end{bmatrix} \tag{B-1}$$

where ϕ_x, ϕ_y, and ϕ_z are the components of the rotation vector $\underline{\phi}$, and

$$\phi = \sqrt{\phi_x^2 + \phi_y^2 + \phi_z^2} \tag{B-2}$$

The four components of the quaternion vector are related by a constraint (normality condition):

$$q_1^2 + q_2^2 + q_3^2 + q_4^2 = 1 \tag{B-3}$$

A quaternion that satisfies this constraint is called a *unit quaternion* and can be used for the parameterization of rotations. Note that the application of this normalization condition does not correct for errors that occur during a computational cycle for the attitude update. In fact, an error arising in a single element of the quaternion can be spread amongst all of the other elements [32].
The complication of working with four parameters and a constraint equation, instead of three parameters only as for the case of the Euler angles, can be compensated in certain applications by the fact that this parameterization is singularity free, in the sense that is well defined for $-\infty < \phi < \infty$ [5]. Besides, quaternion algebra is preferred in updating the attitude information since the linearity of the quaternion differential equations and the lack of trigonometric functions allow an efficient implementation [11].
The differential equation for the quaternion parameters is given by [32]

$$\dot{\underline{q}} = \frac{1}{2}\begin{bmatrix} 0 & \omega_z & -\omega_y & \omega_x \\ -\omega_z & 0 & \omega_x & \omega_y \\ \omega_y & -\omega_x & 0 & \omega_z \\ -\omega_x & -\omega_y & -\omega_z & 0 \end{bmatrix} \underline{q} \tag{B-4}$$

where $\underline{\omega} = \begin{bmatrix} \omega_x & \omega_y & \omega_z \end{bmatrix}^T$ is the angular velocity of the rotation. Eq. (B-4) has to be transformed in a corresponding discrete form in order to be used in a computational algorithm. A possible expression is the following [14]:

$$\underline{q}_{k+1} = \underline{q}_k + \frac{1}{2}\begin{bmatrix} c & s\Delta\phi_z & -s\Delta\phi_y & s\Delta\phi_x \\ -s\Delta\phi_z & c & s\Delta\phi_x & s\Delta\phi_y \\ s\Delta\phi_y & -s\Delta\phi_x & c & s\Delta\phi_z \\ -s\Delta\phi_x & -s\Delta\phi_y & -s\Delta\phi_z & c \end{bmatrix}\underline{q}_k \tag{B-5}$$

where

$$s = \frac{2}{\Delta\phi}\sin\frac{\Delta\phi}{2} = 1 - \frac{\Delta\phi^2}{24} + \frac{\Delta\phi^4}{1920} + \cdots \tag{B-6}$$

$$c = 2\left(\cos\frac{\Delta\phi}{2} - 1\right) = -\frac{\Delta\phi^2}{4} + \frac{\Delta\phi^4}{192} + \cdots \tag{B-7}$$

and

$$\Delta\phi = \sqrt{\Delta\phi_x^2 + \Delta\phi_y^2 + \Delta\phi_z^2} \tag{B-8}$$

In the previous formulas, the operator Δ denotes an increment of a certain quantity during the time interval $t_{k+1} - t_k$.

The DCM R_a^b, which can be used for transforming a vector from the *a*-frame to the *b*-frame (Fig. B.1), can be obtained from the corresponding quaternion vector [14]:

$$R_a^b = \begin{bmatrix} \left(q_1^2 - q_2^2 - q_3^2 + q_4^2\right) & 2\left(q_1q_2 - q_3q_4\right) & 2\left(q_1q_3 + q_2q_4\right) \\ 2\left(q_1q_2 + q_3q_4\right) & \left(q_2^2 - q_1^2 - q_3^2 + q_4^2\right) & 2\left(q_2q_3 - q_1q_4\right) \\ 2\left(q_1q_3 - q_2q_4\right) & 2\left(q_2q_3 + q_1q_4\right) & \left(q_3^2 - q_1^2 - q_2^2 + q_4^2\right) \end{bmatrix} \tag{B-9}$$

In order to start an algorithm involving quaternion algebra, it is necessary to initialize the quaternion vector. If the initial Euler angles ϕ_0, θ_0, and ψ_0 are known (or at least their corresponding estimates with sufficiently good accuracy), the following expression can be used [33]:

$$\underline{q}_0 = \begin{bmatrix} \cos\frac{\phi_0}{2}\cos\frac{\theta_0}{2}\cos\frac{\psi_0}{2} + \sin\frac{\phi_0}{2}\sin\frac{\theta_0}{2}\cos\frac{\psi_0}{2} \\ \sin\frac{\phi_0}{2}\cos\frac{\theta_0}{2}\cos\frac{\psi_0}{2} - \cos\frac{\phi_0}{2}\sin\frac{\theta_0}{2}\sin\frac{\psi_0}{2} \\ \cos\frac{\phi_0}{2}\sin\frac{\theta_0}{2}\cos\frac{\psi_0}{2} + \sin\frac{\phi_0}{2}\cos\frac{\theta_0}{2}\sin\frac{\psi_0}{2} \\ \cos\frac{\phi_0}{2}\cos\frac{\theta_0}{2}\sin\frac{\psi_0}{2} - \sin\frac{\phi_0}{2}\sin\frac{\theta_0}{2}\cos\frac{\psi_0}{2} \end{bmatrix} \quad \text{(B-10)}$$

Alternatively, if the initial DCM is known, this other expression can be applied [32]:

$$\underline{q}_0 = \begin{bmatrix} 0.25\left(c_{32} - c_{23}\right) \Big/ \left(0.5\sqrt{1 + c_{11} + c_{22} + c_{33}}\right) \\ 0.25\left(c_{13} - c_{31}\right) \Big/ \left(0.5\sqrt{1 + c_{11} + c_{22} + c_{33}}\right) \\ 0.25\left(c_{21} - c_{12}\right) \Big/ \left(0.5\sqrt{1 + c_{11} + c_{22} + c_{33}}\right) \\ 0.5\sqrt{1 + c_{11} + c_{22} + c_{33}} \end{bmatrix} \quad \text{(B-11)}$$

where c_{ij}, $1 \le i, j \le 3$ is the (i, j) element of the DCM.

Appendix C

Specifications of the Crista IMU from Cloud Cap Technology

Gyros

- Range: ±300 ° /sec (Note 1)
- Scale Factor Error: < 1 %
- In-Run Bias Error:
  - Fixed temperature < 0.05 % FS
  - Over temperature < 0.2 % FS
- Turn-on to Turn-on Bias < 0.25 % FS
- Linear Acceleration Effects 0.2 ° /sec / g typical.
- Resolution: 0.009 ° /sec
- Bandwidth 2nd order filter. Fc=100 Hz.

Accelerometers

- Range: ±10g (Note 2)
- Scale Factor Error: < 1 %
- In-Run Bias Error:
  - Fixed temperature < 0.025 % FS
  - Over temperature < 0.2 % FS
- Turn-on to Turn-on Bias < 0.3 % FS
- Alignment Error < 0.025g
- Resolution: 0.3mg
- Bandwidth Simple RC LPF. Fc=100 Hz.

Interface

- Serial Interface Options RS232 and/or CAN.
- Data Output Rate > 200 Hz User settable.
- Internal A/D Sample Rate > 1 KHz. **Important**: Output Rate x Over-samples must be > 200.

Power

- Vin 4.4 – 8 Volts
- Iin (max) 143ma @ 5 Volts
  (typ) 110ma @ 5 Volts

Physical

- Size: 2.05" x 1.55" x 1.00" (1.35" x 1.50" x 0.80" without enclosure)
- Weight: 36.8. grams (1.3 oz) (18.8 grams (0.7 oz) without enclosure)

Environment

- Operating Temperature: -40C to +80C Calibrated Temperature Range
- Storage Temperature -60C to +100C
- Max Acceleration 500g

---

[1] ±150 ° /sec option available.
[2] ± 2g option available.

Appendix D

The Galileo System

Galileo is a proposed global navigation positioning system of the European Union and European Space Agency. Galileo is tasked with multiple objectives, including the following [10]:

- to provide a higher precision to all users than is currently available through GPS;
- to improve availability of positioning services at higher latitudes;
- to provide an independent positioning system upon which European nations can always rely.

The initial project plan has the system as operational by 2011; however, some delay is currently expected. The European Union and the United States have signed an agreement (June 2004) to ensure compatibility between their two satellite positioning systems [10], [19]. The deal means that the two sides will agree common operating standards for the American GPS and the European Galileo project currently under development. The agreement will create a world standard for signals, which means that users will be able to obtain similar signals from both systems. Dual GPS-Galileo receivers will provide additional availability, precision, and robustness.

The Galileo constellation will consist of 27 operational satellites equally distributed over 3 orbit planes, in a 27/3/1 Walker constellation. This means that the right ascension of ascending nodes of the three planes are separated by 40º in-plane. Each plane will include an additional (inactive) spare satellite [37]. The main orbit parameters will be:

- semi-major axis: 29601 *km*;
- eccentricity: 0.002;
- inclination: 56º;

- argument of perigee: 0º (TBC);
- right ascension of ascending node: 0º, 120º, 240º (TBC).

Four services will be available: open service (OS), safety of life (SOL), commercial service (CS), and public regulated service (PRS).

Galileo will provide six navigation signals in the frequency ranges 1164-1215 *MHz* (E5 band), 1260-1300 *MHz* (E6 band), and 1559-1592 *MHz* (E2-L1-E1 band). All satellites will make use of the same carrier frequency with different ranging (spreading) codes through CDMA transmission. Tab. D.1 displays the performance for the Galileo services [19].

Tab. D.1 Performance for the Galileo services

Service	OS	CS	SOL	PRS
Positioning accuracy (Horizontal, 2 dRMS, 95%) (Vertical, 95%)	*15m or 24 m H - 35m V (single frequency) 4m H - 8m V (dual frequency)*		*4m H - 8m V (dual frequency)*	*15m or 24m H - 35m V (single frequency) 6.5m H - 12m V (dual frequency)*
Timing accuracy (95%)	*30 ns*	*30 ns*	*30 ns*	*30 ns*
Integrity:	*None*	*None*		
Alert limit			*12m H - 20m V*	*20m H - 35m V*
Time to alert			*6 sec*	*10 sec*
Integrity risk			*3.5 x 10^{-7}/150 sec*	*3.5 x 10^{-7}/150 sec*
Continuity risk	-	-	*1 x 10^{-5}/15 sec*	*1 x 10^{-5}/15 sec*
Service availability	99.5%	99.5%	99.5%	99.5%

Notes:

- Single frequency accuracy depends on the frequency used: 15m horizontal accuracy when using the L1 signal or 24m when using the other frequencies (E5, E6).
- Integrity is defined by the following parameters:
  - alert limit: the maximum allowable error in the user position solution before an alarm is to be raised within the specific time to alert;
  - time to alert: the time from which an alarm condition occurs until when the alarm is received at he user level (including the time to detect the alarm condition);
  - Integrity risk: the probability, during any continuous period of peration, tht the computed vertical or horizontal positioning error exceeds the corresponding alert limit and the user is not informed within the specified time to alert (note that the value reported in the table includes the user contribution of 1.5 x 10^{-7}/150 seconds).